

**Physical processes behind the periodic
radio and gamma-ray emission from the
X-ray binary LS I +61°303**

Dissertation
zur
Erlangung des Doktorgrades (Dr. rer. nat.)
der
Mathematisch-Naturwissenschaftlichen Fakultät
der
Rheinischen Friedrich-Wilhelms-Universität Bonn

vorgelegt von

Frédéric Felix Daniel Jaron

aus
Siegburg

Bonn 2016

Angefertigt mit Genehmigung der Mathematisch-Naturwissenschaftlichen Fakultät der Rheinischen Friedrich-Wilhelms-Universität Bonn

1. Gutachterin: Priv.-Doz. Dr. Maria Massi
2. Gutachter: Prof. Dr. Norbert Langer

Tag der Promotion: 9. Juni 2016
Erscheinungsjahr: 2016

Summary

X-ray binaries are binary stars composed of a normal star and a compact object which, via Roche-lobe overflow or wind accretion, accretes matter from the companion. X-ray emission from these objects can be either thermal emission from an accretion disk formed around the compact object, or the result of inverse Compton scattering. Emission in the radio regime is synchrotron emission from relativistic electrons gyrating in the magnetic fields of a jet. Some X-ray binaries are also emitters of γ -ray emission, the physical processes behind the non-thermal emission of these objects are still poorly understood. Subject of this thesis is the investigation on physical processes behind the emission from one particular γ -ray-loud X-ray binary, LS I +61°303. This source is composed of a Be type star and a compact object of still unknown nature, i.e., either a neutron star or a black hole. Accretion onto the compact object along the eccentric orbit of this source is predicted to peak twice per orbit, giving rise to emission all over the electromagnetic spectrum modulated by the orbital period $P_1 \approx 26.5$ days. Analysis of the astrometry of VLBI images of the source resulted in a precession period of a jet of 27–28 days, expected to give rise to periodic variable Doppler boosting. Timing analysis of archived radio data revealed that a compatible period of $P_2 \approx 26.9$ days modulates the radio lightcurve in addition to P_1 , giving rise to a beating with a long-term period of ~ 4.5 years, in agreement with previous findings. The methods employed for this thesis are timing analysis of radio and GeV lightcurves, and the modelling of physical processes which can lead to radio and GeV emission from LS I +61°303. The first result

of this thesis is how the knowledge about the beating between the periodic ejection of particles and the jet precession can be used for a straightforward prediction of the radio outbursts observable by radio telescopes. The GeV light curve has previously been reported to peak around periastron only. The second result presented here is the discovery of a periodic apastron GeV peak, also explaining a previously reported disappearance of the orbital period from the power spectrum of the GeV light curve during some epochs. We further find that, while the apastron GeV peak is modulated by P_1 and P_2 , the periastron GeV peak is only modulated by P_1 . This timing characteristic is explained by a physical model of a self-absorbed, adiabatically expanding jet, re-filled with a population of relativistic electrons twice along the orbit, the bulk velocity of the jet being slower at periastron than at apastron, giving rise to smaller variable Doppler boosting at periastron, and consequently, P_2 is not present in the power spectrum during these orbital phases. In addition, the absence of a periastron radio peak is explained by catastrophic inverse Compton losses of the electrons at periastron, leading to a jet too short for radio emission. We further report on the detection of radio emission of the first proven case of a binary star composed of a Be type star and a black hole, MWC 656, a source which has also been detected in the GeV regime and therefore bears resemblance to LS I +61°303. The source LS I +61°303 does not only feature variability in the order of months to years, but there is also evidence for short-term variability over time scales of days and shorter. We observed LS I +61°303 with the 100-m telescope in Effelsberg, quasi-simultaneously at three radio frequencies with unprecedented sampling rate for a multiwavelength observation of this source. We present our results on possible periodic behavior on time-scales of hours, which can possibly contribute to future investigations on transient phenomena related to the jet. In conclusion, we show that an accretion scenario for LS I +61°303, including a precessing relativistic jet, can explain the periodic emission from this X-ray binary and may help to understand the physical processes in related sources.

Zusammenfassung

Röntgendoppelsterne bestehen aus einem normalen Stern und einem kompakten Objekt, das, durch Überschreitung der Roche-Grenzen oder durch Akkretion des Sternenwindes, Masse vom Begleitstern akkretiert. Röntgenstrahlung entsteht in diesen Objekten entweder als thermische Strahlung von der Akkretionsscheibe oder als Folge des inversen Compton-Effekts. Strahlung im Radiobereich ist Synchrotronstrahlung, emittiert von relativistischen Elektronen, die in den Magnetfeldern des Jets auf Kreisbahnen gelenkt werden. Einige Röntgendoppelsterne sind darüber hinaus Quellen von Gammastrahlung, wobei die physikalischen Prozesse, die für die Strahlung von diesen Objekten verantwortlich sind, noch immer nicht gut verstanden sind. Gegenstand dieser Doktorarbeit ist die Erforschung der physikalischen Prozessen, die die elektromagnetischen Emission eines bestimmten gamma-emittierenden Röntgendoppelsterns, LS I +61°303, erklären können. Diese Quelle besteht aus einem Be-Stern und einem kompakten Objekt, von dem noch unbekannt ist, ob es sich um einen Neutronenstern oder ein schwarzes Loch handelt. Aufgrund der hohen Exzentrizität des Orbits wird vorhergesagt, dass Akkretion von Materie auf das kompakte Objekt zwei Maxima per Orbit ausbildet, und es, als Konsequenz davon, zu einer Modulation mit der orbitalen Periode $P_1 \approx 26.5$ Tage der resultierenden Strahlung über den gesamten Bereich des elektromagnetischen Spektrums kommt. Eine Analyse der Astrometrie von VLBI-Bildern der Quelle hatte eine Präzessionsperiode des Jets von 27–28 Tagen zum Ergebnis, was erwartungsgemäß zu variablem Doppler-Boosting führen sollte. Durch Zeitreihenanalyse

von archivierten Radiodaten stellte sich heraus, dass eine mit diesem Ergebnis zu vereinbarende Periode von $P_2 \approx 26.9$ Tagen die Radiolichtkurze zusätzlich zu P_1 moduliert, was eine Schwebung mit einer Periode von ca. 4.5 Jahren zur Folge hat, und was in Übereinstimmung mit vorhergehenden Beobachtungen ist. Die in dieser Arbeit zum Einsatz kommenden Methoden beinhalten Zeitreihenanalyse von Radio- und GeV-Lichtkurven sowie die Modellierung von physikalischen Prozessen, die zur Emission im Radio- und GeV-Bereich im Doppelsternsystem LS I +61°303 führen können. Als erstes Ergebnis dieser Arbeit wird gezeigt, wie das Wissen über die Schwebung zwischen der periodischen Beschleunigung von Teilchen und der Präzession des Jets für eine unkomplizierte Vorhersage der Radiostrahlungsmaxima für die Beobachtung mit Radioteleskopen genutzt werden kann. Bisher wurde berichtet, dass die GeV-Lichtkurve Strahlungsmaxima ausschließlich bei Periastron aufweist. Das zweite hier vorgestellte Ergebnis ist die Entdeckung eines periodischen GeV-Strahlungsmaximum während des Apastron, ein Ergebnis, das auch ein zeitweises Verschwinden der orbitalen Periode aus dem Periodenspektrum der GeV-Lichtkurve erklärt. Gleichzeitig finden wir heraus, dass, während das Apastron-GeV-Maximum von P_1 und P_2 moduliert wird, das Periastron-Maximum nur einer Modulation mit P_1 unterliegt. Dieses Verhalten wird, als ein weiteres Ergebnis dieser Arbeit, erklärt durch ein physikalisches Modell eines selbstabsorbierenden, adiabatisch expandierenden Jet, der periodisch, zweimal pro Orbit mit einer Population von relativistischen Elektronen befüllt wird, wobei die Geschwindigkeit entlang des Jets bei Periastron langsamer ist als bei Apastron, was bei Periastron geringeres Doppler-Boosting als bei Apastron zur Folge hat, und infolgedessen P_2 im Periodenspektrum bei Periastron nicht auftaucht. Darüber hinaus wird die Abwesenheit eines Periastron-Radiomaximums erklärt durch katastrophale Energieverluste der Elektronen durch den inversen Compton-Effekt beim Periastron, was in einem Jet, der zu kurz für Radioemission ist, resultiert. Ein weiteres Ergebnis dieser Arbeit ist die Detektion von Radiostrahlung vom ersten nachgewiesenen Fall eines Doppelsterns bestehend aus einem Be-Stern und einem schwarzen Loch, MWC 656, eine Quelle, die auch im GeV-Bereich detektiert

wurde und daher starke Ähnlichkeit mit LS I +61°303 aufweist. LS I +61°303 ist nicht nur variabel auf Zeitskalen von Monaten oder Jahren, sondern es gibt auch Hinweise auf Kurzzeitvariabilität auf Zeitskalen von Tagen oder kürzer. Wir haben LS I +61°303 mit dem 100-m-Teleskop in Effelsberg beobachtet, quasisimultan auf drei Frequenzen mit der bisher höchsten Abtastrate, die bei einer gleichzeitigen Beobachtung dieser Quelle mit mehreren Wellenlängen erreicht wurde. Hier werden Ergebnisse bezüglich möglichen Periodizitäten auf Zeitskalen von Stunden vorgestellt, was möglicherweise als Grundlage für die Erforschung von kurzzeitigen Phänomenen im Jet dienen kann. Zusammenfassend wird gezeigt, dass ein Akkretionsszenario für LS I +61°303 in Zusammenhang mit einem präzedierenden Jet die periodische Emission dieses Röntgendoppelsterns erklären kann und zum Verständnis der physikalischen Prozesse in verwandten Objekten beitragen kann.

Contents

List of Figures	xv
List of Tables	xvii
1 Introduction	1
2 X-ray binaries	9
2.1 Mass transfer in X-ray binaries	9
2.2 Microquasars	11
2.3 X-ray binaries with γ -ray emission	14
3 GeV emission from relativistic jets	17
3.1 Inverse Compton	18
3.2 Particle reactions	18
4 The binary system LS I +61°303	21
4.0.1 The stellar binary system	21
4.1 Pulsar vs. microquasar model	24
4.2 Two-peak accretion model for LS I +61°303	27
4.3 Flattening of the radio spectrum of LS I +61°303	29
4.4 The fast precessing jet of LS I +61°303	31
4.5 The periodic emission from LS I +61°303	31
4.6 The SED of LS I +61°303	35
4.7 Updated SED of LS I +61°303	37
4.8 The GeV emission from LS I +61°303 observed by <i>Fermi</i> -LAT	38

4.9	Related objects	38
4.9.1	The Be-BH binary MWC 656	40
4.9.2	The fast precessing jet of GRO J1655-40	40
5	Prediction of the radio outbursts of LS I +61°303	41
5.1	Introduction	42
5.2	Timing residuals	43
5.2.1	Prediction using the orbital period P_1	44
5.2.2	Predictions with P_{average}	45
5.2.3	Determination of the periodical reset	47
5.3	Conclusions	50
6	Discovery of a periodic apastron GeV peak in LS I +61°303	53
6.1	Introduction	54
6.2	Data analysis	55
6.3	Results	59
6.3.1	Wavelet and Lomb-Scargle analysis	59
6.3.2	Orbital shift	62
6.4	Discussion and conclusion	63
7	Understanding the periodicities in the radio and GeV emission from LS I +61°303	69
7.1	Introduction	70
7.2	Methods	73
7.2.1	Relativistic electron distribution	73
7.2.2	Stellar seed photons	76
7.2.3	Jet seed photons	77
7.2.4	IC emission	77
7.2.5	Accelerated electron survival	79
7.3	Observations and data reduction	80
7.3.1	Consistency with previous results	81
7.3.2	Influence of the Θ interval on P_2	83
7.4	Results	86
7.5	Conclusions	89

8	Observation of QPO from LS I +61°303 at radio wave-lengths	91
8.1	Introduction	91
8.2	Observation	93
	8.2.1 Schedule	93
	8.2.2 Calibration	93
8.3	Results	95
	8.3.1 Light curves	95
	8.3.2 Evolution of the spectral index	95
	8.3.3 Flattening of the radio spectrum	96
	8.3.4 Timing analysis	96
	8.3.5 Polarization	100
	8.3.6 Comparison to <i>Fermi</i> -LAT data	100
8.4	Conclusion	102
9	Radio emission from the Be/black hole binary MWC 656	105
9.1	Introduction	106
9.2	Observations	109
9.3	Results	111
9.4	MWC 656 in the context of the L_X, L_R relationship . .	114
9.5	Updated SED	114
9.6	Conclusions	114
10	Conclusion and outlook	119
10.1	Conclusions	119
10.2	Outlook	121
A	Methods	123
A.1	Programs and scripts	123
	A.1.1 Starlink	123
A.2	Binfold	124
	A.2.1 Introduction	124
	A.2.2 Simple Folding	124
	A.2.3 Binned Folding	124
	A.2.4 Bifold	127
A.3	Analysis of <i>Fermi</i> -LAT data	128

A.3.1	Generating <i>Fermi</i> -LAT light curves	128
	Acknowledgements	137
	Bibliography	139

List of Figures

1.1	Atmospheric window	2
1.2	Effelsberg and OVRO radio telescopes	3
1.3	Schematic sketch of the <i>Fermi</i> -LAT	4
1.4	The <i>Fermi</i> -LAT sky	5
2.1	Artist's impression of an X-ray binary	10
2.2	VLBI images of GRS 1915+105	12
2.3	Flat radio spectrum	13
3.1	Compton scattering	17
4.1	Sketch of LS I +61°303	22
4.2	Radio emission from LS I +61°303	23
4.3	Microquasar vs. pulsar model	25
4.4	Accretion along eccentric orbit	27
4.5	Accretion and emission for LS I +61°303	28
4.6	Radio spectral index of LS I +61°303	30
4.7	VLBA images of LS I +61°303	32
4.8	40 years of radio data from LS I +61°303	34
4.9	Broad band spectrum of LS I +61°303	36
4.10	SED for LS I +61°303	37
4.11	Counts map of LS I +61°303	39
5.1	Timing residuals for the radio outbursts of LS I +61°303	46
5.2	Optimizing P_{average}	48
5.3	Folded GBI radio data from LS I +61°303	49

5.4	Illustration of the predicted outbursts	51
6.1	First 8 months <i>Fermi</i> -LAT observations of LS I +61°303	56
6.2	Wavelet analysis of <i>Fermi</i> -LAT data	57
6.3	Lomb-Scargle periodogram of the <i>Fermi</i> -LAT data . .	61
6.4	Apastron GeV peak of LS I +61°303	64
7.1	Timing analysis of <i>Fermi</i> -LAT and model data	71
7.2	Electron density and Lorentz factor	75
7.3	Timing analysis of Pass 8 <i>Fermi</i> -LAT data	82
7.4	Test on the Θ -interval which corrupts the timing analysis	84
7.5	<i>Fermi</i> -LAT apastron data	85
7.6	Results of the model in comparison with the observations	88
8.1	Radio light curves and spectral index of LS I +61°303 .	92
8.2	Archived GBI data vs. newly observed radio data . . .	94
8.3	<i>Fermi</i> -LAT and Effelsberg light curves	97
8.4	Flux density vs. frequency	98
8.5	Timing analysis of Effelsberg data	99
8.6	QPO in 5 and 10 GHz Effelsberg radio data	101
9.1	Radio emission from MWC 656	112
9.2	VLA images of MWC 656 from epoch 2 to 7	113
9.3	MWC 656 in the fundamental plane	115
9.4	Updated SED for MWC 656	116

List of Tables

2.1	Gamma-ray emitting X-ray binaries	16
7.1	Model parameters	87
8.1	Best fit parameters	98
8.2	QPO Best fit parameters	100
9.1	MWC 656 observations	107
A.1	Keywords for binfold	127

Chapter 1

Introduction

Since the beginning of sky observations the only information of objects in the universe could be gathered through the optical regime of the electromagnetic spectrum. The radical change came in 1932, when Karl Jansky detected radio signals of extraterrestrial origin (Jansky 1933). In the course of the twentieth century many more new windows to the universe were opened. Nowadays we are observing the sky in the entire electromagnetic spectrum from low frequency radio waves (10–240 MHz, Heald et al. 2011) up to very high energy energy γ -rays in the TeV regime, observed by ground based Cherenkov telescopes. Windows beyond the electromagnetic interaction have been opened by neutrino observatories exploiting the weak interaction (IceCube, Kurauchi & for the IceCube Collaboration 2014), and very recently the first gravitational waves were detected, originating from the merger event of two black holes, marking the birth of gravitational astronomy (Abbott et al. 2016).

For this PhD thesis I used data from radio and GeV γ -ray observations. Figure 1.1 shows how the electromagnetic spectrum is absorbed or transmitted by the atmosphere of the Earth. In this plot, atmospheric opacity against wavelength, there is one region from ~ 5 cm to ~ 10 m in which the opacity drops to zero, this region is called the atmospheric window and is the reason why radio observations can be carried out by ground based observatories. Two examples of radio telescopes are pre-

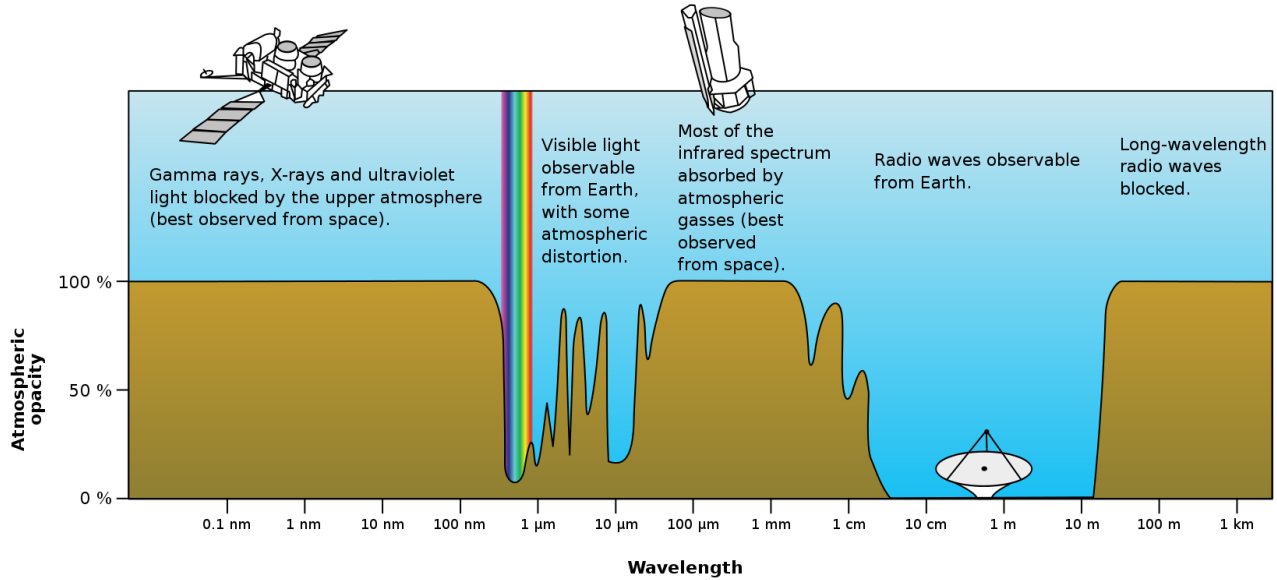


Figure 1.1: Absorption and transmission of electromagnetic waves by the atmosphere of the Earth. Optical and radio waves can reach the ground, hence the name atmospheric window. Source: https://upload.wikimedia.org/wikipedia/commons/3/34/Atmospheric_electromagnetic_opacity.svg



Figure 1.2: Top: The 100-m radio telescope in Effelsberg, Germany. Built in 1969, it is the second largest free steerable radio telescope in the world. Source: http://www.mpifr-bonn.mpg.de/337419/gallery_zoom.jpg **Bottom:** Owens Valley Radio Observatory (OVRO) 40-m dish. Source: https://www.ovro.caltech.edu/images/40m_small_4.jpg Data from both instruments, along with the Green Bank Interferometer (GBI), have been used for the thesis.

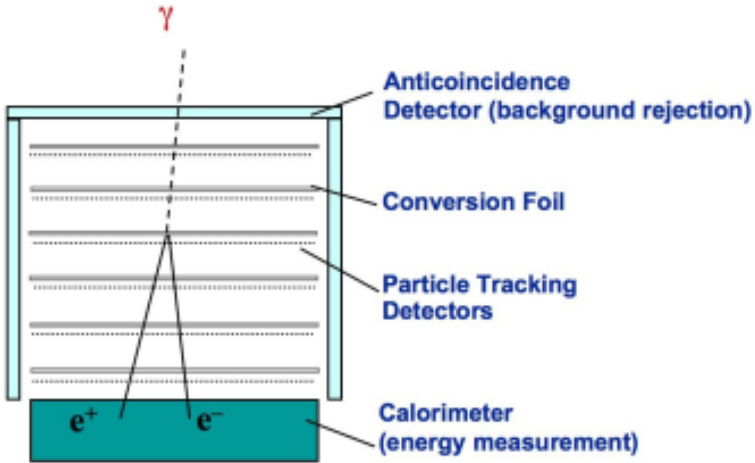


Figure 1.3: Principle of the *Fermi*-LAT. An incident γ -ray photon decays into an electron-positron pair, the energy and direction of which is detected. Source: https://www-glast.stanford.edu/images/Gamma_telescope_schematic.png

sented in Fig. 1.2, showing the Effelsberg 100-m telescope in the top panel and the 40-m telescope of the Owens Valley Radio Observatory (OVRO) in the bottom panel.

From the plot in Fig. 1.1 it is evident that the GeV γ -ray regime (i.e., wavelengths in the order of femtometer) has to be observed by satellites orbiting the Earth, because photons at these energies are totally absorbed by the atmosphere. The *Fermi* satellite carries an instrument for that purpose, the Large Area Telescope (LAT), monitoring the entire sky in the energy range 0.1 to over 300 GeV every three hours. The principle of the LAT is shown in Fig. 1.3. An incident γ -ray photons, in the presence of tungsten atoms, decays into an electron-positron pair. The tracks of these decay products are used to reconstruct the direction of the incident photon. The energy of the electron-positron pair is detected in the calorimeter. In this way, the *Fermi*-LAT counts single photons and stores the direction and energy of every one of these. Fig-

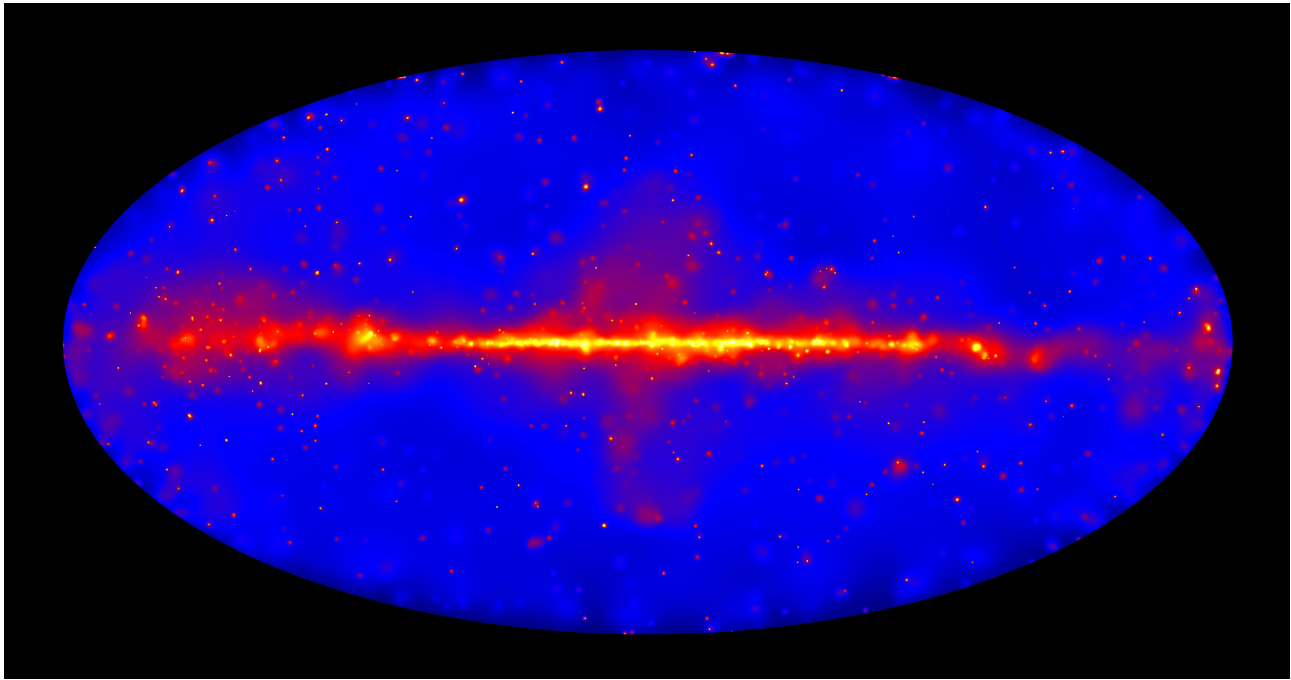


Figure 1.4: The sky as seen by the *Fermi*-LAT in the energy range 50 GeV–1 TeV. The horizontal feature is the emission from the Galactic plane. The Galactic center is in the middle of the map, the two diffuse features extending from the center to the north and south are the famous Fermi bubbles. Source: http://www.nasa.gov/sites/default/files/thumbnails/image/2fhl_all-sky_no_labels.jpg

ure 1.4 shows the sky as seen by the *Fermi*-LAT in the energy range 50 GeV to 1 TeV. The red band extending from East to West in the middle of the image is the Galactic plane. The Galactic center is in the middle of the image, and the two diffuse features extending from the center to the North and South direction are the famous *Fermi* bubble. Below and above the Galactic plane there are a lot of extragalactic point sources, most of which are blazars.

In many cases the physical processes behind the emission detected by the observatories is not known yet. Here are two examples: In the Galactic center one observes more GeV emission than expected. This GeV excess could be the result of dark matter annihilation, another model attributing the emission to a population of undetected pulsars. The other example are the *Fermi* bubbles, believed to be the remainder of past activity of the supermassive black hole located at the center of the Galaxy.

The physical processes behind the γ -ray emission from X-ray binaries is another unsolved problem of γ -ray astronomy. Subject of this thesis are physical processes which can lead to periodic emission in radio and GeV γ -rays from one particular X-ray binary, LS I +61°303. We apply timing analysis to observational radio and γ -ray data and investigate on correlations between the two energy bands. We put LS I +61°303 in context to other stellar binary systems of similar composition or behavior.

This PhD thesis is structured as follows. Chapter 2 introduces the class of X-ray binaries and puts LS I +61°303 in this context. Chapter 3 introduces physical processes which lead to γ -ray emission in relativistic jets. Chapter 4 gives a general introduction to the stellar binary system LS I +61°303. Chapter 5 shows how the findings of *Massi & Jaron (2013)* lead to a straightforward prediction of the radio outbursts from LS I +61°303 (this chapter was published as *Jaron & Massi 2013* in *A&A*). Chapter 6 reports on the discovery of a periodic apastron GeV peak in LS I +61°303 (this chapter was published as *Jaron & Massi 2014* in *A&A*). Chapter 7 presents a physical model for the periodic radio and GeV emission from LS I +61°303 (this chapter has been submitted to *A&A*). We have observed LS I +61°303 with the

100-m radio telescope in Effelsberg and report on these observations in Chapter 8 and present our results (this chapter will serve as basis for a manuscript to be submitted to A&A). Chapter 9 reports on the detection of radio emission from a related object, MWC 656 (parts of this chapter have been published as Dzib et al. 2015 in A&A). Chapter 10 contains the conclusion of this thesis and gives an outlook on future investigations.

Chapter 2

X-ray binaries

X-ray binaries are binary stars composed of a normal star and a neutron star or a stellar mass black hole (i.e., a compact object) accreting matter from the companion (i.e., the donor star). Depending on the mass of the donor star one distinguishes between two types of X-ray binaries. If the primary star has a mass of less than one solar mass the system is called *low mass X-ray binary* (LMXB). Systems with a primary star mass greater than five solar masses are called *high mass X-ray binaries* (HMXB). An artist's impression of an X-ray binary is shown in Fig. 2.1.

2.1 Mass transfer in X-ray binaries

Mass transfer from the donor star can occur in two ways. One possibility is that during the evolution of the lifetime of the donor, the star fills its Roche lobe and mass can travel through the Lagrangian point from the donor to the compact object. Roche lobe overflow is the only possibility for accretion in LMXB. On the other hand, high-mass stars have winds strong enough for accretion in HMXB, giving rise for this second possibility for accretion in these systems.

Because the matter from the star has a certain angular momentum, it does not fall directly onto the compact object. The matter forms an *accretion disk* around the compact object, which by the means of

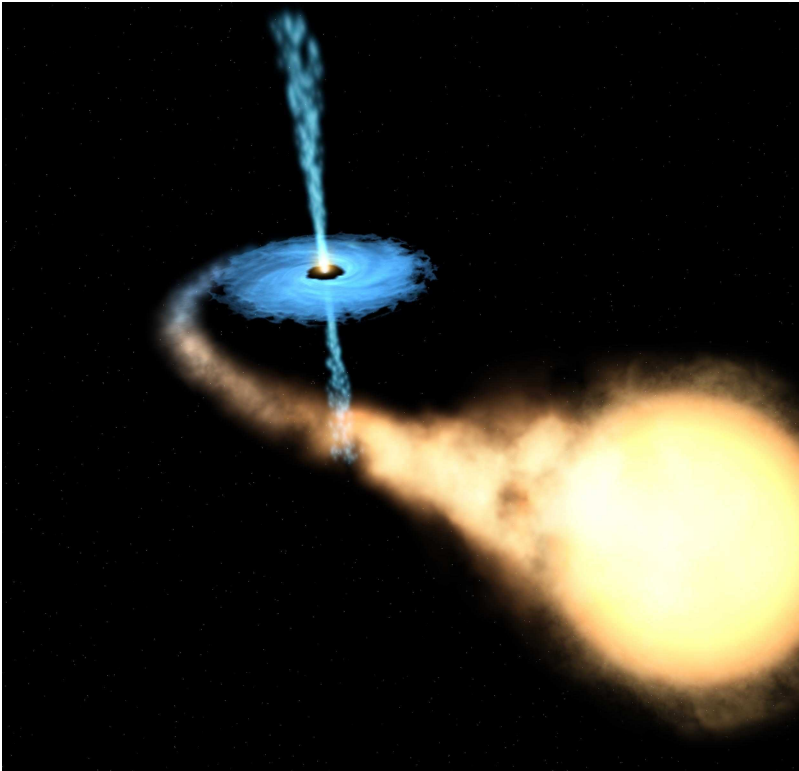


Figure 2.1: Artist's impression of an X-ray binary. The donor star loses mass which is transferred to the compact object where an accretion disk is formed and a jet is launched. ESA (2013) <http://hubblesite.org/newscenter/archive/releases/2002/30/image/a/>

viscous forces reaches temperatures in the order of 10^7 K, giving rise to a thermal black body component observed in the X-ray spectrum (not present in the low-hard X-ray state of X-ray binaries, see Sect. 2.2). Accretion is one of the most efficient ways of energy release in the universe, even when compared to nuclear reactions.

The majority of X-ray binaries harbors a neutron star with a strong magnetic field (i.e., $> 10^8$ Gauss). If the rotational velocity of the neutron star is not too high, the matter from the accretion disk falls further down but is forced to travel on the magnetic field lines of the neutron star and finally reaches the pole caps, where the energy is released in form of X-ray pulses. If the rotational velocity is sufficiently high, the matter cannot reach the poles and the system is in the so-called propeller regime (Illarionov & Sunyaev 1975). If the magnetic field $B < 10^8$ Gauss, or if the compact object is a black hole, then a jet can be formed. This case is treated in the next section.

2.2 Microquasars

A subset of X-ray binaries ($\sim 10\%$) are also sources of radio emission. One example is GRS 1915+105, and Fig. 2.2 shows a series of Very Large Baseline Interferometry (VLBI) images of this source, the position of the stationary core is marked by the small cross in each image (Fig. 2 in Rodríguez & Mirabel 1995). The elongated structure, well visible in these images, is two-sided and moves further outwards from the central engine, as time evolves. This collimated outflow is called a *jet* and is a ubiquitous phenomenon in accretion processes, from young stellar objects to the supermassive black holes of active galactic nuclei (AGN). This is why the term *microquasar* was coined by Mirabel et al. (1992) in analogy to quasars, a subclass of AGN (see Mirabel & Rodríguez 1999 for a review).

The origin of the radio emission in jets is synchrotron radiation emitted by relativistic charged particles gyrating in magnetic fields.

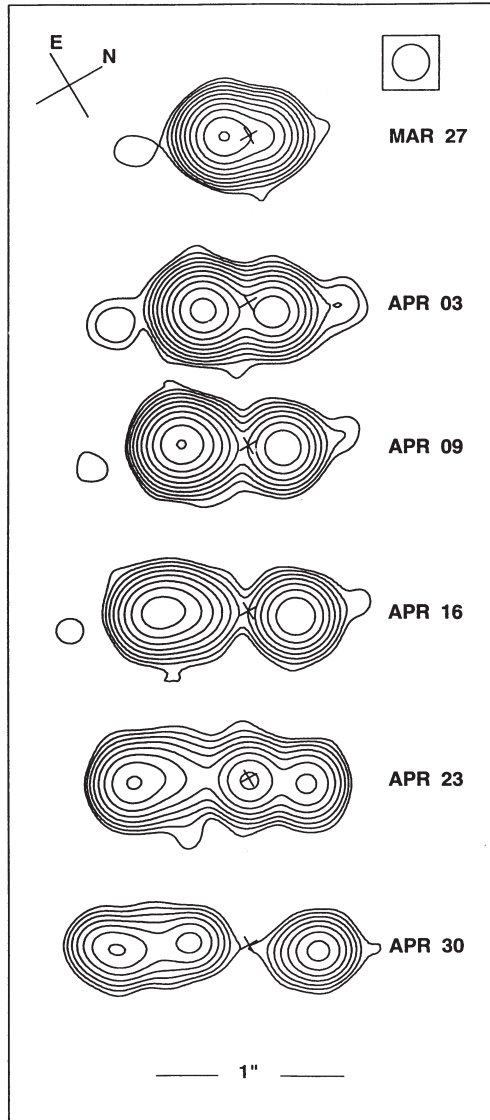


Figure 2.2: VLBI images of the X-ray binary GRS 1915+105, a microquasar. The elongated structure and the movement of features outwards from the central engine justify the interpretation as a relativistic jet. Figure 2 in Rodriguez & Mirabel (1995).

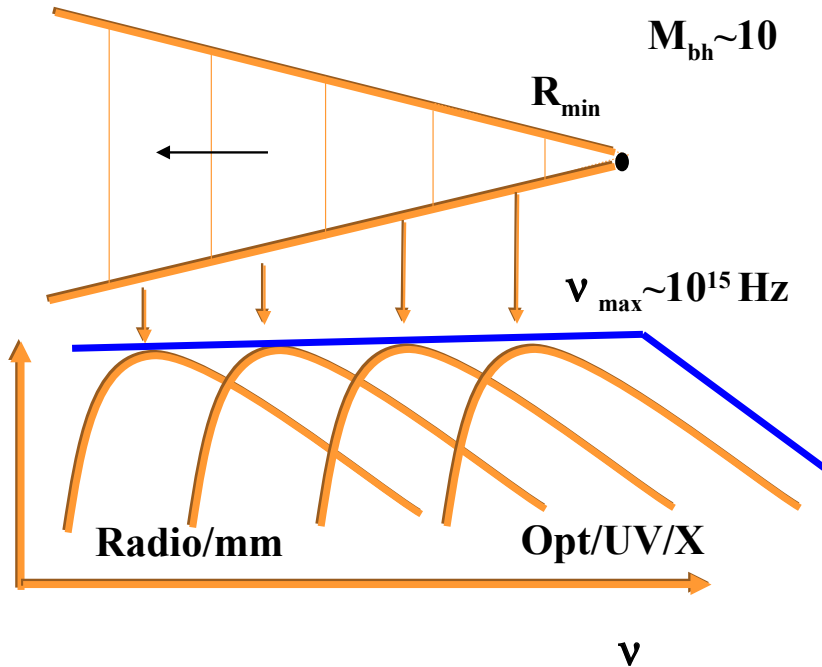


Figure 2.3: Composite spectrum of a jet from a stellar mass accreting black hole. Source: http://www.astro.isas.ac.jp/conference/bh2003/program/ppt/20031029am/KyotoBH2003_Falcke.ppt

The peak frequency

$$\nu_{\text{peak}} \approx 3.2 \cdot 10^7 \sin \theta \left(\frac{E_0}{1 \text{ MeV}} \right)^{(2\delta-2)/(\delta+4)} \times \left[8.7 \cdot 10^{-12} \frac{\delta-1}{\sin \theta} NL \right]^{2/(\delta+4)} B^{(\delta+2)/(\delta+4)} \quad (2.1)$$

depends on the electron density N and the magnetic field strength B (Eq. 43 from Dulk 1985). Since both N and B change along the jet, the resulting radio spectrum, when observed with a resolution which does not resolve the jet, appears flat (Blandford & Königl 1979; Hjellming & Johnston 1988; Falcke et al. 1996; Kaiser 2006; Pe'er & Casella 2009), where flat means that the radio spectral index

$$\alpha = \frac{\log(S_1/S_2)}{\log(\nu_1/\nu_2)} \quad (2.2)$$

is approximately zero, assuming a power law radio flux,

$$S \propto \nu^\alpha. \quad (2.3)$$

Figure 2.3 shows an illustration of the observed flat radio spectrum being the sum of individual spectra emitted in different regions along the unresolved jet.

2.3 X-ray binaries with γ -ray emission

A subset of X-ray binaries, all of which are HMXB, are also emitters of γ -rays. A full list is presented in Table 2.1. In the table caption, one (example) reference is given for each detection in the GeV and/or TeV regime. For about half of the γ -ray-loud X-ray binaries the compact object is of unknown nature, indicated by a question mark in the table. Only one object, PSR B1259-63, contains a proven pulsar, while three of the others contain a proven black hole. The only known binary system composed of a Be star and a black hole, MWC 656, appears in this list, because a detection in the GeV regime by the AGILE satellite (Lucarelli et al. 2010) has by now been confirmed (Alexander & McSwain

2015, who also give a possible explanation for the non-detection by the *Fermi*-LAT).

Name	Primary	Compact object	GeV	TeV	Comment
1FGL J1018.6-5856	O	?	yes ¹	yes ²	
Cyg X-1	O	black hole	yes ³	yes ⁴	
Cyg X-3	Wolf-Rayet	black hole ?	yes ⁵	no	
HESS J0632+057	Be	?	no	yes ⁶	
LS 5039	O	?	yes ⁷	yes ⁸	
LS I +61°303	Be	?	yes ⁹	yes ¹⁰	
MWC 656	Be	black hole	yes ¹¹	no	See Chapter 9 for radio detection.
PSR B1259-63	Be	pulsar	yes ¹²	yes ¹³	
SS 433	A	black hole	yes ¹⁴	no	Detected up to 800 MeV.

Table 2.1: Gamma-ray emitting X-ray binaries. The references are: ¹The Fermi LAT Collaboration et al. (2012), ²H. E. S. S. Collaboration et al. (2015), ³Bodaghee et al. (2013), ⁴Albert et al. (2007), ⁵Bodaghee et al. (2013), ⁶Aharonian et al. (2007), ⁷Abdo et al. (2009c), ⁸Mariaud et al. (2015), ⁹Abdo et al. (2009b), ¹⁰Albert et al. (2009), ¹¹Alexander & McSwain (2015), ¹²Abdo et al. (2011), ¹³Aharonian et al. (2005), ¹⁴Bordas et al. (2015).

Chapter 3

GeV emission from relativistic jets

Relativistic jets are not only sources of radio emission. Because of the relativistic velocities of the plasma traveling in the jet there are also other physical processes which lead to emission at other wavelengths. In this section two processes, which can lead to emission in the GeV regime, are presented.

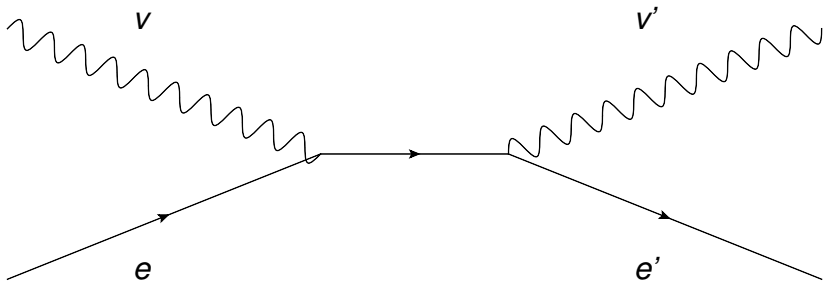


Figure 3.1: Feynman graph for Compton scattering. The time direction is from left to right.

3.1 Inverse Compton

Scattering of particles, electrons in particular, with photons is known as *Compton scattering*. In this process energy is transferred between the participants. In the non-relativistic case, i.e., the electron travels at velocities which are small compared to the speed of light, the photon loses energy and the electron gains energy. At relativistic speeds, however, energy is transferred from the electron to the photon (called *seed photon* in this context), which results in a photon with a shorter wavelength than before the encounter. This process is known as *inverse Compton* (IC) scattering and is one of the most important physical processes leading to high energy radiation from astrophysical sources.

The relativistic speeds of particles accelerated in a jet and the presence of seed photons from a number of sources make IC an important process in jet sources. In the context of a jet the source of seed photons allows for a further classification. The process is called *external inverse Compton* (EIC) if the seed photons come from outside of the jet, e.g., from the companion star or the accretion disk in case of a microquasar. The other possibility is that the seed photons are synchrotron photons emitted by the jet itself, which is why the process is called *synchrotron self-Compton* (SSC).

There is still the possibility that an IC reprocessed photon serves as a seed photon and is again upscattered to a higher energy. This process is referred to as *cascading*.

3.2 Particle reactions

The physical make-up of jets is still a matter of debate. The presence of a leptonic component has recently been confirmed by the observation of the characteristic line at 511 keV in the microquasar V404 Cygni (Siegert et al. 2016), resulting from the annihilation of electron-positron pairs,

$$e^+e^- \rightarrow \gamma\gamma. \quad (3.1)$$

Another possibility for the production of high energy emission is a hadronic component of the jet, i.e., not only electrons and positrons

(leptons) are accelerated in the jet, but also protons (hadrons). Gamma-ray emission can be the result of the decay of neutral pions, formed by either the collision of high-energy protons with coller material in the jet or by pion photoproduction, into two photons

$$\pi^0 \rightarrow \gamma\gamma, \quad (3.2)$$

in which case the two photons would have the characteristic energy of 135 MeV. The decay of charged pions (e.g., π^+)

$$\pi^+ \rightarrow \mu^+ + \nu_\mu \rightarrow e^+ + \nu_\mu + \nu_e \quad (3.3)$$

would lead to a neutrino flux, possibly detectable by the IceCube experiment.

Chapter 4

The binary system LS I +61°303

This chapter provides a general introduction to the binary star LS I +61°303, which is the most important object of this thesis. Observational results are presented and physical scenarios are discussed.

4.0.1 The stellar binary system

The stellar binary system LS I +61°303 consists of a Be type star and a compact object and is located at a distance of about 2 kpc (Hutchings & Crampton 1981). Figure 4.1 shows a sketch of the system.

The orbital period is $P_1 = 26.4960 \pm 0.0028$ days (Gregory 2002), and the orbital phase is defined as

$$\Phi = \frac{t - t_0}{P_1} - \text{int} \left(\frac{t - t_0}{P_1} \right), \quad (4.1)$$

where $t_0 = \text{MJD } 43366.275$ is the time of the first radio detection of the source (Gregory & Taylor 1978), and $\text{int}(x)$ takes the integer part of x . Periastron passage occurs at $\Phi = 0.23 \pm 0.02$ (Casares et al. 2005).

The source is observable and highly variable all over the electromagnetic spectrum, but in this thesis we focus on the radio and GeV

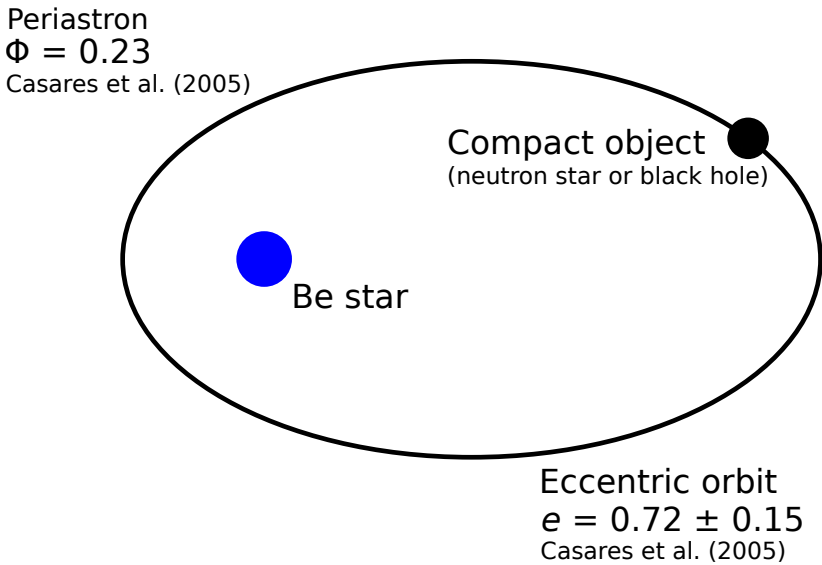


Figure 4.1: Sketch of the stellar binary system LS I +61°303. The compact object (neutron star or black hole) orbits the Be star in a very eccentric orbit. Periastron passage occurs at orbital phase $\Phi = 0.23$.

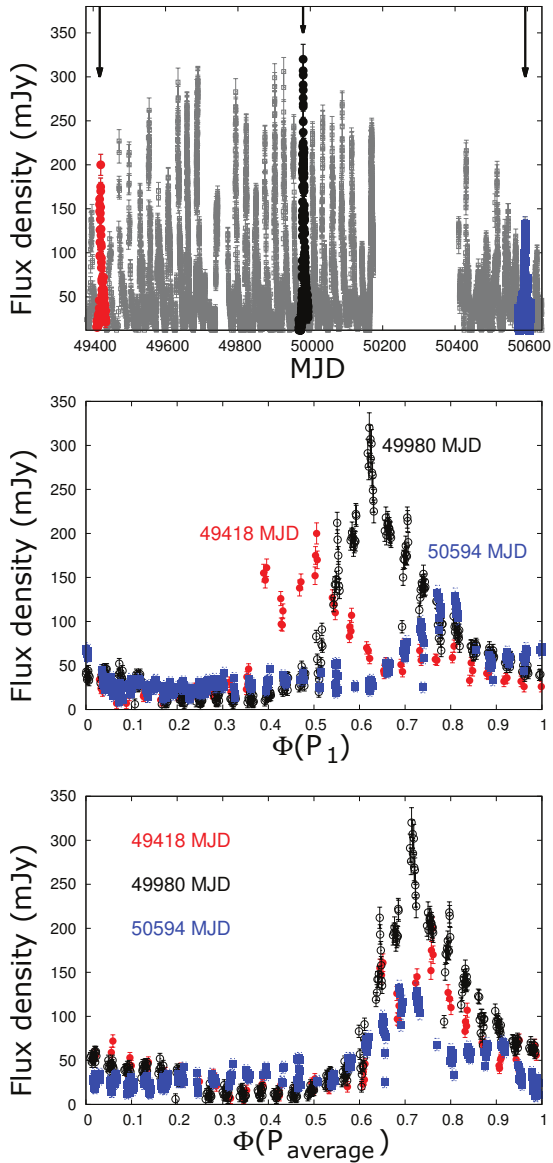


Figure 4.2: Phase of radio outbursts of LS I +61°303 with respect to P_1 (top panel) and P_{average} (bottom panel). Figure 1 in Massi & Torricelli-Ciamponi (2016).

γ -ray emission, which features periodic behavior. Radio outbursts occur once per orbit and at orbital phases $\Phi = 0.4 - 0.9$, i.e., around apastron (see Fig. 4.2, which is a reproduction of Fig. 1 in Massi & Torricelli-Ciamponi 2016). The GeV γ -ray emission peaks twice per orbit, once at periastron and fixed in orbital phase, and once around apastron, with hints for a correlation to the radio peaks in orbital phase occurrence (Jaron & Massi 2014).

The emission from LS I +61°303 is subject to a long-term modulation, which has first been detected in the radio light curves (Gregory 2002), but which has also been associated to other wavelengths, in particular to the apastron (defined as $\Phi = 0.5 - 1.0$) GeV emission (Ackermann et al. 2013). The long-term phase Θ is defined analogously to the orbital phase Φ ,

$$\Theta = \frac{t - t_0}{P_{\text{long}}} - \text{int} \left(\frac{t - t_0}{P_{\text{long}}} \right), \quad (4.2)$$

where $t_0 = \text{MJD } 43366.275$ is the same as for Φ , and $P_{\text{long}} = 1628 \pm 49$ days (Massi & Torricelli-Ciamponi 2016). The characteristics of this long-term modulation and the possible reasons for it are explained further down.

4.1 Pulsar vs. microquasar model

The physical processes behind the radio and GeV emission, which are both non-thermal, is still a matter of debate. In the literature two competing models are discussed, the one being the pulsar model and the other the microquasar model. The following paragraphs will introduce the basic ideas behind the two models.

If the compact object is a black hole or a neutron star with a low magnetic field ($\leq 10^8$ Gauss, Psaltis 2004) it can accrete matter from the companion star to become a *microquasar*. (Fig. 4.3 left panel). The matter forms an accretion disk and a jet is launched, in which charged particles, accelerated to relativistic speeds, gyrate in the magnetic fields and emit synchrotron radiation in the radio regime. Optical

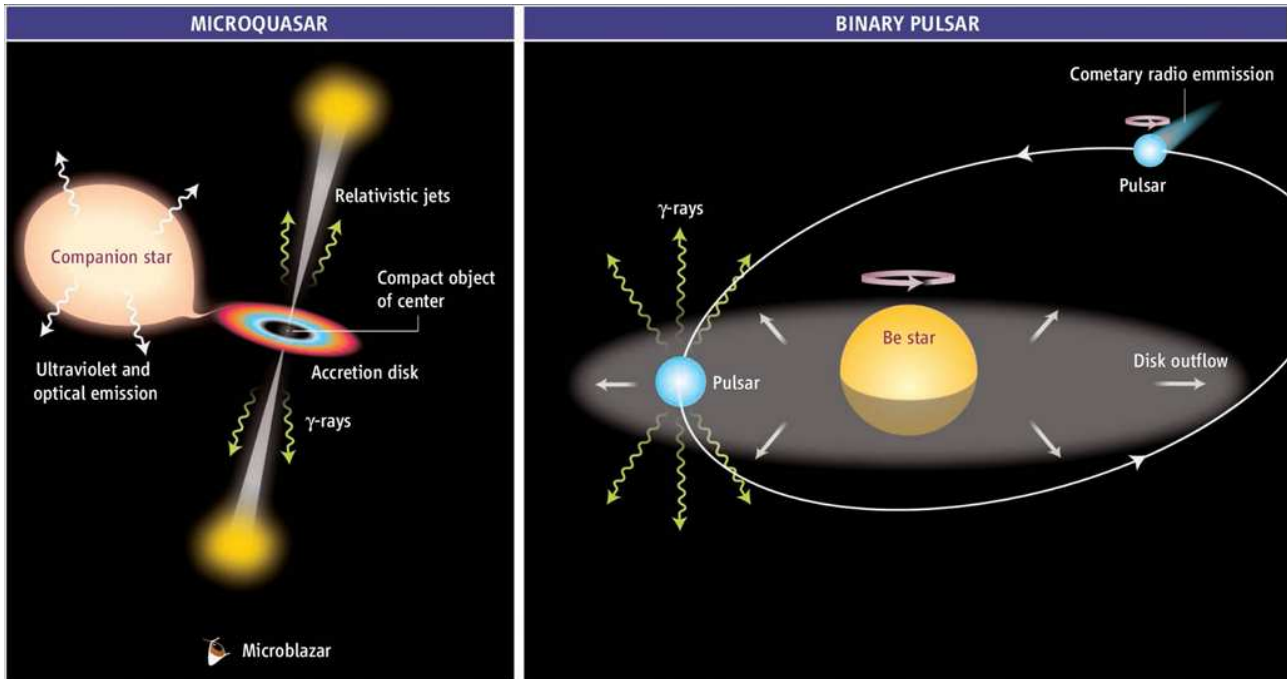


Figure 4.3: Sketches of the two models discussed for the origin of the non-thermal emission from LS I +61°303. **Left:** Microquasar model. The compact object accretes matter from the companion star. The relativistic charged particles accelerated in a jet emit synchrotron emission in the radio regime and upscatter seed photon to the GeV regime. **Right:** Pulsar model. The compact object is a pulsar, the wind of which collides with the Be star wind, resulting in radio to γ -ray emission. (Figure from Mirabel 2006.)

photons from the companion star can be upscattered to higher energies by EIC, synchrotron photons from the jet can by SSC. Both EIC and SSC can produce emission in the GeV regime (see Chapter 7 for a physical model for GeV emission from LS I +61°303).

In the *pulsar model* the compact object is assumed to be a rapidly rotating neutron star with a high magnetic field ($> 10^{12}$ Gauss), i.e., a pulsar¹, in which the matter is either forced on the magnetic field lines to the pole caps (X-ray pulsar), or, if the rotation is strong enough, the pulsar can be in the propeller regime. In the right panel of Fig. 4.3 (Figure from Mirabel 2006) this model is depicted in a schematic way. In this model the non-thermal emission from radio to γ -rays is produced in the collision between the Be star wind and the pulsar wind (Maraschi & Treves 1981; Dubus 2006; Moldón et al. 2012). There is indeed one binary star which consists of a Be star and a pulsar, which is PSR B1259-63 (Johnston et al. 1992). The orbit of this system is highly eccentric and for most of the time 47.7 ms radio pulsations can be detected from the source. Periastron passage occurs every 1237 days, the pulsar passes through the dense Be star wind and the pulses disappear. Instead of radio pulsations, continuous emission is observed from radio to TeV wavelengths (see, e.g., Chernyakova et al. 2015 for the 2014 periastron passage).

In summary, observations show that all of the emission from this source, PSR B1259-63, peaks around periastron passage, occurring every ~ 3.4 years (Connors et al. 2002; Abdo et al. 2011; Chernyakova et al. 2014). The modulation of the fluxes from LS I +61°303, for which a search for pulses remains elusive (McSwain et al. 2011), shows a pattern which is better explained by an accretion scenario, as explained in the next subsection.

¹See, i.e., Harding (2013) for a recent review on neutron stars and pulsars.

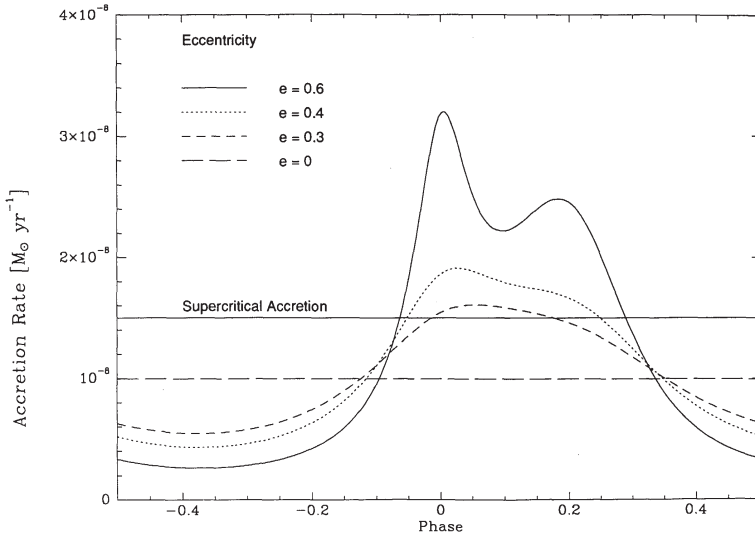


Figure 4.4: Bondi & Hoyle (1944) accretion along an eccentric orbit for different values of the eccentricity e . Please note that in this figure periastron is defined at $\Phi = 0$. Figure 7 from Taylor et al. (1992).

4.2 Two-peak accretion model for LS I +61°303

Bondi & Hoyle (1944) accretion,

$$\dot{M} \propto \frac{\rho}{v^3}, \quad (4.3)$$

is proportional to the density ρ and inversely proportional to the third power of the relative velocity v between the accretor and the matter to be accreted. In a binary system where the compact object accretes matter from the companion star along an eccentric orbit ($e > 0$), the accretion rate \dot{M} will be a function of the orbital phase. In Fig. 4.4 (Fig. 7 in Taylor et al. 1992, where periastron is defined at $\Phi = 0$, different from the remainder of this thesis) the accretion rate, as a function of orbital phase, is plotted for different values of the eccentricity e , and it is shown that for $e > 0.4$ the accretion rate has two peaks along the or-

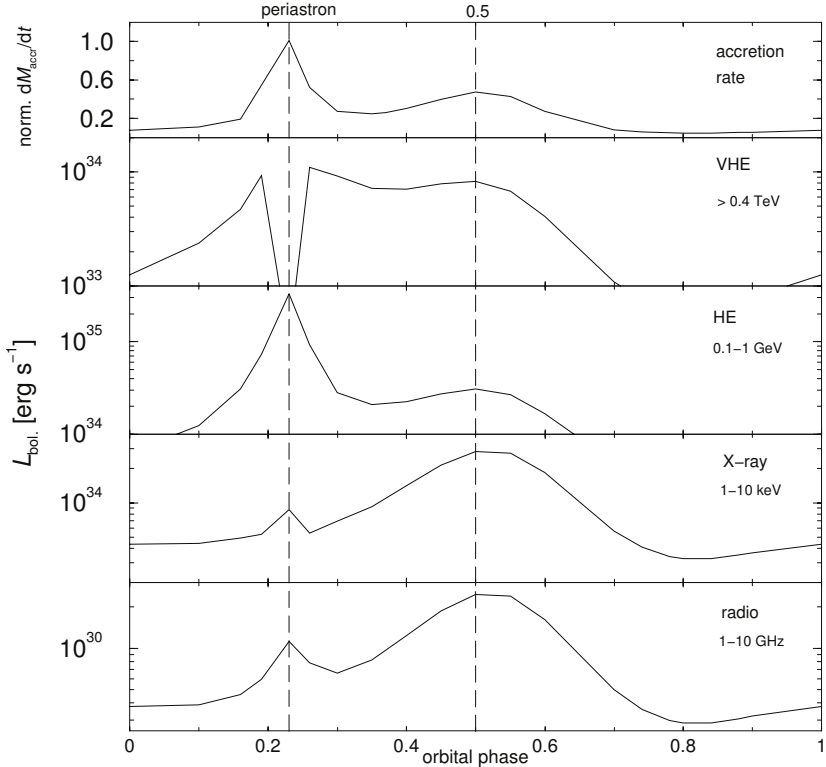


Figure 4.5: Predicted accretion rate (top panel) and emission at different wavelengths as a function of orbital phase for the eccentric orbit of LS I +61°303. Figure 1 from Bosch-Ramon et al. (2006).

bit, one peak at periastron where the density ρ is greatest, and a second peak towards apastron where the lower velocity v between the compact object and the Be star wind compensates for the lower density during these orbital phases. Several authors have shown that this *two peak accretion model* applies for LS I +61°303 (Taylor et al. 1992; Marti & Paredes 1995; Bosch-Ramon et al. 2006; Romero et al. 2007).

In addition to the accretion rate along the eccentric orbit of LS I +61°303, Bosch-Ramon et al. (2006) computed the emission at different wavelengths, their Fig. 1 is reproduced as Fig. 4.5 here. In the top panel of Fig. 4.5 one sees that the major accretion peak is predicted at periastron and a second, minor peak towards apastron. The predicted radio emission (bottom panel of Fig. 4.5) has a major peak at apastron, and only a minor peak is predicted to occur at periastron. The fact that we do not observe a periastron radio peak can be explained by catastrophic inverse Compton losses of the relativistic particles in the strong ultra violet photon field in the proximity to the Be star, which will be treated in detail in Chapter 7 of this thesis (submitted to A&A as Jaron, Torricelli-Ciamponi, & Massi). In the GeV regime the situation looks almost opposite to what is predicted for radio, here we have a major outburst at periastron and a minor one towards apastron. Indeed, two GeV peaks along the orbit are observed (Chapter 6 of this thesis, which has been published as Jaron & Massi 2014), however, the observed apastron GeV peak is much more pronounced than the one predicted by Bosch-Ramon et al. (2006), which could be due to the neglect of Doppler boosting in their model.

4.3 Flattening of the radio spectrum of LS I +61°303

The two peak accretion model (Taylor et al. 1992; Marti & Paredes 1995; Bosch-Ramon et al. 2006; Romero et al. 2007) not only corroborated by the observation of a periodic apastron radio peak (Gregory 2002) and the two GeV peaks along the orbit (Jaron & Massi 2014), but also by the evolution of the radio spectral index (Massi & Kaufman Bernadó 2009). In Fig. 4.6 top the radio spectral index α (as defined by Eq. 2.2), resulting from observations by the GBI simultaneously at the two frequencies 2.2 and 8.3 GHz, is folded on the orbital period $P_1 = 26.4960$ days, showing the orbital evolution of α . It is evident that the spectral index undergoes a transition from optically thin ($\alpha < 0$) to flat ($\alpha = 0$) and inverted ($\alpha > 0$) twice along the orbit, once at periastron and once towards apastron, i.e., during these parts

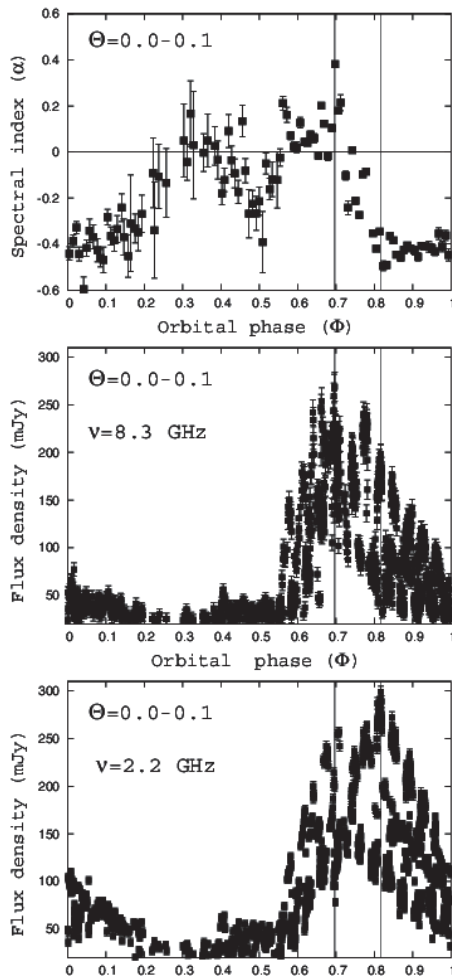


Figure 4.6: Top: Radio spectral index, resulting from the observations by the GBI at 2.2 and 8.3 GHz, folded on the orbital period P_1 , showing its orbital evolution. During the presented long-term phase interval ($\Theta_{1667\text{d}} = 0.0-0.1$) the flattening and even inversion twice along the orbit is particularly well visible. Figure 3 in Massi & Kaufman Bernadó (2009). **Middle:** 8.3 GHz GBI data folded on P_1 . **Bottom:** 2.2 GHz GBI data folded on P_1 .

of the orbit where enhanced accretion is expected following the two peak accretion model and where consequently a jet is launched, which is expected to result in a flat or inverted spectrum, in agreement with the observations.

4.4 The fast precessing jet of LS I +61°303

Figure 4.7 (Fig. 1 in Massi et al. 2012) shows consecutive Very Large Baseline Interferometry (VLBI) images of LS I +61°303 covering one orbit. The elongated structure of the self-calibrated images (middle panel of Fig. 4.7) continuously changes position angle and performs a transition from one-sided to two-sided. By analyzing the astrometry Massi et al. (2012) estimated a precession period in the range of 27–28 days.

While tidal forces in binary systems typically lead to precession periods ten times larger than the orbital one, Lense-Thirring precession (i.e., frame dragging) of a slow compact rotator can be the reason for a precession period so short (Massi & Zimmermann 2010).

4.5 The periodic emission from LS I +61°303

As mentioned in Section 4.2, the high eccentricity of the orbit of LS I +61°303 is expected to give rise to the emission being modulated by the orbital period $P_1 = 26.4960 \pm 0.0028$ days (Gregory 2002), in agreement with the observations at multiple wavelengths. But P_1 is not the only periodicity affecting the emission from the source. In Section 4.4 we saw VLBI images of a fast precessing jet, which will give rise to variable Doppler boosting of the emission for relativistic bulk velocities (a physical model for the radio emission has been developed in Massi & Torricelli-Ciamponi 2014). Indeed, a period compatible with the precession period estimated by Massi et al. (2012) has been found by timing analysis of radio (Massi & Jaron 2013; Massi et al. 2015; Massi & Torricelli-Ciamponi 2016), *Fermi*-LAT γ -ray data (Jaron & Massi 2014), and recently also in X-rays (D’Aì et al. 2016),

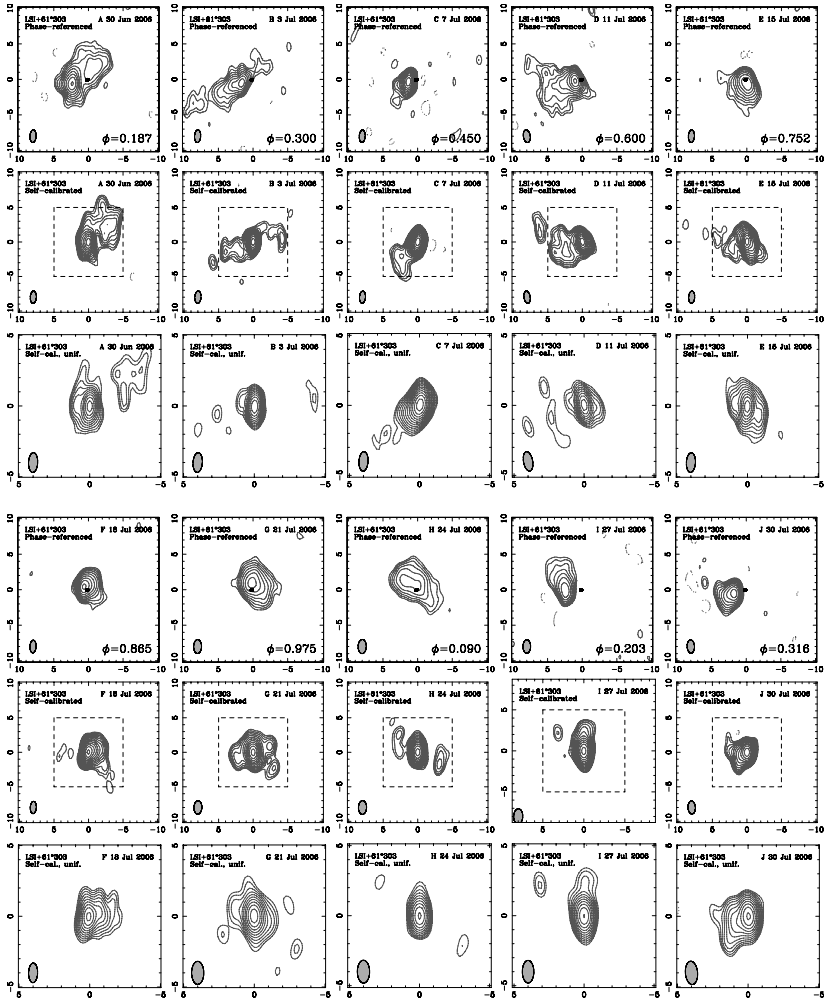


Figure 4.7: Consecutive VLBI images of LS I +61°303 covering one orbit showing an elongated structure, sometimes one-sided, sometimes two-sided, continuously changing position angle along the orbit. Figure 1 in Massi et al. (2012).

the values being in the range $P_2 = 26.92 - 26.935$ days, slightly larger than the orbital period P_1 .

Since the orbital period P_1 and the precession period P_2 are close to each other, the interference between the two modulations has the shape of a beating. The sum of two sine waves

$$\sin(\omega_1 t) + \sin(\omega_2 t) = 2 \sin\left(\frac{\omega_1 + \omega_2}{2} t\right) \cos\left(\frac{\omega_1 - \omega_2}{2} t\right) \quad (4.4)$$

at similar frequencies $\omega_1 \approx \omega_2$ results in a sine wave oscillating at the average frequency, slowly modulated by a cosine term depending on the difference between ω_1 and ω_2 . Coming back to the observed radio emission from LS I +61°303, Ray et al. (1997) found that the radio outbursts, observed by the Green Bank Interferometer (GBI) at 2 and 8 GHz, occur with a period of 26.69 ± 0.02 days, which they interpreted as an “apparent lengthening of the period between outbursts”, but which finds a natural explanation in the beating model, since this value is in agreement with the average between P_1 and P_2 , which is $P_{\text{average}} = 26.704 \pm 0.004$ days (Massi & Torricelli-Ciamponi 2016).

The other period resulting from the beating, $P_{\text{beat}} = (\nu_1 - \nu_2)^{-1} = 1628 \pm 49$ days (Massi & Torricelli-Ciamponi 2016), has also been found before, Gregory (2002) give $P_{\text{long}} = 1667 \pm 8$ days for the long-term radio monitoring by the GBI. Ackermann et al. (2013) confirm the Gregory (2002) value for the 0.1–300 GeV emission observed by the *Fermi*-LAT, a database completely different from the GBI monitoring regarding observation time and energy range.

Massi & Torricelli-Ciamponi (2016) concatenate all of the available radio data from 1977 until 2014 (see Fig. 4.8) and reveal that the long-term modulation has remained stable over this time range, which corresponds to eight long-term cycles. This stability is another observational fact which speaks in favor of the beating model. The alternative explanation of the long-term modulation attributes the variability to the Be star wind, which usually comes from one-armed density waves in the equatorial disk causing variation in the V/R ratio of the $H\alpha$ line (Okazaki 1997), but this is at odds with the stability, because all of the known variations in Be star winds are only quasi-periodic

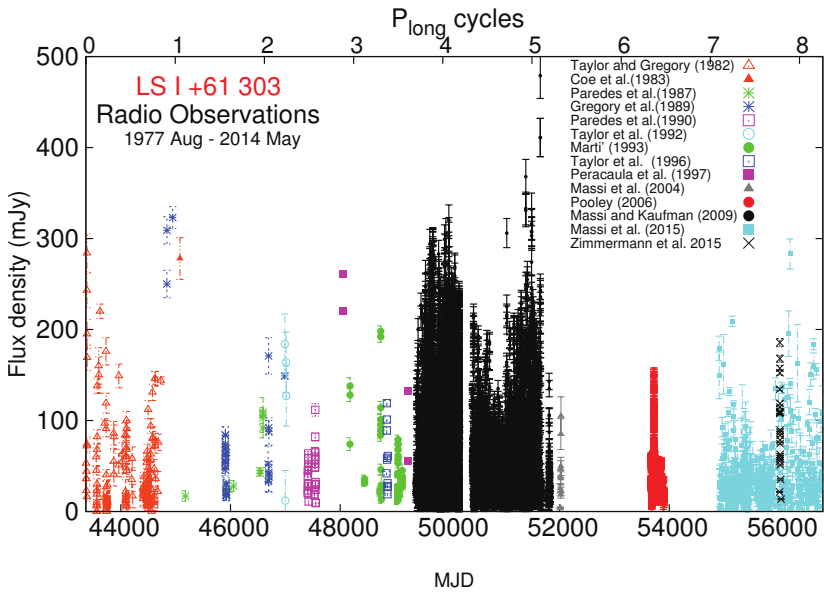


Figure 4.8: All available radio data from LS I +61°303. Figure 2 in Massi & Torricelli-Ciamponi (2016).

and even disappear sometimes (Rivinius et al. 2013, and references therein), even in the most stable variation of a Be star disk observed so far (ζ Tau, Štefl et al. 2009). Searches for a periodicity in the V/R ratio of the $H\alpha$ emission from LS I +61°303 compatible with P_{long} have returned negative results (Zamanov et al. 1999, 2013).

However, Zamanov et al. (2013) reported the presence of the long-term period in the equivalent width (EW) of the $H\alpha$ emission line from LS I +61°303. Moreover, the $\text{EW}(H\alpha)$ is affected by the orbital shift in a similar way as the radio outbursts (Paredes-Fortuny et al. 2015), suggesting that P_{average} is the true period of $\text{EW}(H\alpha)$, as pointed out by Massi & Torricelli-Ciamponi (2016), who further state that the presence of both long-term period and P_{average} indicates that the precessing jet also induces variations in $\text{EW}(H\alpha)$.

4.6 The SED of LS I +61°303

In Figure 4.9 the SED of LS I +61°303 is shown, which appears as Fig. 7 in Sidoli et al. 2006. A composition of data from different observations (Strickman et al. 1998; van Dijk et al. 1996; Kniffen et al. 1997; Albert et al. 2006), it covers a frequency range from radio to very high energy γ -rays. The absolute peak is in the infrared regime, shown in the shape of stars in the figure. If one assumes this emission to be thermal, then the peak of the non-thermal emission is in the MeV regime, making it a member of the γ -ray binaries as defined by Dubus (2013).

The similarity between the SED of LS I +61°303 (Fig. 4.9) of the blazar 3C 279 (Fig. ??) is evident when comparing the two figures. Both show the characteristic camel back shape, the higher energy hump peaking at 10^{22} Hz for both sources. The SED for LS I +61°303 has a strong peak in the infrared, however, a large fraction of this IR emission may be thermal emission from the Be star.

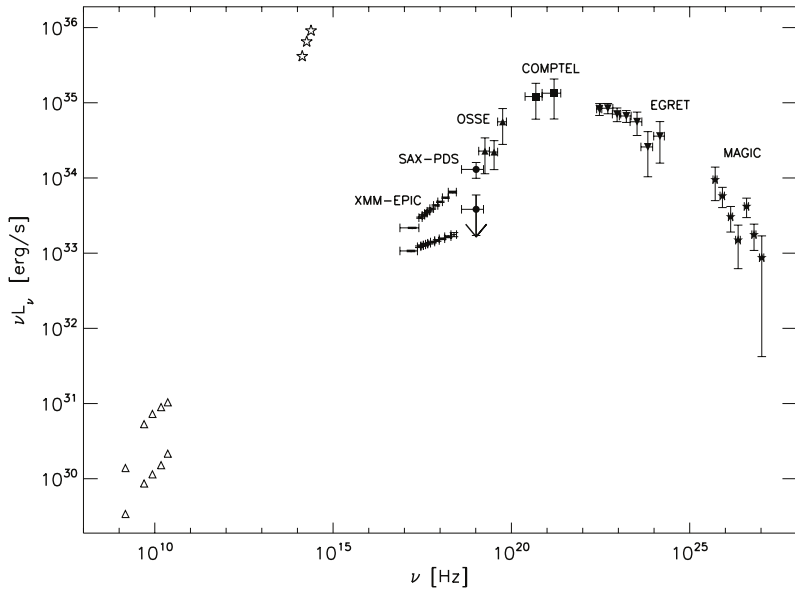


Figure 4.9: The broad band spectrum of LS I +61°303 (Sidoli et al. 2006), resulting from observations with different instruments at different wavelengths.

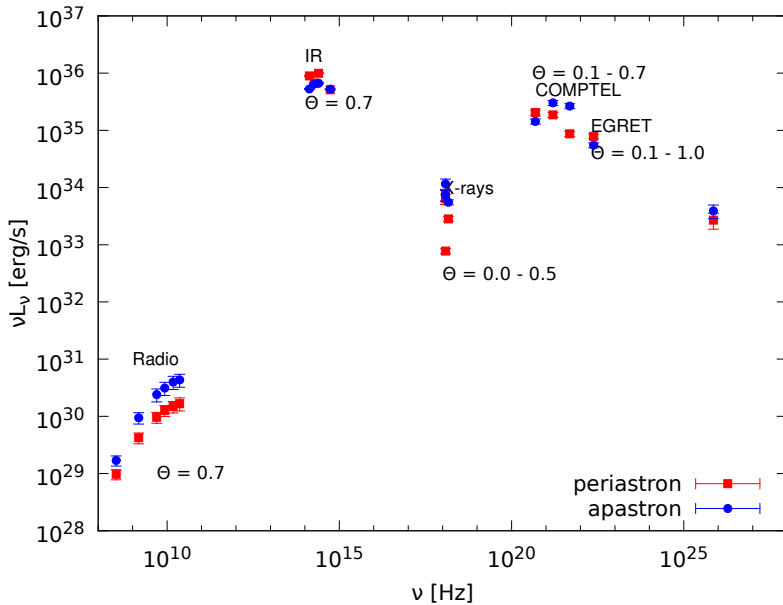


Figure 4.10: SED for LS I +61°303 based on the data of Fig. 7 in Sidoli et al. (2006) (Fig. 4.9 here), divided into periastron ($\Phi = 0.0 - 0.5$, red squares) and apastron ($\Phi = 0.5 - 1.0$, blue circles).

4.7 Updated SED of LS I +61°303

The emission from the binary system LS I +61°303 strongly depends on the orbital phase. The SED shown in Fig. 4.9 does not take orbital phase into account. Only in the cases of radio and XMM-EPIC X-ray emission, it distinguishes between a *low* and a *high* state, but does not attribute them to periastron or apastron orbital phases. Also, the emissions were recorded during very different phases of the long-term modulation Θ (Eq. 4.2, here taking the Gregory (2002) value $P_{\text{long}} = 1667$ days), resulting in a mix of all long-term phases.

The SED shown in Figure 4.10 uses the data plotted in Fig. 7 of Sidoli et al. (2006), but divides them into periastron and apastron, where possible. Here, periastron is defined as the orbital phase range

$\Phi = 0.0 - 0.5$, and apastron $\Phi = 0.5 - 1.0$ (same intervals used in Ackermann et al. 2013, Jaron & Massi 2014, and Jaron et al. submitted). The issue of mixing data from all over the long-term modulation remains, however. In addition, optical photometric data from Paredes-Fortuny et al. (2015), X-ray and VHE γ -ray data from Anderhub et al. (2009), and X-ray data from Esposito et al. (2007) were included.

4.8 The GeV emission from LS I +61°303 observed by *Fermi*-LAT

The γ -ray space telescope *Fermi*-LAT has been observing the entire sky every three hours since August 4 2008 (Atwood et al. 2009). Figure 4.11 shows the counts map for a region 15° around LS I +61°303 including all *Fermi*-LAT data from the beginning (MJD 54682) till January 4 2015 (MJD 57391) using the energy range 0.1–300 GeV. Sourced included in the *Fermi*-LAT third source catalog (3FGL, Acero et al. 2015) are marked by green crosses, and associated sources are labelled. Clearly LS I +61°303 is the brightest source of γ -rays in this region of interest.

4.9 Related objects

There are two phenomena described in this introduction to the binary star LS I +61°303, which deserve further discussion.

First, the compact object in LS I +61°303 is possibly a black hole, while the companion is a Be type star, which would make the system belong to the class of Be-BH binaries, which is expected to be very small (Belczynski & Ziolkowski 2009). In Subsection 4.9.1 we report on the first case of a proven Be-BH binary, which allows to compare the phenomena observed in this object to LS I +61°303.

Second, the precession period of the jet is very close to the orbital period in LS I +61°303. This phenomenon has been observed in another binary system, GRO J1655-40, which we introduce in Subsection 4.9.2.

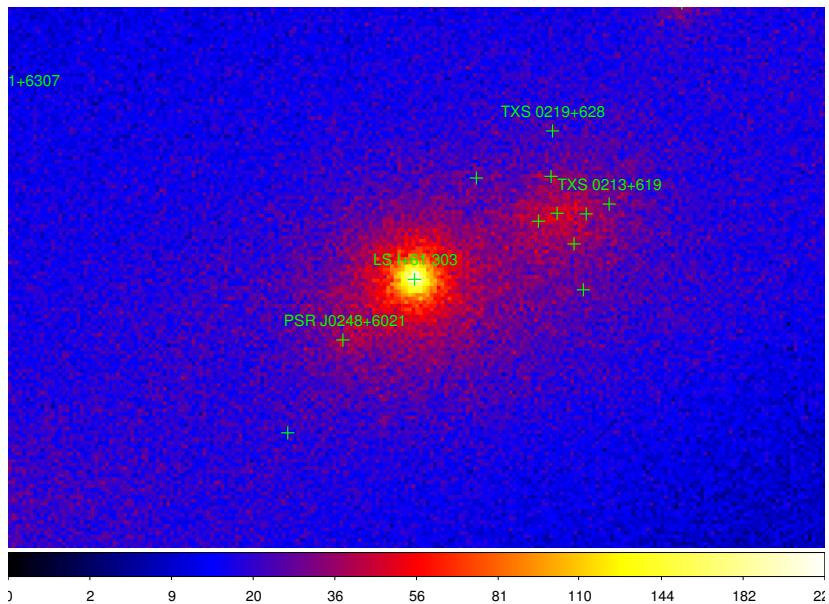


Figure 4.11: Counts map of the *Fermi*-LAT observations of the region around LS I +61°303, clearly the brightest source here. This counts map includes data from MJD 54682–57391 in the energy range 0.1–300 GeV. Sources included in the 3FGL catalog (Acero et al. 2015) are indicated by green crosses.

4.9.1 The Be-BH binary MWC 656

The binary system MWC 656 was first detected in the high energy γ -ray regime by the AGILE satellite (Lucarelli et al. 2010, confirmed by Alexander & McSwain 2015). Shortly after that first detection the Be type star MWC 656 was found in the error circle (Williams et al. 2010). The binary nature of this object was first considered by Casares et al. (2012), and a confirmation of this hypothesis together with the result of this object being the first proven case of a Be type star with a black hole companion was given by Casares et al. (2014). In Chapter ?? we will give details about the detection of radio emission from MWC 656 by Dzib et al. (2015). The existence of MWC 656 shows that nature can produce Be-BH binary systems (see Grudzinska et al. 2015 for a theoretical model for the binary evolution of MWC 656).

4.9.2 The fast precessing jet of GRO J1655-40

The binary star GRO J1655-40 consists of an F type star and a black hole with an orbital period of $P_{\text{orbit}} = 2.601 \pm 0.027$ days (Bailyn et al. 1995). The source features episodic ejection of relativistic jets, the jet precession with a period of $P_{\text{precession}} = 3 \pm 0.2$ days (Hjellming & Rupen 1995). The fact that the orbital period is close to the precession period of the jet puts this source in a relationship to LS I +61°303. Although a theoretical explanation for a mechanism which forces the two periods to synchronize has not been elaborated yet, the observation of now two objects with this characteristic can help for a better understanding of this phenomenon.

Chapter 5

Prediction of the radio outbursts of LS I +61°303

Credit: Jaron, F., & Massi, M., A&A, 559, A129, 2013, reproduced with permission © ESO.

Abstract

In the gamma-ray binary LS I +61°303, radio outbursts occur every 26.70 days and are modulated by a long-term periodicity of 1667 days. Until now the prediction of the periodical radio outbursts has been made using the orbital period $P_1 = 26.4960 \pm 0.0028$ days. This procedure implies timing residuals up to ~ 7 days affected by a systematic error with a sawtooth pattern. On the other hand, the direct use of the known periodicity of the radio outbursts, that is of $P_{\text{outburst}} = P_{\text{average}} = 26.70 \pm 0.05$ d, is prevented because of a time variable phase term. Our aim is to analyze this phase term and determine its exact value at each given epoch. First, we modeled the systematic sawtooth pattern affecting the timing residuals between the observed outbursts and those predicted by P_1 . Then, we removed this pattern from 6.7 yr of 8.3 GHz Green Bank Interferometer radio data to generate noise-limited residuals. Finally, we determined a criterion to determine the phase term based on the number of elapsed cycles of the

long-term modulation at a given epoch. The prediction of the outburst with $P = P_{\text{average}}$ is now straightforward and produces noise-limited timing residuals. This chapter was published as Jaron & Massi (2013).

5.1 Introduction

In 1995, Hjellming & Rupen (1995) discovered GRO J1655-40, the first case of a microquasar having a precessing radio jet with precessional period $P_{\text{prec}} = 3 \pm 0.2$ d (Hjellming & Rupen 1995) rather close to the orbital period $P_{\text{orbit}} = 2.601 \pm 0.027$ d (Bailyn et al. 1995). The source LS I +61°303 is a probable second case with a precessional period $P_2 = 26.92 \pm 0.07$ d of the radio jet (Massi & Jaron 2013) very close to the orbital period $P_1 = 26.4960 \pm 0.0028$ d (Gregory 2002; Grundstrom et al. 2007). Fast variations of the radio structure in LS I +61°303 were the results from MERLIN observations (Massi et al. 2004) and have been confirmed by VLBA observations by Dhawan et al. (2006), there interpreted as due to a cometary tail of a pulsar. Radio spectral index analysis (Massi & Kaufman Bernadó 2009), 3D simulations (Romero et al. 2007), and VLBA images (Massi et al. 2012) indicated, however, a microquasar scenario and the radio astrometry of 27-28 d suggested a slightly different value of the precession period from the orbital one (Massi et al. 2012). Finally, timing analysis resulted in $P_2 = 26.92 \pm 0.07$ d (Massi & Jaron 2013). Lense-Thirring precession has been invoked as a possible mechanism in both objects, for GRO J1655-40 by Martin et al. (2008), and for LS I +61°303 by Massi & Zimmermann (2010).

In addition to these two periods, i.e., the orbital one P_1 and the precessional one P_2 , the radio properties of LS I +61°303 feature two additional periods. Ray et al. (1997) determined a $P = 26.69 \pm 0.02$ d for the periodical large radio outburst. Gregory (2002) determined a $P = 1667 \pm 8$ d for a long-term periodicity modulating the radio outbursts. Massi & Jaron (2013) show that the intrinsic periodicities of the source are the orbital period $P_1 = 1/\nu_1$ and the precessional period $P_2 = 1/\nu_2$ giving rise to a beating which results in a $P_{\text{average}} = 2/(\nu_1 + \nu_2) = P_{\text{outburst}} = 26.70 \pm 0.05$ d, con-

sistent with the period found by Ray et al. (1997), modulated by a $P_{\text{long}} = 1/(\nu_1 - \nu_2) = 1667 \pm 393$ d, consistent with the long-term periodicity determined by Gregory (2002).

The importance of LS I +61°303 has grown after the detection of emission in the TeV band (Albert et al. 2006). Nowadays, the source is observed at all wavelengths of the electromagnetic spectrum. In addition LS I +61°303 is now included in the search for neutrino sources. While the high energy emission could be due to Inverse Compton, i.e., of leptonic origin, there could also be a hadronic component. The source LS I +61°303 and other gamma-ray binaries could therefore play a role as accelerators of Galactic cosmic rays (Romero et al. 2005; Abbasi et al. 2012). What sets LS I +61°303 apart from other gamma-ray binaries is its periodicity; however, this has not yet been fully exploited because of the uncertainty in predictions of its outburst. In fact, P_{average} , that is the periodicity of the outbursts, cannot be used directly for predictions because of its periodical reset at the minimum of the long-term modulation inherent to the beating process (Massi & Jaron 2013). On the other hand, using P_1 to predict the occurrence of the radio outbursts implies timing residuals between predicted and observed outbursts up to ~ 7 d and is affected by a systematic trend with a saw-tooth pattern (Gregory et al. 1999, see their Fig. 2). In this paper we aim to determine the best procedure for predicting the periodical radio outburst. We determine the reset affecting P_{average} and compare the procedures using P_1 and P_{average} .

5.2 Timing residuals

In this section we analyze the timing residuals defined as the difference between observed and predicted outburst times, for a given period. We use the Green Bank Interferometer (GBI) radio data at 8.3 GHz for this analysis. They cover the interval from 49379.975 MJD to 51823.441 MJD. During the minimum of the long-term modulation the outburst loses its characteristic shape and becomes a broad low curve without a definite peak (Paredes et al. 1990). We find this phase, defined by Paredes et al. (1990) as “quiet phase”, also in the GBI data,

in the interval 50500 MJD to 51000 MJD, where no maxima occur and where consequently large timing residuals would affect our tests for P_1 and P_{average} . We therefore remove this interval that biases our analysis. This interval in terms of the long-term modulation phase Θ ,

$$\Theta = \frac{t - t_0}{P_{\text{long}}} - \text{int} \left(\frac{t - t_0}{P_{\text{long}}} \right), \quad (5.1)$$

with $t_0 = 43366.275$ MJD and $P_{\text{long}} = 1667$ d, corresponds to $\Theta = 0.28 - 0.58$, which is therefore the interval where no clear radio outbursts occur.

5.2.1 Prediction using the orbital period P_1

Gregory et al. (1999) showed (see their Figs. 2 and 8) that when radio outbursts are predicted to occur with P_1 then there are residuals of -5.5 to $+7$ days, and that these residuals follow a sawtooth trend. In this section we analytically determine the sawtooth function and remove it from the data to finally obtain noise-limited residuals. These residuals are compared to residuals based on P_{average} in the next section.

We divided the GBI data into bins of size $P = P_1$. A direct search for the data point with the greatest flux within each bin gives a residual of

$$\Delta t_i = t_{\text{max},i} - t_i. \quad (5.2)$$

One sees that the resulting timing residuals in Fig. 5.1 a are not dominated by noise; on the contrary, a systematic pattern is present. The shape, as pointed out by Gregory et al. (1999), is a sawtooth pattern with a gradual rise and a rapid fall, and periodicity P_{long} equal to that present in the peak flux. This long-term modulation was first calculated to be about 1584 d (Gregory et al. 1999) and later established to be 1667 ± 8 d (Gregory 2002). The analytical shape for the sawtooth function has been determined in Massi & Jaron (2013) to be ¹

$$\tau(t) = m \cdot \text{fmod}(t, 1667) + c. \quad (5.3)$$

¹fmod is a function implemented in the math library of C.

We remove $\tau(t)$ from the timing residuals shown in Fig. 5.1 a and compute the standard deviation σ for the noise-limited residuals. We minimize σ by varying m . Figure 5.1 b shows the difference between the data in Fig. 5.1 a and the sawtooth function. Figure 5.1 b, with $\sigma = 1.87$ d, will therefore be our term of quantitative comparison when using P_{average} in the next section.

5.2.2 Predictions with P_{average}

To predict the outburst occurrence in LS I +61°303 one generally determines for a given epoch that time t for which $\Phi(P_1) = 0.6$, where

$$\Phi = \frac{t - t_0}{P_1} - \text{int} \left(\frac{t - t_0}{P_1} \right), \quad (5.4)$$

with $t_0 = 43366.275$ MJD. This method follows from the analysis of the orbital shift by Paredes et al. (1990). During the maximum of the long-term periodicity of 1667 d the outburst occurs at $\Phi(P_1) = 0.6$. This, in terms of the timing residuals in Fig. 5.1 a, corresponds to a delay of zero; afterwards the phase of the outbursts increases until a maximum of about $\Phi(P_1) = 0.9$ (Paredes et al. 1990). In terms of the timing residuals in Fig. 5.1 a, this corresponds to a timing residual of $(0.9 - 0.6)P_1 \simeq 8$ d. The jump in the sawtooth function from maximum positive delay to maximum negative delay occurs when the peak of the outburst, after the nearly quiescent period at the minimum, appears again but at an earlier phase than $\Phi = 0.6$, i.e., at phase $\Phi = 0.4$ (Paredes et al. 1990). In terms of timing residuals this corresponds to $(0.4 - 0.6)P_1 = -5$ d.

Here we show that the procedure above described to predict the outburst occurrence should be replaced by the determination whether $\Phi(P_{\text{average}}) = 0.7$ or $\Phi(P_{\text{average}}) = 0.2$ (as in Eq. (5.4) with P_{average} instead of P_1), where the ambiguity between 0.7 or 0.2 is determined as shown in the next section. We demonstrate by the residuals how effective this procedure is.

We compute the timing residuals for P_{average} following the procedure of Sect. 2.1 for $P = P_{\text{average}}$; the residuals are shown in the lower panel of Fig. 5.2. The value in Massi & Jaron (2013) for P_{average} is

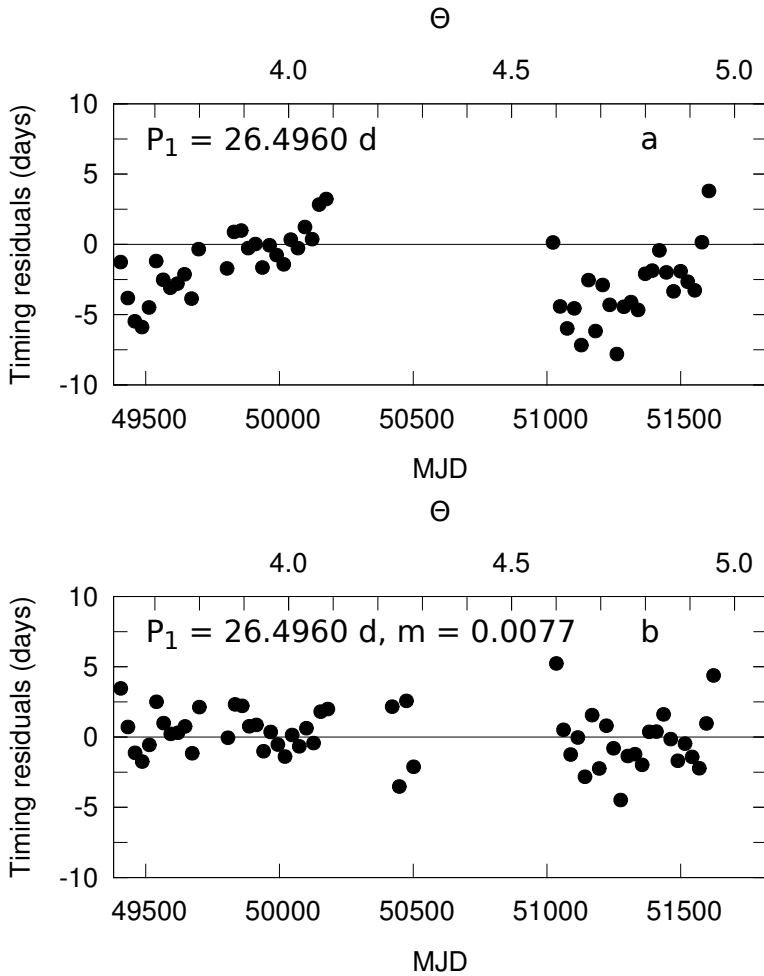


Figure 5.1: a: Timing residuals for the radio outbursts expected to occur with orbital periodicity P_1 . b: Difference between the residuals from Fig. 5.1 a and the sawtooth function discussed in Sect. 5.2.1.

26.70 ± 0.05 d. Therefore, we compute the value of P_{average} minimizing the standard deviation σ of the residuals for a number of trial periodicities equally distributed in $P = 26.65 - 26.75$ d, i.e., within the error bar given in Massi & Jaron (2013). In the plot, the minimum σ shows a plateau with center at 26.704 d and a half width of 0.04 d, that define therefore our improved value for P_{average} and its error.

The residuals in Fig. 5.2 Bottom have $\sigma = 1.60$ d, even slightly better than the “residuals of the residuals” with $\sigma = 1.87$ d shown in Fig. 5.1 b, obtained by the complex removal of the sawtooth function from the residuals in Fig. 5.1 a.

5.2.3 Determination of the periodical reset

Figure 5.3 shows that the folding of the data with the orbital and precessional periods P_1 and P_2 results in one clustering in both cases, whereas the folding with P_{average} , which is simply their average and therefore one might expect an intermediate clustering, results in a double clustering. In particular, all data before the minimum of the long-term modulation P_{long} (black in Fig. 5.3) cluster at one phase, and all points after the minimum (green) cluster at the other phase. This is what a beat of P_1 and P_2 predicts: At the minimum of P_{long} the function in P_2 has arrived at a delay with respect to the function in P_1 equal to $P_1/2$, then one cycle later it precedes the function in P_1 instead of lagging behind it as before the minimum. This gives rise to a jump in the function in P_{average} , being $f(P_{\text{average}})$ always between $f(P_1)$ and $f(P_2)$ (Massi & Jaron 2013).

From our tests we find that the phase Φ_{outburst} changes during every minimum of the long-term modulation such that

$$\Phi_{\text{outburst}} = \begin{cases} 0.7 & \text{for } K \text{ even,} \\ 0.2 & \text{for } K \text{ odd.} \end{cases} \quad (5.5)$$

Here, the integer number K counts the long-term modulation cycles for $t \geq 49174$ MJD

$$K = \text{int} \left(\frac{t - 49174 \text{ MJD}}{P_{\text{long}}} \right), \quad (5.6)$$

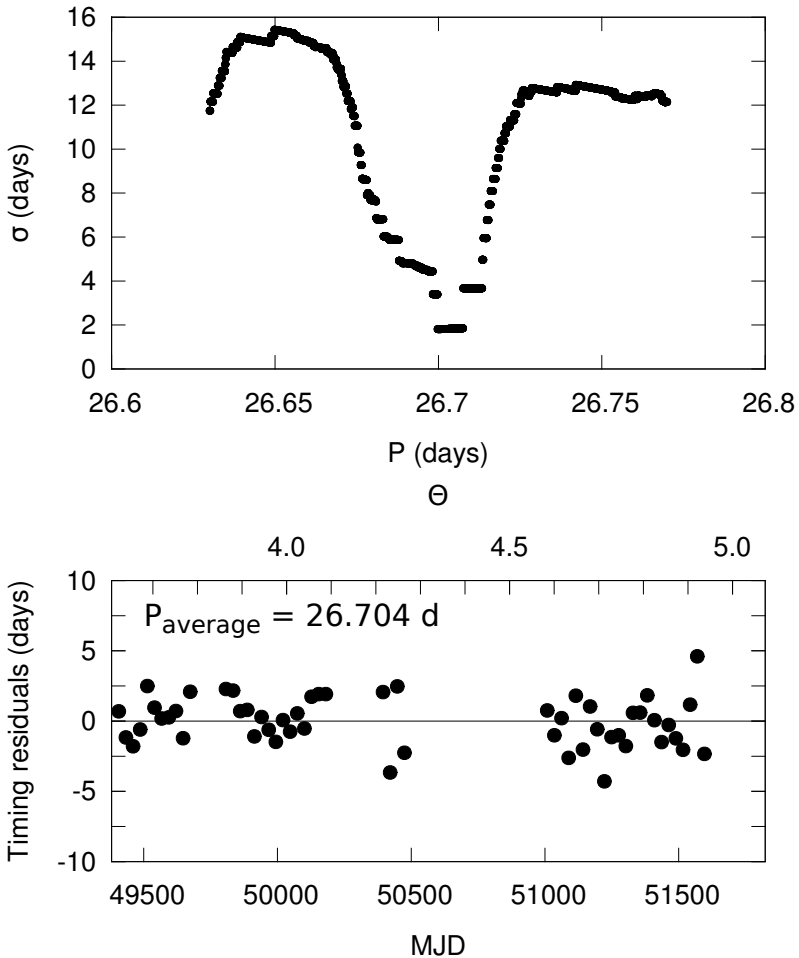


Figure 5.2: Top: The standard deviation σ as a function of the periodicity P_{average} of the radio outbursts. Bottom: Timing residuals for the assumption that the outbursts occur with a periodicity of $P_{\text{average}} = 26.704 \text{ d}$ and that there is a phase jump during the long-term minimum.

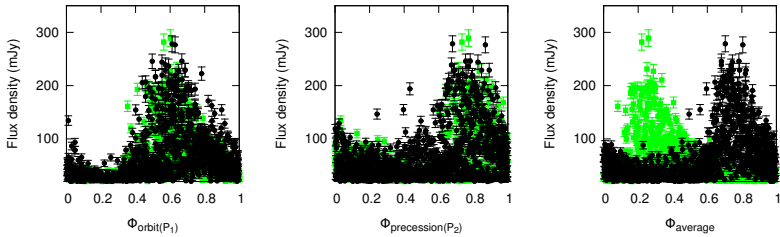


Figure 5.3: Left: 8.3 GHz GBI radio data vs Φ_{orbit} , where $\Phi_{\text{orbit}} (= P_1) = 26.49$ d. Middle: 8.3 GHz GBI radio data vs $\Phi_{\text{precession}}$, where $\Phi_{\text{precession}} (= P_2) = 26.92$ d. Right: 8.3 GHz GBI radio data vs Φ_{average} for $P_{\text{average}} = \frac{2}{\nu_1 + \nu_2} = 26.704$ d. Data before the minimum at 50841 MJD are black circles, data after 50841 MJD are green squares.

where $49174 \text{ MJD} = (50841 - 1667) \text{ MJD}$ is coincident with the time of the phase jump related to the GBI data (Massi & Jaron 2013).

For the purpose of illustrating the predicted times of outburst we use the function

$$f(t) = A \left[\frac{1}{2} + \frac{1}{2} \cos \left(\frac{2\pi}{P} (t - t_0) - 2\pi\Phi_{\text{outburst}} \right) \right]^n, \quad (5.7)$$

where A is a scaling factor which we set to 150 mJy to roughly match the average amplitude of the outbursts, P is the periodicity of the outbursts, $t_0 = 43366.275$ MJD as usual, Φ_{outburst} is the phase of the outbursts, and n is an exponent to sharpen the peaks; we chose $n = 8$. In Fig. 5.4 two intervals of the GBI 8.3 GHz data are plotted together with the predicted outbursts. The continuous curve is the prediction made by Eq. (5.7) with $P = P_{\text{average}} = 26.704$ d and Φ_{outburst} computed according to Eq. (5.5). The dashed curve is the result inserting P_1 and $\Phi_{\text{outburst}} = 0.6$. There are times when the prediction with the orbital period P_1 is quite accurate, as shown in Fig. 5.4 b, but in Fig. 5.4 a, e.g., the deviations from the predictions are as large as several days. The prediction with $P = 26.704$ d and setting Φ_{outburst} according to the number K is in good agreement with the observations in both cases.

5.3 Conclusions

The usual procedure used until now to predict the outburst occurrence is based on the orbital period $P_1 = 26.4960 \pm 0.0028$ d. Recently, Massi & Jaron (2013) determined that the periodicity of the radio outburst is $P_{\text{average}} = 26.70 \pm 0.05$ d. However, the direct use of P_{average} is not possible because of the phase jump during the minimum of the long-term modulation. In this paper we determined a straightforward way of calculating the phase term and therefore of predicting the radio outbursts using P_{average} . We obtained the following results:

1. We showed that the standard deviation of the timing residuals becomes minimal and equal to $\sigma = 1.6$ d for a periodicity of $P_{\text{average}} = 26.704 \pm 0.004$ d when taking into account the phase jump of 0.5 during the minimum of the long-term modulation. This value of P_{average} is our new improved estimation of the periodicity of the observed radio outbursts.
2. The quantity which resets the phase Φ_{outburst} is the integer number of long-term cycles K as introduced in Eq. (5.6). The phase Φ_{outburst} is either 0.2 or 0.7 depending on whether K is odd or even, respectively, as described in Eq. (5.5).
3. We confirm the results of Paredes et al. (1990) that during the minimum of the long-term modulation not only is the outburst low, but it even becomes a broad curve without a definite peak. We established that this occurs in the interval $\Theta = 0.28 - 0.58$.

Acknowledgements

We thank James Urquhart, Lisa Zimmermann, and Jürgen Neidhöfer for reading the manuscript and for useful discussions and the anonymous referee for constructive comments which improved the paper. The Green Bank Interferometer is a facility of the National Science Foundation operated by the NRAO in support of NASA High Energy Astrophysics programs.

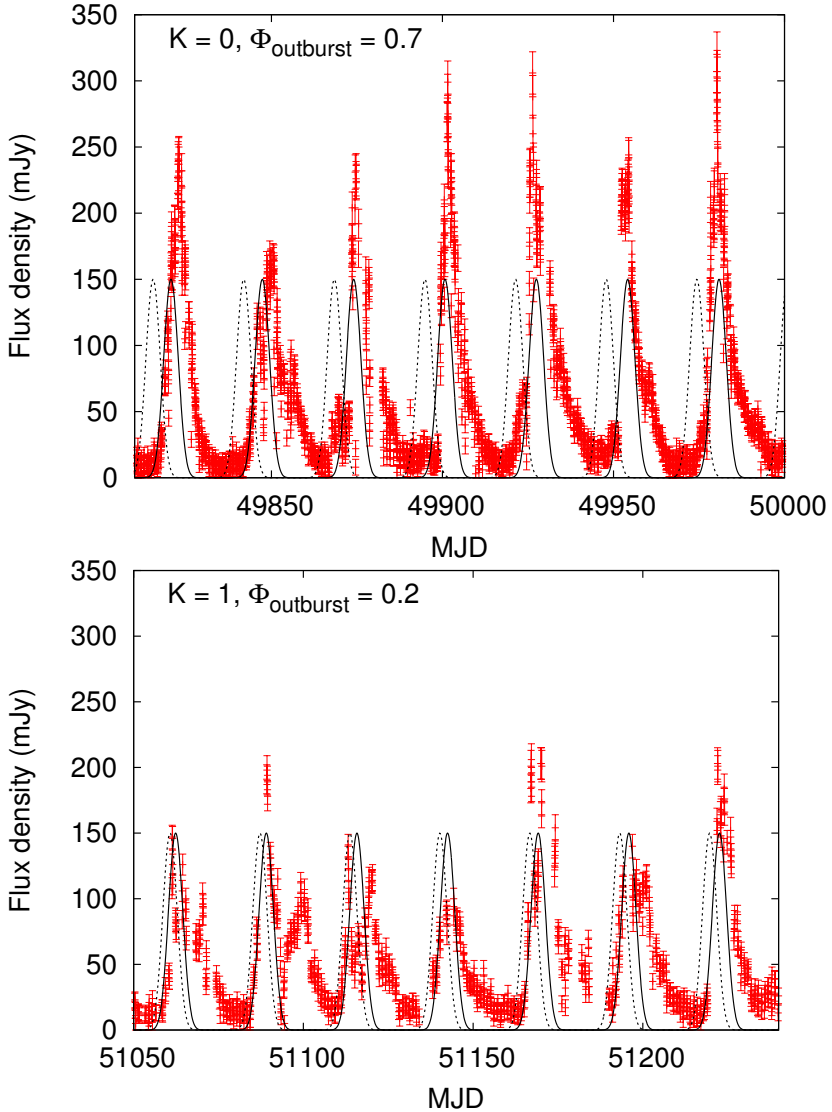


Figure 5.4: Illustration of the predicted outbursts, GBI 8.3 GHz data in red, prediction with $P = P_1$ as a dashed line, and prediction with $P = P_{\text{average}}$ with phase jump as a continuous line, top: time interval with a clear difference between the two predictions, bottom: time interval where the prediction with P_1 is also in good agreement with the observation.

Chapter 6

Discovery of a periodic apastron GeV peak in LS I +61°303

Credit: Jaron, F., & Massi, M., A&A, 572, A105, 2014, reproduced with permission © ESO.

Abstract

The aim of this paper is to analyse the previously discovered discontinuity of the periodicity of the GeV γ -ray emission of the radio-loud X-ray binary LS I +61°303 and to determine its physical origin. We used wavelet analysis to explore the temporal development of periodic signals. The wavelet analysis was first applied to the whole data set of available *Fermi*-LAT data and then to the two subsets of orbital phase intervals $\Phi = 0.0 - 0.5$ and $\Phi = 0.5 - 1.0$. We also performed a Lomb-Scargle timing analysis. We investigated the similarities between GeV γ -ray emission and radio emission by comparing the folded curves of the *Fermi*-LAT data and the Green Bank Interferometer radio data. During the epochs when the timing analysis fails to determine the orbital periodicity, the periodicity is present in the two orbital phase

intervals $\Phi = 0.0 - 0.5$ and $\Phi = 0.5 - 1.0$. That is, there are two periodical signals, one towards periastron (i.e., $\Phi = 0.0 - 0.5$) and another one towards apoastron ($\Phi = 0.5 - 1.0$). The apoastron peak seems to be affected by the same orbital shift as the radio outbursts and, in addition, reveals the same two periods P_1 and P_2 that are present in the radio data. The γ -ray emission of the apoastron peak normally just broadens the emission of the peak around periastron. Only when it appears at $\Phi \approx 0.8 - 1.0$, because of the orbital shift, it is enough detached from the first peak to become recognisable as a second orbital peak, which is the reason why the timing analysis fails. Two γ -ray peaks along the orbit are predicted by the two-peak accretion model for an eccentric orbit, that was proposed by several authors for LS I +61°303.

6.1 Introduction

The system LS I +61°303 with an orbital period $P_1 = 26.4960 \pm 0.0028$ days (Gregory 2002) consists of a compact object and a massive star with an optical spectrum typical for a rapidly rotating B0 V star (Casares et al. 2005; Grundstrom et al. 2007).

In 2009 the first detection of orbital periodicity in high-energy gamma rays (20 MeV–100 GeV) was reported by using the Large Area Telescope (LAT) from the *Fermi* Gamma-Ray Space Telescope spacecraft (Abdo et al. 2009a). Longer monitoring has shown (Hadasch et al. 2012; Ackermann et al. 2013) that indeed the system shows a clear periodical outburst towards periastron ($\Phi_{\text{periastron}} = 0.23$, Casares et al. 2005) at some epochs, but that this periodicity is not always present. This is different from the behaviour of the system in the radio band where not only periodical outbursts occur at each orbit, even if modulated with a long-term period ($P_{\text{long}} = 1667 \pm 8$ d, Gregory 2002), but they also occur towards apoastron and not towards periastron as in the GeV energy band (e.g., see Fig. 2 c in Massi & Kaufman Bernadó 2009).

Along with this different behaviour between high and low energy there is a puzzling overlap. Ackermann et al. (2013) noticed that GeV

data also show the long-term periodical variation affecting the radio data, but only at a specific orbital phase interval, $\Phi = 0.5 - 1.0$, that is around apoastron.

The aim of this paper is to investigate the discontinuity in the periodicity of the GeV γ -ray emission at periastron, the relationship of its disappearance with the variation of the emission in other parts of the orbit, and finally the possible relationship between GeV and radio emission. Section 6.2 describes our data analysis. In Sect. 6.3 we present our results and in Sect. 6.4 our conclusions.

6.2 Data analysis

In this section we present the data reduction of *Fermi*-LAT data performed with three packages: the *Fermi* science tools package (version v9r33p0)¹, the wavelet analysis², and the software Starlink³.

The γ -ray data used in this analysis span the time period MJD 54683 (August 05, 2008) to MJD 56838 (June 30, 2014). We used the script `like_lc.pl` by Robin Corbet.⁴ Only source-event-class photons were selected for the analysis. Photons with a zenith angle greater than 100° were excluded to reduce contamination from the Earth's limb. For the diffuse emission we used the model `gll_iem_v05_rev1.fit` and the template `iso_source_v05_rev1.txt`. We used the instrument response function (IRF) `P7REP/background_rev1`, and the model file was generated from the 2FGL catalogue (Nolan et al. 2012), all sources within 10° of LS I +61 $^\circ$ 303 were included in the model. LS I +61 $^\circ$ 303 was fitted with a log-parabola spectral shape and with all parameters left free for the fit, performing an unbinned maximum likelihood analysis. The other sources were fixed to their catalogue values. We produced light curves with a time bin size of one day and of five days. For all light curves we used an energy range of 100 MeV to 300 GeV.

¹<http://fermi.gsfc.nasa.gov/ssc/data/analysis/software/>

²<http://atoc.colorado.edu/research/wavelets/>

³<http://www.starlink.rl.ac.uk/>

⁴<http://fermi.gsfc.nasa.gov/ssc/data/analysis/user/>

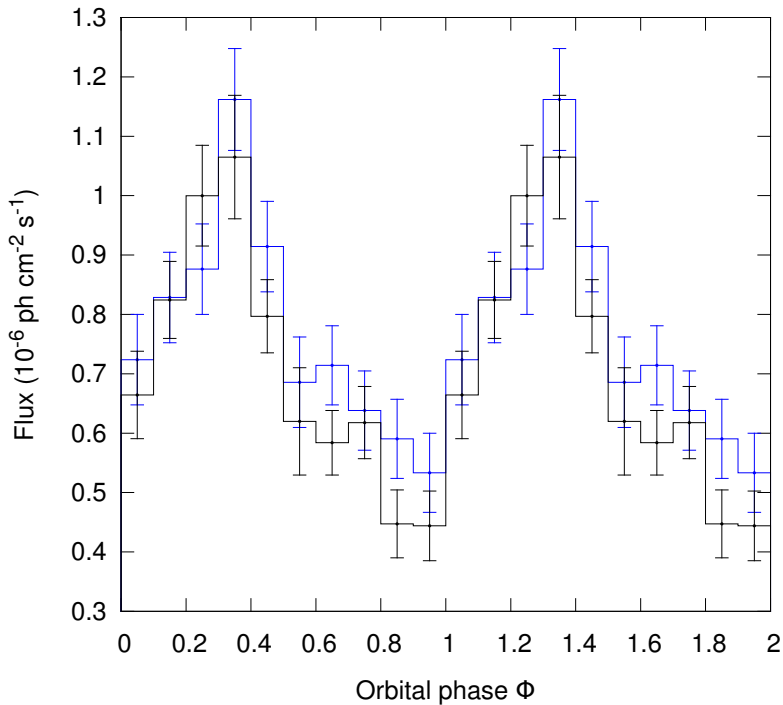


Figure 6.1: Folded light curve (blue) of Fig. 8 by Hadasch et al. (2012). This covers the first 8 months of *Fermi*-LAT observations. As comparison we give our folded data (black) from the same time interval. This time interval corresponds to $\Theta = 6.79 - 6.92$.

The data were folded with the orbital phase defined as

$$\Phi = \frac{t - t_0}{P_1} - \text{int} \left(\frac{t - t_0}{P_1} \right), \quad (6.1)$$

where $t_0 = 43366.275$ MJD and $P_1 = 26.4960 \pm 0.0028$ d is the orbital period of the binary system (Gregory 2002).

We investigated the temporal evolution of the orbital periodicity by means of a wavelet analysis with Morlet function (Torrence & Compo 1998). The wavelet analysis decomposes the one-dimensional time series into a two-dimensional time-frequency space and displays the

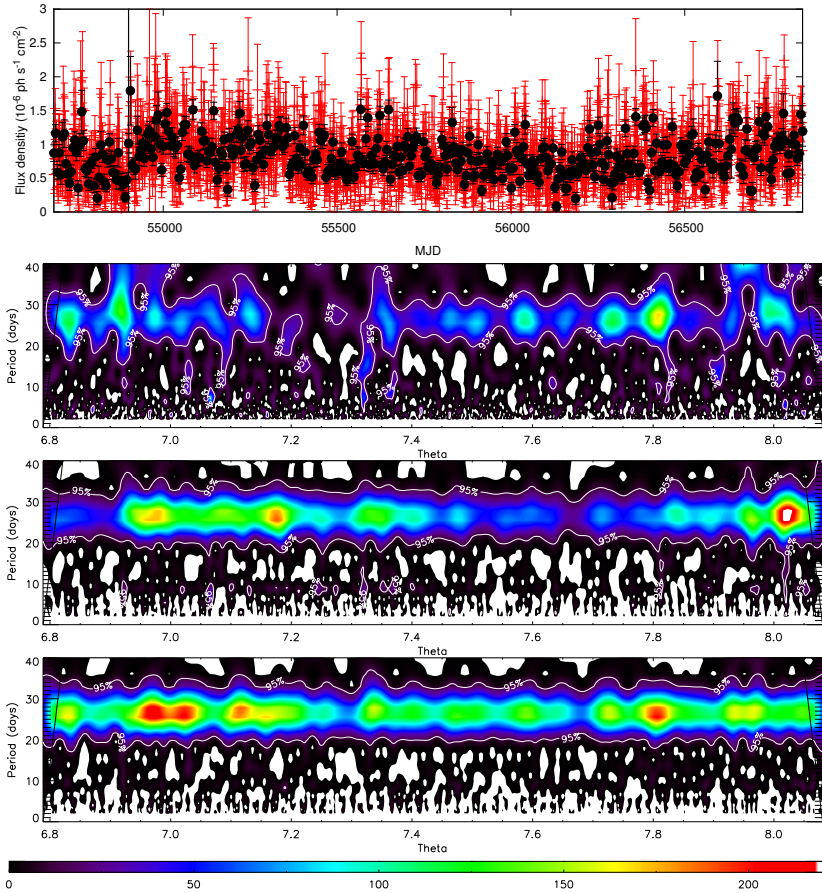


Figure 6.2: Wavelet analysis of *Fermi*-LAT data. The strength of periodicity is colour coded as indicated in the bottom bar. First row: *Fermi*-LAT data with a time bin of 5 d (black) are overplotted on *Fermi*-LAT data with a time bin of 1 d (red). The black line marks the point of flux change reported by Hadasch et al. (2012) which is also visible in our light curve. Second row: Wavelet analysis for the whole data set, that is for the whole orbital interval 0.0 – 1.0 (b–d use a time bin of one day). Third row: Wavelet analysis for half the data set, that is for the orbital interval $\Phi = 0.5 - 1.0$, i.e., around apoastron. Fourth row: Wavelet for half the data set, that is for the orbital interval $\Phi = 0.0 - 0.5$, i.e., around periastron.

power spectrum in a two-dimensional colour-plot that shows how the Fourier periods vary in time (Torrence & Compo 1998). While the wavelet analysis was applied to the γ -ray data vs time, for a straightforward comparison with radio data, we express the x -axis as

$$\Theta = \frac{t - t_0}{P_{\text{long}}}. \quad (6.2)$$

This allows a comparison with non-simultaneous radio data because the radio data are periodical in Θ . We will therefore compare gamma-ray data to radio data having the same fractional part of Θ . For the Lomb-Scargle timing analysis (Lomb 1976; Scargle 1982), we used the program PERIOD, which is part of the UK software Starlink. The version we used was 5.0-2 for UNIX. The wavelet analysis assumes regularly sampled data. We therefore set the data for the wavelet analysis to zero for missing flux. For the Lomb-Scargle analysis this was not necessary. As discussed in Sect. 3, the Lomb-Scargle analysis confirms and accurately determines the periodicities found with the wavelet analysis. In the Lomb-Scargle and wavelet analysis, significance levels for the spectra were determined with the Fisher randomisation, as outlined in Linnell Nemec & Nemec (1985), and with Monte Carlo simulations, as in Torrence & Compo (1998). The fundamental assumption is: if there is no periodic signal in the time series data, then the measured values are independent of their observation times and are likely to have occurred on any other order. One thousand randomized time-series were formed and the periodograms calculated. The proportion of permutations that give a peak power higher than that of the original time series would then provide an estimate of p , the probability that for a given frequency window there is no periodic component present in the data with this period. A derived period is defined as significant for $p < 0.01$, and a marginally significant period for $0.01 < p < 0.10$ (Linnell Nemec & Nemec 1985).

6.3 Results

In this section we discuss our wavelet and Lomb-Scargle results for the gamma-ray data and compare them with previously published results (Hadasch et al. 2012; Ackermann et al. 2013). Then we compare gamma-ray data with radio data.

6.3.1 Wavelet and Lomb-Scargle analysis

As a general check of our data reduction we verified the consistency of the folded curve of our data with the folded curve of Hadasch et al. (2012). For this purpose we selected the same time interval as in Hadasch et al. (2012), that is 54683–54900 MJD ($\Theta = 6.79 - 6.92$), covering the first eight months of *Fermi*-LAT observations. Figure 6.1 presents the result by Hadasch et al. (2012) and our results. We see how these independently calibrated data sets, which used different versions of the software, of the instrumental response function, etc., produce the same result: There is a main peak at orbital phase $\Phi \approx 0.35$.

We compare the light curve and wavelet results with previous results. The whole interval of the *Fermi*-LAT data used in our analysis is presented in Fig. 6.2 a. The point of flux change reported by Hadasch et al. (2012) is also visible in our light curve. Figure 6.2 b shows the wavelet analysis results for the whole data set. The orbital periodicity shows a minimum around $\Theta \approx 7.25$. This agrees with the periodograms of Fig. 7 in Hadasch et al. (2012), where the orbital periodicity is already almost absent for MJD 55044–55225 ($\Theta = 7.00 - 7.11$) and is completely absent at MJD 55405–55586 ($\Theta = 7.22 - 7.33$). The panels of Fig. 4 in Ackermann et al. (2013) show the decline in the orbital flux modulation in the interval MJD 55191–55698 ($\Theta = 7.1 - 7.5$). Our Figs. 6.1, 6.2 a and 6.2 b therefore confirm the orbital modulation that peaks around periastron, the point of flux change at $\Theta \approx 6.95$, and the lack of orbital flux modulation at $\Theta \approx 7.25$ previously discovered and discussed in Hadasch et al. (2012) and Ackermann et al. (2013).

Now we examine the new results obtained when the wavelet analysis is performed separately for emission around periastron, $\Phi = 0.0 -$

0.5, and emission around apoastron, $\Phi = 0.5 - 1.0$. By comparing Fig. 6.2 d with Fig. 6.2 c it is clear that the orbital periodicity is not a characteristic of periastron emission alone, it is also present at apoastron, at least at some Θ s. At $\Theta \approx 7.2$ where the wavelet analysis for the whole data set (Fig. 6.2 b) shows the minimum power for the orbital periodicity, a maximum is present in Fig. 6.2 c. Orbital flux modulation is present from $\Theta \approx 6.95$ to $\Theta \approx 7.40$, and at $\Theta \approx 7.95$ the periodicity is strong again, indicating a repetition consistent with the long-term period P_{long} . This confirms the discovery of Ackermann et al. (2013) that in the orbital phase interval $\Phi = 0.5 - 1.0$ the γ -ray flux shows periodical variation with a period equal to the long-term modulation affecting the radio outburst. In addition, our wavelet analysis shows that the emission at apoastron, affected by the long-term modulation, is orbitally modulated.

We checked the presence of the orbital and long-term periodicities that were indicated by the wavelet analysis with the Lomb-Scargle timing analysis of the data from $\Phi = 0.5 - 1.0$. First of all, the periodogram of the subset $\Phi = 0.5 - 1.0$, shown in Fig. 6.3 d, presents a periodicity at 1705 ± 355 days, confirming the result of Ackermann et al. (2013) of a long-term modulation of emission around apoastron. Moreover, the periodogram shows a feature at the orbital period P_1 , confirming the results of the wavelet analysis, and this feature seems to have a complex profile. The zoomed version is presented in Fig. 6.3 e. Figure 6.3 f shows the periodogram for data integrated over five days. There is one peak at $P_1 = 26.48 \pm 0.08$ d and another one at $P_2 = 26.99 \pm 0.08$ d. When we consider the whole data set, which is the longest time interval of *Fermi*-LAT data analysed so far, P_{long} and P_2 are significant in the randomisations tests (i.e., the probability p that there is no periodic component present in the data with these periods is for both periods $p < 0.01$), even if they are rather weak features in the periodograms of Fig. 6.3 a, b, and c. For the emission around periastron, Figures 6.3 g, h, and i show the Lomb-Scargle periodograms of $\Phi = 0.0 - 0.5$. Here the only outstanding feature is P_1 .

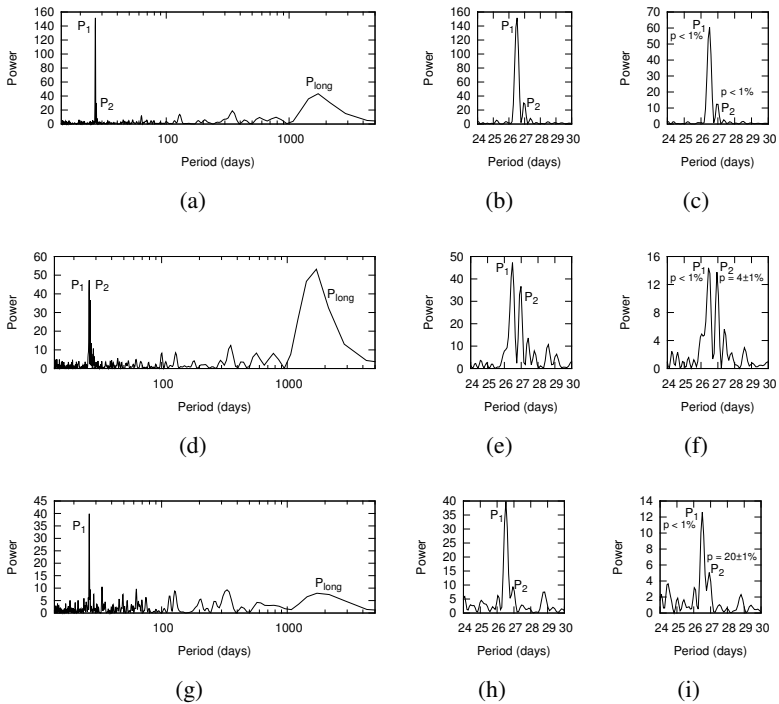


Figure 6.3: Lomb-Scargle periodogram of the *Fermi*-LAT data (with a time bin of one day). (a) Full data set: data in the orbital phase $\Phi = 0.0 - 1.0$. (b) Zoom of Fig. 6.3 a. (c) Same as Fig. 6.3 b for data with a time bin of 5 days. The false alarm probability (p) resulting from randomisation tests is indicated. A period is defined as significant for $p < 1\%$, and as marginally significant for $1\% < p < 10\%$ (Sect. 2). (d) Half the data set: data in the orbital phase $\Phi = 0.5 - 1.0$. The periods P_2 and P_{long} here present are typical periodicities in radio data (Massi & Jaron 2013). (e) Zoom of Fig. 6.3 d. (f) Same as Fig. 6.3 e for data with a time bin of 5 d. (g) Half the data set: data in the orbital phase $\Phi = 0.0 - 0.5$. (h) Zoom of Fig. 6.3 g. (i) Same as Fig. 6.3 h for data with a time bin of 5 d.

6.3.2 Orbital shift

Why does the timing analysis reveal a lack of orbital modulation around $\Theta \approx 7.2$ with a peak at periastron passage when the periodicity is still present, as shown in Fig. 6.2 d for data at $\Phi = 0.0 - 0.5$? And why does the orbital modulation of GeV emission towards apoastron get stronger in that Θ -interval (Fig. 6.2 c)? Clearly, the second question is the answer to the first. Two peaks along the orbit disturb the timing analysis. The curves shown in Fig. 6.4 a, b, and c refer to the three consecutive Θ -intervals around the minimum of Fig. 6.2 b, that is around the peak of Fig. 6.2 c: $\Theta = 7.12 - 7.22$ (MJD 55235–55402), $\Theta = 7.22 - 7.32$ (MJD 55402–55569), and $\Theta = 7.32 - 7.42$ (MJD 55569–55743). In addition to the peak at periastron Fig. 6.4 a and Fig. 6.4 b show a second peak in the interval $\Phi = 0.8 - 1.0$.

The real question therefore is why periodical emission towards apoastron is detected only at $\Theta \approx 7.2$. The important information from the Lomb-Scargle analysis is that there are two periods, P_1 and P_2 , as is for radio data (Massi & Jaron 2013). We therefore examined the trend of radio data in that particular Θ -interval. Figure 4 d shows the GBI data at 8 GHz at $\Theta = 4.23 - 4.40$. The curve shows indeed a peak at $\Phi \approx 0.9$ consistent with the second peak in the GeV data in the interval $\Phi = 0.8 - 1.0$ (Fig. 6.4 a-b). Figure 4 d also shows data at $\Theta = 3.79 - 3.92$, as the GeV data of our Fig. 6.1. In this case, the radio data show a peak at $\Phi \approx 0.65$ consistent with the bump of emission at $\Phi \approx 0.65$ in the gamma-ray data of Fig. 6.1. This is the well-known phenomenon of the orbital shift of the radio outburst in LS I +61°303: The largest outbursts occur at orbital phase 0.6, afterwards, with the long-term periodicity, the orbital phase of the peak of the outburst changes, as analysed by Paredes et al. (1990) in terms of orbital phase shift, by Gregory et al. (1999) in terms of timing residuals, and reproduced recently by the precessing jet model in Massi & Torricelli-Ciamponi (2014, their Fig. 4 b).

The second γ -ray peak, clearly associated with the radio outburst in terms of timing analysis, therefore also follows the same orbital shift. The second peak is therefore only detected at $\Theta \approx 7.2$, although the periodicity is indeed always present, because in that Θ -interval the peak

is detached enough from the first γ -ray peak to be discernable in the timing analysis.

6.4 Discussion and conclusion

The first eight months of the *Fermi*-LAT observations ($\Theta = 6.79 - 6.93$) analysed by Hadasch et al. (2012) indicate a peak of GeV γ -ray emission close to periastron. This clear orbital modulation of the GeV gamma-ray emission is lost at some time interval (Hadasch et al. 2012; Ackermann et al. 2013). The aim of this paper was to investigate the origin of this disappearance. Our results are the following:

1. In the interval $\Theta \approx 7.2$ (Fig. 6.2 b) where the timing analysis fails to find the orbital periodicity in GeV γ -ray emission, there are two periodical signals, one in the orbital phase interval $\Phi = 0.0 - 0.5$ (Fig. 6.2 d), that is towards periastron, the other in the interval $\Phi = 0.5 - 1.0$ (Fig. 6.2 c), that is towards apoastron. This result of two GeV peaks along the orbit corroborates the two-peak accretion model for LS I +61°303. The hypothesis that a compact object that accretes material along an eccentric orbit undergoes two accretion peaks along the orbit was suggested and developed by several authors for the system LS I +61°303 (Taylor et al. 1992; Marti & Paredes 1995; Bosch-Ramon et al. 2006; Romero et al. 2007). The first accretion peak is predicted to occur close to the Be star and to give rise to a major high-energy outburst. The second accretion peak is predicted to occur much farther away from the Be star, where the radio outburst occurs, and a minor high-energy outburst is predicted there (Bosch-Ramon et al. 2006). The predicted periastron event corresponds well to the observed GeV peak towards periastron, the second predicted high-energy outburst, corresponds well to the here discussed apoastron peak.
2. The Lomb-Scargle analysis of emission around apoastron (Fig. 6.3 d, e, f) revealed the same three periodicities $P_{1\gamma} = 26.48 \pm 0.08$ d, $P_{2\gamma} = 26.99 \pm 0.08$ d, and $P_{\text{long}\gamma} = 1705 \pm 335$ d

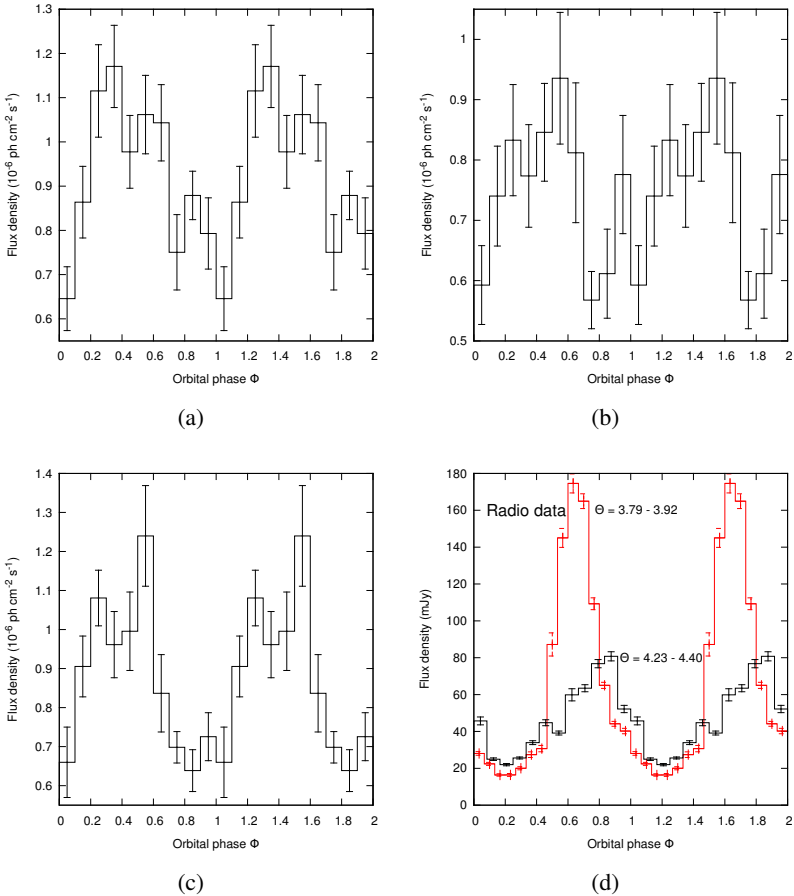


Figure 6.4: Apostron peak. *Fermi*-LAT gamma-ray data folded with the orbital periodicity $P_1 = 26.4960$ d for three consecutive Θ -intervals. (a) $\Theta = 7.12 - 7.22$ (MJD 55235–55402); (b) $\Theta = 7.22 - 7.32$ (MJD 55402–55569); (c) $\Theta = 7.32 - 7.42$ (MJD 55569–55740); there is a second peak at $\Phi = 0.8 - 1.0$, i.e., around apoastron. (d) GBI radio data at 8 GHz folded with orbital period $P_1 = 26.4960$ d. The two Θ -intervals are those considered in Fig. 6.1 and in this figure for *Fermi*-LAT data. The orbital phase of the peak of the two radio curves agrees well with those of the second peak in GeV curves.

that affect the radio emission: $P_{1\text{radio}} = 26.4960 \pm 0.0028$ d, $P_{\text{longradio}} = 1667 \pm 8$ d (Gregory 2002), and $P_{2\text{radio}} = 26.92 \pm 0.07$ d (Massi & Jaron 2013).

This second result confirms the previous result of P_1 in GeV emission around apoastron, and in addition reveals P_2 , only recently discovered in the radio emission by the timing analysis of 6.7 years of Green Bank Radio Interferometer (GBI) observations at the two frequencies of 2.2 GHz and 8.3 GHz (Massi & Jaron 2013). The radio data base of GBI and the data base of *Fermi*-LAT cover two quite different time intervals separated by 8 yr (the last scan in the GBI database is June 2000, whereas *Fermi*-Lat monitoring begins in August 2008). Moreover, the two monitorings have a quite different sampling rate (GBI with up to eight observations per day and large gaps, *Fermi*-LAT covers the whole sky over three hours, and we integrated over one day). Nevertheless, the timing analysis gives the same three periodicities (compare our Figs. 6.3 d, e, f with Figs. 1 and 2 b in Massi & Jaron 2013).

Figures 6.3 g, h, and i reveal a quite different characteristic for emission around periastron: the Lomb-Scargle analysis results in only one outstanding feature at $P_1 = 26.52 \pm 0.08$ d. The connection of P_{long} with P_2 is evident from Figs. 6.3 g and h: the lack of P_2 (or reduction at noise level) is associated with a lack of P_{long} (reduced at noise level). Simulations (Massi & Jaron 2013) with P_1 and the long-term modulation cannot reproduce the observed periodogram (i.e., P_2), whereas simulations with P_1 and P_2 directly produce the long-term modulation as their beating frequency $\nu_1 - \nu_2$.

While P_1 is related to the periodical accretion peak towards apoastron described above, the period P_2 is most likely related to the precession of the radio jet of LS I +61°303, see the agreement with the precessional period from VLBA astrometry, of 27–28 days (Massi et al. 2012). The hypothesis that a precessing jet, with an approaching jet with large excursions in its po-

sition angle, gives rise to appreciable Doppler boosting effects (and therefore to changes of flux density that can be detected by timing analysis) is supported by the morphology of images reported by Massi et al. (2004), Dhawan et al. (2006), and Massi et al. (2012) that showed extended radio structures changing from two-sided to one-sided morphologies at different position angles. A physical model for LS I +61°303 of synchrotron emission from a precessing (P_2) jet, periodically (P_1) refilled with relativistic particles, has shown that the maximum of the long-term modulation occurs when P_1 and P_2 are synchronized, that is the jet electron density is at about its maximum and the approaching jet forms the smallest possible angle with the line of sight. This coincidence of the highest number of emitting particles and the strongest Doppler boosting of their emission occurs with the frequency of $\nu_1 - \nu_2$ and creates the long-term modulation observed in LS I +61°303 (Massi & Torricelli-Ciamponi 2014).

3. The folded curves of γ -ray data show that the peak at apoastron seems to be affected by the same orbital shift that affects the radio outburst. When the radio outburst occurs at orbital phase $\Phi \sim 0.65$, the first main GeV peak at periastron shows a bump at orbital phase $\Phi \sim 0.65$. When the radio outburst is shifted towards orbital phase $\Phi \approx 0.9$, the apoastron peak appears at the same orbital phases and is detached from the first main GeV peak.

We conclude that there exists a GeV peak at apoastron with the same timing characteristics and orbital shift as the radio emission. Because of the orbital shift, at some Θ -intervals this GeV peak is detached enough from the periastron γ -ray peak to become discernable as a second peak, and then it influences the timing analysis. Future analyses should investigate how the radio outburst and second GeV peak are connected; constraints to these future analyses should result from a detailed investigation of the evolution of the spectrum with orbital phase to see the increase of some spectral features at various orbital phases.

Acknowledgements

We thank Bindu Rani for reading the manuscript and useful comments, Robin Corbet for answering questions concerning the reduction of *Fermi*-LAT data and Chris Torrence for answering questions concerning the wavelet analysis. We thank Walter Alef and Alessandra Bertarini for their support with the computing power. Finally, we thank the anonymous referee for the careful reading of our manuscript and the useful comments made for its improvement. The wavelet software was provided by C. Torrence and G. Compo, and is available at URL: <http://atoc.colorado.edu/research/wavelets/>. The Green Bank Interferometer was operated by the National Radio Astronomy Observatory for the U.S. Naval Observatory and the Naval Research laboratory during the timeperiod of these observations. This work has made use of public *Fermi* data obtained from the High Energy Astrophysics Science Archive Research Center (HEASARC), provided by NASA Goddard Space Flight Center.

Chapter 7

Understanding the periodicities in the radio and GeV emission from LS I +61°303

This chapter is based on Jaron, Torricelli-Ciamponi, & Massi, submitted to A&A.

Abstract

Accretion theory along the eccentric orbit of LS I +61°303 predicts two ejections: one major ejection at periastron and a second lower ejection towards apastron. Observations reveal that whereas gamma-ray (GeV) emission around periastron is periodic with a period P_1 equal to the orbital period, gamma-ray emission toward apastron is due to two periodicities: P_1 and P_2 , where P_2 is associated with the jet precession. The same two periodicities dominate the strong radio emission toward apastron. Why are the two ejections producing emission with different periodicities? Why is the periastron emission modulated by P_1 only? We develop a physical model in which relativistic electrons are ejected

twice along the orbit. The ejecta form a conical jet, precessing with P_2 . The jet radiates in the radio band due to synchrotron processes and in the GeV energy band due to the external inverse Compton and synchrotron self Compton effects. We compare the output fluxes of our physical model with two available large archives: OVRO radio and *Fermi*-LAT GeV observations overlapping for 5 years. The larger ejection around periastron passage suffers strong energetic losses due to inverse Compton scattering of stellar photons. The result is that the more massive jet at periastron is shorter ($9.6 \cdot 10^6 r_g$) and slower ($\beta = 0.01$) than that developed at apastron of length of $1.04 \cdot 10^8 r_g$ and $\beta = 0.42$. The Doppler factor being a function of the jet velocity, the emission around periastron is little influenced by the small Doppler boosting variations modulated with P_2 . At apastron the larger velocity creates larger Doppler boosting variations and P_2 appears in the timing analysis.

7.1 Introduction

In the binary system LS I +61°303 the compact object travels in an eccentric orbit (Casares et al. 2005, $e = 0.72 \pm 0.15$) around a fast rotating B0 star (see sketch in Fig. 7.1). The orbital period is $P_1 = 26.4960 \pm 0.0028$ days (Gregory 2002) and periastron passage is at orbital phase $\Phi = 0.23$ (Casares et al. 2005).

Radio images show an elongated structure with very rapid variations in position angle attributed to possible jet precession (Massi 2004). Radio astrometry indicates a periodicity, with a period P_2 in the range 27–28 d (Massi et al. 2012, see their Fig. 1 reproduced as Fig. 4.7 here). Precession is confirmed by timing analysis of radio data revealing, along with the feature at $P_1 = 26.496 \pm 0.013$ d, a second strong spectral feature at $P_2 = 26.935 \pm 0.013$ d, consistent with the result from the astrometry. Periodic radio outbursts, always occurring towards apastron passage, are modulated by a long-term period (Gregory 2002) which corresponds to the beat of $\nu_1 = \frac{1}{P_1}$ and $\nu_2 = \frac{1}{P_2}$, with $P_{\text{beat}} = \frac{1}{\nu_1 - \nu_2} = 1626 \pm 68$ d (Massi & Jaron 2013; Massi & Torricelli-Ciamponi 2014; Massi et al. 2015; Massi & Torricelli-Ciamponi 2016).

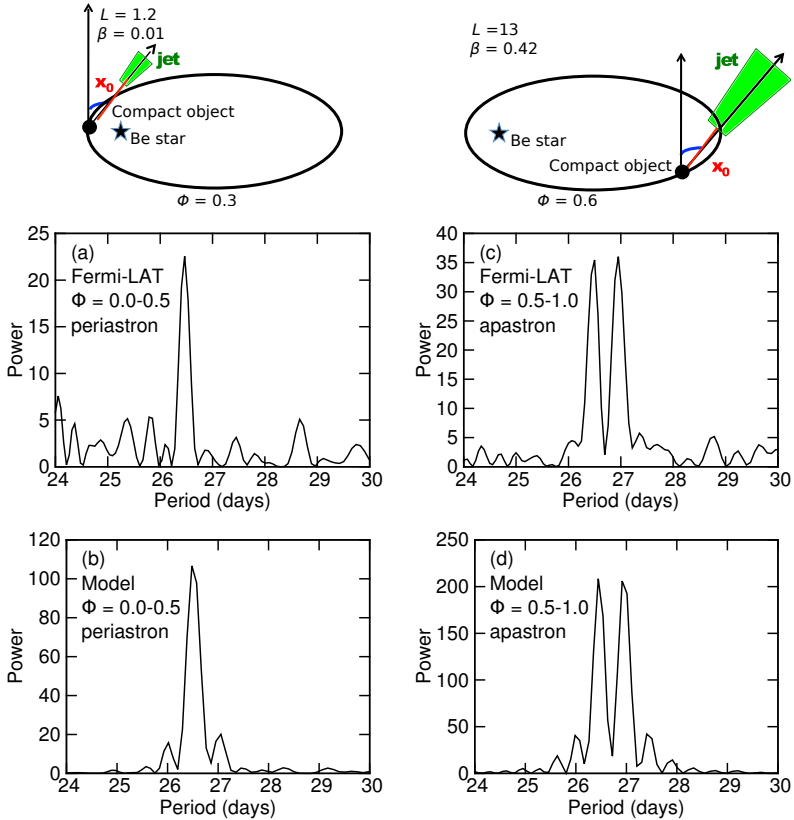


Figure 7.1: Top: Sketch of the stellar system LS I +61°303 with resulting model at periastron (left) and apastron (right). The compact object orbits the Be star in an eccentric orbit ($e = 0.72$, Casares et al. 2005). The model is the same as in Massi & Torricelli-Ciamponi (2014). We assume two ejections of relativistic electrons along the orbit, one at orbital phase $\Phi = 0.3$ (periastron) and the other at $\Phi = 0.6$ (towards apastron). The position of the base of the jet is at $x_0 = 0.36 \cdot 10^{13}$ cm, at both periastron and apastron. Length and velocity, however, are different: $L = 1.2$ and $\beta = 0.01$ at periastron, and $L = 13$ and $\beta = 0.42$ at apastron. **(a)** Lomb-Scargle periodogram for *Fermi*-LAT data from the orbital phase interval $\Phi = 0.0 - 0.5$ (periastron). The orbital period P_1 is clearly detected. **(b)** Lomb-Scargle periodogram of the model data from the orbital phase interval $\Phi = 0.0 - 0.5$ (periastron). The orbital period P_1 is the only peak, in agreement with the observations. **(c)** In the orbital phase interval $\Phi = 0.5 - 1.0$ (apastron) there is a peak at the precession period P_2 in addition to the orbital period P_1 . **(d)** The two peaks at P_1 and P_2 in the apastron data are reproduced by the model.

Gamma-ray emission in the GeV range (*Fermi*-LAT data) occurs both towards periastron and apastron but only the emission towards apastron is affected by the long-term modulation (Ackermann et al. 2013). Timing analysis of *Fermi*-LAT data confirms the results by Ackermann et al. (2013), finding both the two characteristic periods of the beat, P_1 and P_2 , at apastron but only P_1 in the emission around periastron (Jaron & Massi 2014).

As shown in Massi & Torricelli-Ciamponi (2014) the precession of the jet periodically changes the angle η between jet axis and the line of sight and therefore periodically changes the Doppler boosting $DB = f(\eta)$. That is, for an intrinsic flux S_i we can approximate the observed flux as $S_0(P_1, P_2) = S_i(P_1)DB(P_2)$. Each period, P_1 and P_2 , appears in the timing analysis only when the related term ($S_i(P_1)$ or $DB(P_2)$) is significant. Several authors have shown that in LS I +61°303 two ejections are expected along the eccentric orbit (Taylor et al. 1992; Marti & Paredes 1995; Bosch-Ramon et al. 2006; Romero et al. 2007) and this is consistent with finding P_1 in the signal both around periastron and apastron (Jaron & Massi 2014). The Bondi & Hoyle (1944) accretion rate $\dot{M} \propto \frac{\rho}{v^3}$ onto a compact object along the eccentric orbit of LS I +61°303 results in fact in two accretion peaks, one peak around periastron, where the density ρ has its maximum, and a second accretion peak towards apastron, where the lower relative velocity v between the accretor and the Be star wind compensates for the lower density (Taylor et al. 1992; Marti & Paredes 1995; Bosch-Ramon et al. 2006; Romero et al. 2007). The relativistic electrons ejected around periastron, embedded in the strong ultra violet photon field of the B0 star, suffer severe inverse Compton losses and are not able to emit synchrotron radiation detectable in the radio band; i.e., a large γ -ray outburst is predicted due to the IC upscattered UV photons and no or a reduced radio outburst (Bosch-Ramon et al. 2006). At the second ejection, because of the larger displacement from the B0 star the electrons suffer lower IC losses and produce the observed radio outburst and a γ -ray outburst (Bosch-Ramon et al. 2006).

Therefore, one expects radio emission at apastron and gamma-ray emission at both periastron and apastron as indeed is observed

(Fig. 7.6). However, why is the precession, P_2 , appearing only at apastron? The aim of this analysis is to investigate the physical origin for the finding that the γ -ray emission around apastron is affected by the precession period P_2 while that around periastron is not. In Sect. 7.2 we present a physical model for the emission from LS I +61°303. The calibration and reduction of the observational data are presented in Sect. 7.3. In Sect. 7.4 the computed emission from the model, for synchrotron and IC radiation is compared with observations made with the Owens Valley Radio Observatory (OVRO) and the *Fermi*-LAT. We present our conclusions in Sect. 7.5.

7.2 Methods

In the following we develop a physical model of a precessing (P_2) jet periodically (P_1) refilled with relativistic electrons in two different parts of the orbit (Sect 2.1). The synchrotron emission of such a jet is calculated as in Massi & Torricelli-Ciamponi (2014). In addition we calculate here inverse Compton (IC) radiation. Seed photons are stellar photons (External inverse Compton, EIC) (Sect 2.2) and the photons emitted by synchrotron radiation (synchrotron self Compton, SSC), i.e., jet photons (Sect. 2.3). The total IC emission from the model is calculated (Sect. 2.4). Electron energy losses are taken into account and the length of the jet is determined (in Sect. 2.5).

7.2.1 Relativistic electron distribution

For the eccentric orbit of LS I +61°303 accretion theory predicts two maxima (Taylor et al. 1992; Marti & Paredes 1995; Bosch-Ramon et al. 2006; Romero et al. 2007). One maximum is around periastron and the second is toward apastron. We will indicate the two relativistic electron distributions as N_I (periastron) and N_{II} (towards apastron).

Some quantities of this section are functions of the orbital phase

Φ , or of the long-term modulation Θ , defined as

$$\Phi = \frac{t - t_0}{P_1} - \text{int} \left(\frac{t - t_0}{P_1} \right), \quad (7.1)$$

$$\Theta = \frac{t - t_0}{P_{\text{beat}}} - \text{int} \left(\frac{t - t_0}{P_{\text{beat}}} \right), \quad (7.2)$$

where $t_0 = 43366.275$ MJD and $\text{int}(x)$ takes the integer part of x .

In Massi & Torricelli-Ciamponi (2014), the radio emission was reproduced with a relativistic electron distribution N ejected around apastron expressed in $\frac{\text{electrons}}{\text{cm}^3 \text{d}\gamma}$ as

$$\begin{aligned} N_{\text{II}} &= \kappa E^{-p} = \kappa_0(\Phi) l^{-a_3} E^{-p} \\ &= \frac{\kappa_0(\Phi)}{(mc^2)^{-p}} l^{-a_3} \gamma^{-p} = K_{\text{II}}(\Phi) l^{-a_3} \gamma^{-p}, \end{aligned} \quad (7.3)$$

with $a_3 = 2(2 + p)/3$ as in Kaiser (2006).

In the present work we add to the above electron distribution another component with a maximum around periastron

$$N_{\text{I}} = K_{\text{I}}(\Phi) l^{-a_3} \gamma^{-p}, \quad (7.4)$$

where p is the same as in (7.3), i.e., the same quantity used for the radio wavelength component. This new electron component is injected and expands in the same jet-like magnetic structure defined by the model of Massi & Torricelli-Ciamponi (2014).

We assume that the accelerated electrons powered by accretion are injected both at periastron and apastron in a similar way and that the initial (i.e., at time $t = t_{\text{min}}$ in $l = 1$) electron energy range is the same for the two distributions,

$$\gamma_1 \leq \gamma(t_{\text{min}}) \leq \gamma_2. \quad (7.5)$$

However, as we will see in Sect. 2.5, the value of γ evolves in a different way at periastron than at apastron owing to the different weight of radiative losses.

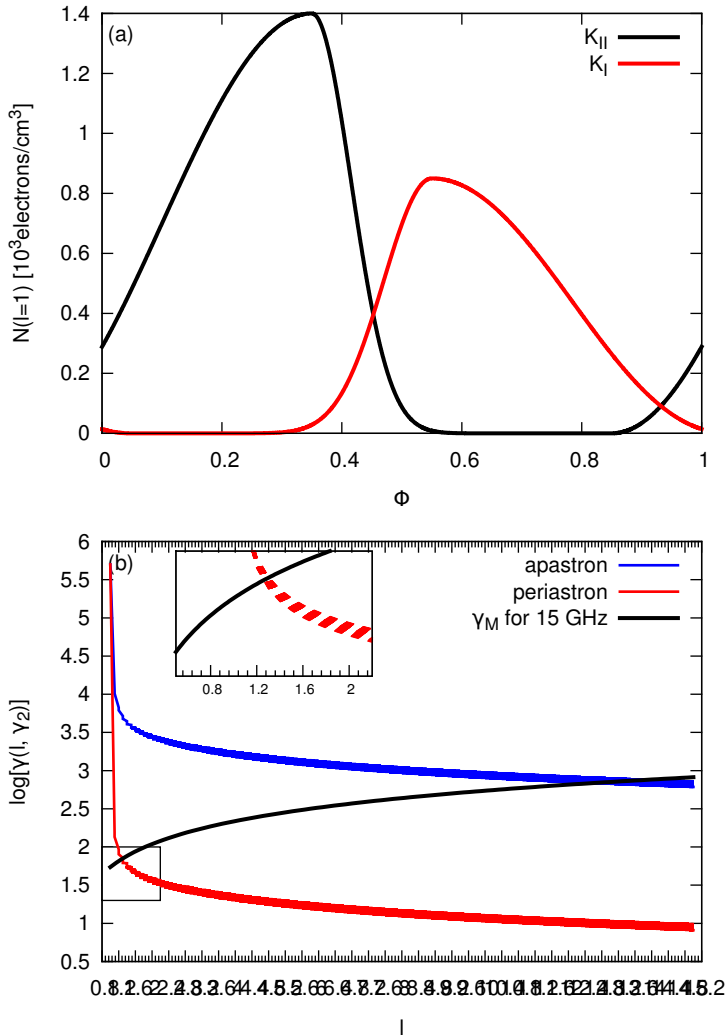


Figure 7.2: (a) Orbital modulation of the electron density assumed in the model. The two ejections are given one at $\Phi = 0.3$ (periastron) and the other at $\Phi = 0.6$. (b) Lorentz factor γ of the electrons as a function of the position l along the jet, for periastron and apastron separately. The black curve is a plot of the minimum γ (Eq. 7.23) necessary for the production of radio emission at 15 GHz for a magnetic field of $B = 2.8$ Gauss. The intersection point of the black curve with the red and blue lines defines the length of the jet at periastron and that of the jet towards apastron, respectively.

7.2.2 Stellar seed photons

In order to take into account IC scattering of B0 star photons by relativistic electrons in the jet, it is necessary to compute the distance between the central B0 star and the generic distance, $x_0 l$, along the jet anchored to the orbiting compact object. With ψ being the opening angle of the precession cone, under the assumption that the jet precession axis is perpendicular to the orbital plane, we can compute

$$d_{\perp} = x_0 l \cos \psi, \quad (7.6)$$

$$d_{\text{plane}} = \sqrt{r(\Phi)^2 + (x_0 l \sin \psi)^2 - 2r(x_0 l \sin \psi) \cos \Omega}, \quad (7.7)$$

$$d_{\text{jet-star}}(l, \Phi, \Theta) = \sqrt{d_{\text{plane}}^2 + d_{\perp}^2}, \quad (7.8)$$

where Ω (as in [Massi & Torricelli-Ciamponi 2014](#)) introduces the long-term modulation phase dependence and $r(\Phi)$ is the distance from the Be star to the point of the orbit corresponding to phase Φ . A sketch of the geometry is shown in [Fig. 7.1](#).

Assuming for the star a blackbody emission with temperature T_* , the photon density at the position $x_0 l$, along the jet is

$$\rho_{\text{star}}(l, \Phi) = \frac{4\pi B_{\nu}(T_*)}{ch^2\nu} \frac{\pi R_*^2}{4\pi d_{\text{jet-star}}^2} [\text{photons cm}^{-3} \text{erg}^{-1}]. \quad (7.9)$$

It is evident that this density value can be affected by the different position along the orbit of the compact object (and hence of its associated jet) only if the values of $r(\Phi)$ and x_0 are comparable. Given that the ellipse's semi-major axis is $a \simeq 8.4R_*$ ([Casares et al. 2005](#)), the orbital periodicity in the IC reprocessing of stellar photons will show up only if relativistic electrons are present at distances from the orbital plane $\simeq a$, which in our case implies distances $\simeq 4 \cdot 10^{12}$ cm. This fact implies that the jet scale dimensions, x_0 , must be of this order of magnitude or even smaller.

7.2.3 Jet seed photons

The jet photon density, due to synchrotron emission inside the jet, can be computed as a function of the distance l along the jet axis,

$$\rho_{\text{jet}}(l) = \frac{4\pi I_\nu(l)}{ch^2\nu} [\text{photons cm}^{-3} \text{ erg}^{-1}]. \quad (7.10)$$

In this expression I_ν is the locally produced synchrotron emission in the optically thin limit

$$I_\nu(l) = \int J_\nu x_0 dl, \quad (7.11)$$

and the notation is the same as in Massi & Torricelli-Ciamponi (2014).

7.2.4 IC emission

In order to compare our theoretical model for GeV emission to available data we derive the quantity

$$F_{0.1-3 \text{ GeV}} = \frac{1}{4\pi D^2} \int_{0.1 \text{ GeV}}^{3 \text{ GeV}} \frac{E_{\text{IC}}}{\epsilon} d\epsilon \left[\frac{\text{counts}}{\text{cm}^2 \text{sec}} \right], \quad (7.12)$$

where $\epsilon = h\nu$ is the photon energy, and E_{IC} is the total scattered power per energy (in units of $\text{erg sec}^{-1} \text{ erg}^{-1}$), which can be computed following Rybicki & Lightman (1986):

$$E_{\text{IC}} = \sum_i \int_V \frac{A D_i}{l^{a_3}} \int \frac{\epsilon}{\epsilon_S} \rho_i(\epsilon_S) \int_{\gamma_m}^{\gamma_M} \gamma^{-p-2} f\left(\frac{\epsilon}{4\gamma^2 \epsilon_S}\right) d\gamma d\epsilon_S dV, \quad (7.13)$$

where the overall emission is composed of the sum of two different contributions: SSC from jet photons ($i = 1$, $\rho_1(\epsilon_S) = \rho_{\text{jet}}$) and EIC from star photons ($i = 2$, $\rho_2(\epsilon_S) = \rho_{\text{star}}$). In the above expression $\epsilon_S = h\nu_S$ is the seed photon energy, V is the volume over which to integrate the IC emission, i.e., the jet and other quantities are defined as follows:

$$f\left(\frac{\epsilon}{4\gamma^2 \epsilon_S}\right) = \frac{2}{3} \left(1 - \frac{\epsilon}{4\gamma^2 \epsilon_S}\right) \quad \text{for} \quad 0 \leq \frac{\epsilon}{4\gamma^2 \epsilon_S} \leq 1, \quad (7.14)$$

and zero otherwise,

$$D_i = K_{\text{I}} \times DB_i(\beta_{\text{I}}) + K_{\text{II}} \times DB_i(\beta_{\text{II}}) \quad (7.15)$$

$$A = \frac{3}{4} c \sigma_{\text{T}}, \quad (7.16)$$

with the Thompson cross-section σ_{T} . The Doppler boosting term is

$$DB_i = \left[\frac{1}{\Gamma(1 \pm \beta \cos \eta)} \right]^{ex_i}, \quad (7.17)$$

$$\Gamma = \frac{1}{\sqrt{1 - \beta^2}},$$

with $\beta = v/c$, v the electron velocity component along the jet axis and the possibility for a different injection velocity for each distribution is allowed, i.e., $\beta = \beta_{\text{I}}$ for periastron distribution and $\beta = \beta_{\text{II}}$ for apastron distribution. η is the angle between observer's line of sight and the jet axis (see Massi & Torricelli-Ciamponi 2014 for details). The Doppler boosting exponent ex_i for IC radiation produced by stellar seed photons is different from that for synchrotron jet photons, in particular we have $ex_1 = 4$ (see, e.g., Potter & Cotter 2012) and $ex_2 = 2 + p$ (Kaufman Bernadó et al. 2002).

The integral over the seed spectrum, i.e., on ϵ_{S} , is extended to all seed photons which can contribute to GeV emission. Since the function $f\left(\frac{\epsilon}{4\gamma^2\epsilon_{\text{S}}}\right)$ is different from zero only in the interval $[0, 1]$, this condition shows that, given an electron distribution in a specific γ range, and a seed photon of energy ϵ_{S} , IC emission is different from zero only for energies, ϵ , such that $0 \leq \epsilon \leq 4\gamma^2\epsilon_{\text{S}}$.

The integration interval in dy depends on the distance l along the jet axis since electrons lose energy while proceeding along the jet. Therefore, the integration range is $\gamma_{\text{M}}(l = 1) = \gamma_2$ and $\gamma_{\text{m}}(l = 1) = \gamma_1$ at the jet beginning, while for a generic distance we have

$$\gamma_{\text{M}}(l) = \gamma(l, \gamma_2) \quad \gamma_{\text{m}}(l) = \gamma(l, \gamma_1)$$

where these function are specified by Eq. (7.18) in the next section.

7.2.5 Accelerated electron survival

As outlined in various parts of this section, relativistic electrons will lose energy with time, i.e., on their way along the jet, owing to different types of losses and hence their γ values decrease. From expression (26) in Kaiser (2006) we can investigate how γ evolves along the jet when affected by adiabatic, synchrotron and IC losses.

We examine electrons starting at time $t_{\min} = x_0/(\Gamma\beta c)$ at the jet basis, x_0 , (all notations are as in Kaiser 2006) and arriving at time $t = x_0 l/(\Gamma\beta c)$ at the distance lx_0 along the jet axis. For the case of our model we have $a_1 = 1$, $a_2 = 2$, and with $W = 4\sigma_T/(3m_e c) = 3.2 \cdot 10^{-8}$, it is possible to compute the value $\gamma(l)$ at a certain distance along the jet axis when the initial value in $l = 1$ was $\gamma(t_{\min})$.

Using Kaiser (2006)'s expression in a more general way, which includes internal and external IC losses, SSC and EIC respectively, we obtain for a generic initial value of $\gamma(t_{\min}) = g$

$$\gamma(l, g) = \frac{g l^{-2/3}}{1 + W \frac{x_0}{\Gamma\beta c} g \left\{ \int_1^l l^{-2/3} [U_B + U_{\text{jet}} + U_{\text{star}}] dl \right\}}. \quad (7.18)$$

In the above expression the energy densities are due to different types of losses. The term

$$U_B(l) = \frac{B_0^2}{8\pi} l^{-4} [\text{erg cm}^{-3}] \quad (7.19)$$

takes into account synchrotron losses, while the two terms

$$U_{\text{jet}}(l, \Phi) = \frac{4\pi}{c} \int I_\nu d\nu [\text{erg cm}^{-3}], \quad (7.20)$$

$$U_{\text{star}}(l, \Phi, \Theta) = \int \frac{B_\nu(T_*)}{c} \frac{\pi R_*^2}{d_{[\text{jet-star}]}}^2 d\nu [\text{erg cm}^{-3}] \quad (7.21)$$

take into account electron losses due to interactions with synchrotron jet photons and star photons, SSC and EIC respectively.

Following Eq. (7.18) each initial value of the Lorentz factor, g , decreases along the jet, causing the initial distribution to shift to lower

energies. In particular, choosing $\gamma(t_{\min}) = g = \gamma_2$, we can determine how the upper limit of the distribution evolves along the jet, i.e., $\gamma_M(l) = \gamma(l, \gamma_2)$. Its profile is shown in Fig. 7.2 b, for two specific orbital positions, i.e., around periastron ($\Phi = 0.2$) and around apoastron ($\Phi = 0.65$).

Synchrotron emission is centered on a peak spectral frequency (Ginzburg & Syrovatskii 1965)

$$\nu = 1.8 \cdot 10^6 \gamma^2 B. \quad (7.22)$$

Hence, for $B = B_0 l^{-2}$ and with a magnetic field value at the jet basis of $B_0 = 2.8$ G, as results from our present model, the jet emitted radio frequency can be present at $\nu = 15$ GHz (OVRO observations) only if the electron distribution extends up to

$$\gamma_M(l) > \left[\frac{\nu l^2}{1.8 \cdot 10^6 B_0} \right]^{1/2} \approx 57 l, \quad (7.23)$$

Condition (7.23) is drawn as a black line in Fig. 7.2; its intersection with the red line describing the γ decrease induced by losses at periastron defines the jet length ($L \sim 1.2$). At apastron it is evident that the jet length ($L \sim 13$), and hence the radio emission, is not limited by radiative losses.

7.3 Observations and data reduction

We compare the model output data to observational data at radio and GeV wavelengths. The databases that we use for that purpose are the OVRO monitoring at 15 GHz ranging from MJD 54684 until MJD 56794 (08/06/2008 until 05/17/2014), and GeV γ -ray data from the *Fermi*-LAT in the energy range 0.1–3.0 GeV from MJD 54682 until MJD 57450 (08/04/2008 until 03/03/2016).

The calibration of radio OVRO data is described in Massi et al. (2015).

For the analysis of *Fermi*-LAT data we used version v10r0p5

of the Fermi ScienceTools¹. We used the instrument response function P8R2_SOURCE_V6 and the corresponding model gll_iem_v06.fits for the Galactic diffuse emission and the template iso_P8R2_SOURCE_V6_v06.txt. Model files were created automatically with the script make3FGLxml.py² from the third *Fermi*-LAT source catalog (Acero et al. 2015). The spectral shape of LS I +61°303 in the GeV regime is a power law with an exponential cut-off at 4–6 GeV (Abdo et al. 2009a; Hadasch et al. 2012). Here we restrict our analysis to the power law part of the GeV emission by fitting the source with

$$\frac{dn}{dE} = n_0 \left(\frac{E}{E_0} \right)^{-\alpha + \beta \log(E/E_b)} \left[\frac{\text{counts}}{\text{cm}^2 \text{sec dE}} \right] \quad (7.24)$$

with all parameters left free for the fit, and including data in the energy range $E = 0.1 - 3$ GeV. All other sources within a radius of 10° and the Galactic diffuse emission were left free for the fit. All sources between $10 - 15^\circ$ were fixed to their catalog values. The light curves were computed by performing this fit for every time bin of width one day for *Fermi*-LAT data from 2008 August 8 (MJD 54684) till 2016 March 3 (MJD 57450). The average test statistic for LS I +61°303 was 40, which corresponds to a detection of the source at the 6.3σ level on average in each time bin.

The search for periodicities in the light curves is carried out with the UK Starlink package, implementing the Lomb-Scargle algorithm (Lomb 1976; Scargle 1982). The procedure is the same as outlined in Massi & Jaron (2013).

7.3.1 Consistency with previous results

Jaron & Massi (2014) found that the GeV data from LS I +61°303 observed by the *Fermi*-LAT are modulated by P_1 and P_2 in the orbital phase interval $\Phi = 0.5 - 1.0$ (apastron), but by only P_1 in $\Phi = 0.0 - 0.5$ (periastron) (see their Fig. 3). Their analysis was performed with

¹available from <http://fermi.gsfc.nasa.gov/ssc/data/analysis/software/>

²available from <http://fermi.gsfc.nasa.gov/ssc/data/analysis/user/>

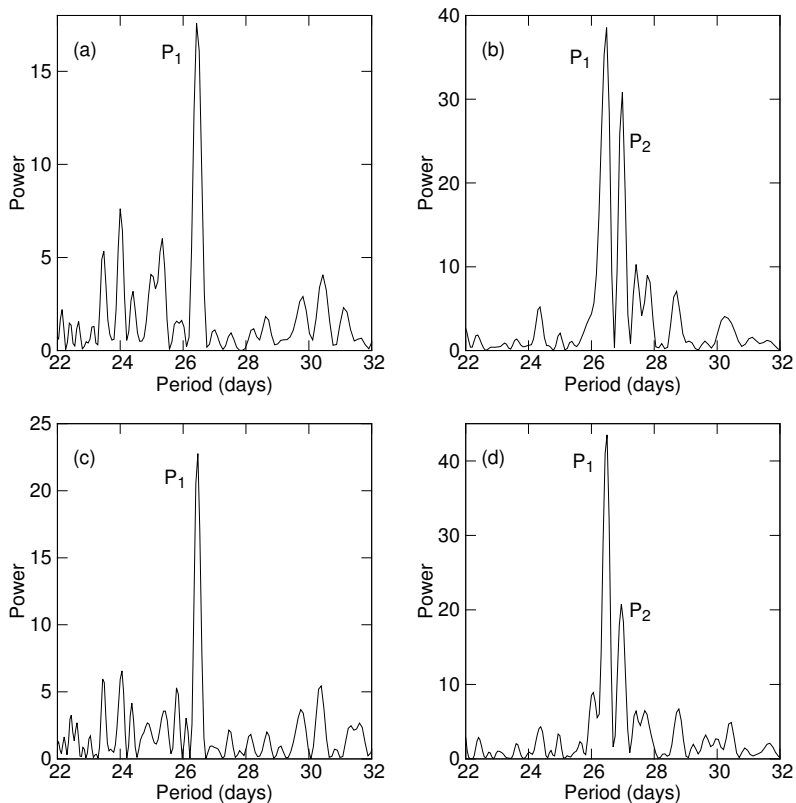


Figure 7.3: Timing analysis of Pass 8 *Fermi*-LAT data, energy range 0.1–3.0 GeV. **(a, b)** Time interval MJD 54683–56838 (same epoch as used in Jaron & Massi 2014, representing Pass 7 data for the energy range 0.1–300 GeV). The result of the timing analysis is confirmed (compare Fig. 3 in Jaron & Massi 2014): **(a)** periastron, only P_1 , **(b)** apastron, P_1 and P_2 . **(c, d)** Time interval 54683–57450: **(c)** periastron, only P_1 , **(d)** apastron, P_1 and P_2 , but with less power than in (b).

the Pass 7 *Fermi*-LAT data, using the energy range 0.1 – 300 GeV, and for the time interval MJD 54683–56838. In the work presented here we use Pass 8 *Fermi*-LAT data and restrict the energy range to 0.1 – 3.0 GeV. It is therefore important to verify how the data processed with the new method compare to the previous data. We apply the timing analysis to the data processed with the new method as in Jaron & Massi (2014). The result is shown in the top panel of Fig. 7.3. Since we use a time bin of 1 day for the likelihood analysis, Figs 3 e and h in Jaron & Massi (2014) are the figures to use for comparison. Clearly the result of Jaron & Massi (2014) is confirmed here, i.e., in Fig. 7.3 a the only significant feature is a peak at the orbital period P_1 , whereas in Fig. 7.3 b there is not only a peak at P_1 but also a highly significant one at P_2 . This result shows that the timing characteristics reported by Jaron & Massi (2014) is a feature of the power law part of the SED ranging from 0.1–3 GeV and not a contribution of a higher energy range.

7.3.2 Influence of the Θ interval on P_2

Applying the same timing analysis to all available *Fermi*-LAT data ranging from MJD 54682 until MJD 57450 ($\Theta = 6.8 - 8.8$) we obtain the result presented in the bottom panel of Fig. 7.3. While in Fig. 7.3 c, showing the Lomb-Scargle periodogram for the periastron data, the orbital period P_1 has increased its power and stands out a bit more significantly over the noise when compared to Fig. 7.3 a, the P_2 feature in Fig. 7.3 d has decreased its power and its relative importance with respect to P_1 drops to about 1/2, when it was 3/4 for the narrower time range shown in Fig. 7.3 b.

Which are the data causing this decline in the power of P_2 ? In order to find out we remove a certain interval of the long-term modulation from the data in the sense that we delete data for which $\Theta = 0.0 - 0.1, 0.1 - 0.2, \dots, 0.9 - 1.0$ and perform Lomb-Scargle timing analysis on the remaining data. In Fig. 7.4 the resulting powers of P_1 and P_2 are plotted for the different Θ -intervals removed from the data. While the power of P_1 is only slightly affected by the choice of the removed Θ -interval and in a random manner, the power of P_2

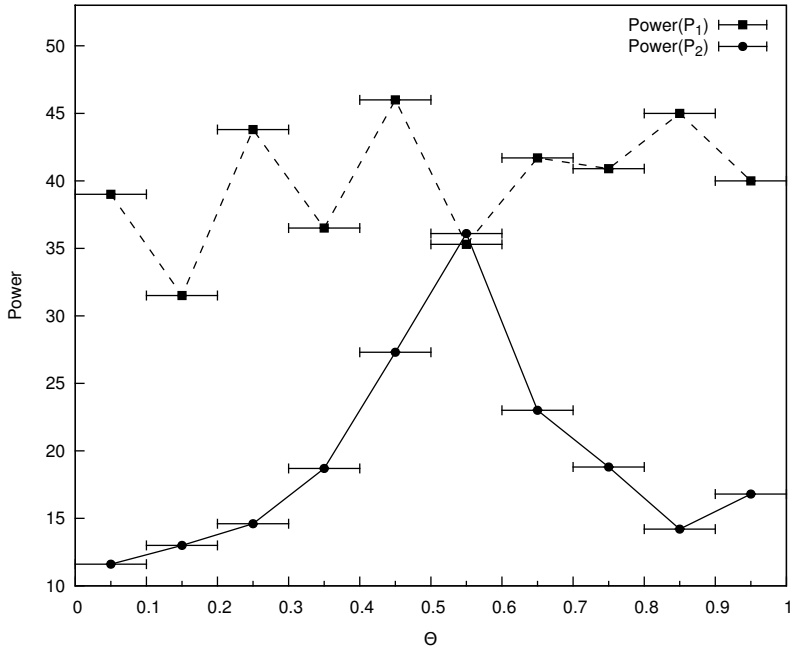


Figure 7.4: Test on the Θ -interval which corrupts the timing analysis. In this plot the powers of P_1 and P_2 resulting from Lomb-Scargle timing analysis are plotted as a function of the Θ -interval removed from the data, that interval being indicated by the horizontal error bars. While the power of P_1 is only affected very little and in a random way, the power of P_2 shows a systematic trend peaking at $\Theta = 0.5 - 0.6$.

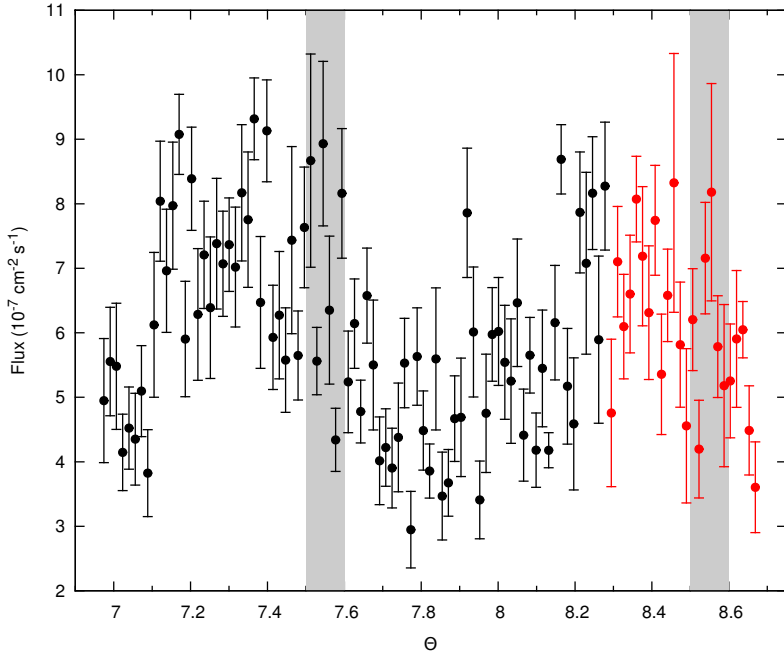


Figure 7.5: All *Fermi*-LAT data from the orbital phase interval $\Phi = 0.5 - 1.0$, i.e., apastron. Data until MJD 56838 (the time interval in Jaron & Massi 2014) are plotted in black, data newer than that appear in red. The long-term amplitude modulation is clearly visible. The two grey areas indicate the θ -intervals which are removed from the data for the present analysis.

is clearly dependent on the removed Θ -interval in a stronger and systematic way. We find that P_2 gains the strongest power by removing the interval $\Theta = 0.5 - 0.6$. This is indicated by the grey areas in Fig. 7.5, where we plot all *Fermi*-LAT data from the orbital phase interval $\Phi = 0.5 - 1.0$ (i.e., apastron) and averaged over one orbit. The resulting periodogram, plotted in Fig. 7.1 c shows two peaks at P_1 and P_2 with equal power.

7.4 Results

The model parameters are shown in Table 7.1. Figure 7.2 shows the shape of the two electron distributions injected around periastron ($\Phi \approx 0.30$) and towards apastron ($\Phi \approx 0.6$). The relativistic electron density K_I is larger than K_{II} as for the accretion peaks of Figs 5 and 6 in Marti & Paredes (1995).

Figure 7.1 shows the timing analysis results. The observed γ -ray flux is modulated by only the orbital period P_1 at periastron, as shown in Fig 7.1 a. Also the model data are only modulated by the same period P_1 , as shown in Fig 7.1 b. At apastron, both observational and model data are not only modulated by P_1 but also by P_2 .

The folded light curves for radio (OVRO) and γ -ray data (*Fermi*-LAT) are shown in Fig. 7.6. The right panel of Figure 7.6 shows the radio data and model. One sees that at periastron, even if N_I is larger than N_{II} (Fig. 7.2), there no radio peak. Concerning *Fermi*-LAT data, the two peak structure is present in both observations and model. The two peak structure is above an offset of $5 \cdot 10^{-7} \text{ cm}^{-2} \text{ s}^{-1}$. The origin of the offset could be SSC of optical photons produced not in the jet but in the hot flow that fills the inner part of the accretion flow. Such an SSC component is invoked to explain the MeV tail in the hard state of Cygnus X-1 (Poutanen & Veledina 2014) but extended to GeV, as the LS I +61 $^\circ$ 303 spectrum from 0.01–1000 MeV in Fig. 5 by Tavani et al. (1996) suggests.

We find the jet at periastron and apastron to have a quite different velocity parameter, $\beta = 0.01$ at periastron while $\beta = 0.42$ at apastron. Moreover, the jet has quite a different length at periastron compared

Parameter	Value
Periastron:	
β	$\lesssim 0.01$
a	1400 ± 50
Φ_0	0.35 ± 0.01
rn	0.5 ± 0.1
ex	6 ± 2
s_{jet}	$\lesssim 1.2$
Apastron:	
β	0.42 ± 0.01
a	850 ± 50
Φ_0	0.55 ± 0.01
rn	8.0 ± 0.5
ex	1.10 ± 0.05
s_{jet}	13 ± 1
General:	
Δ	-925.05 d
ζ	45.61°
ψ	40.37°
γ_2	$5 \cdot 10^5$
P_1	26.4960 d
P_2	26.922 d
e	0.72
T_*	28000 K
q	2.4
q_τ	2.3 ± 0.1
flux ₀	$0.40 \pm 0.02 \cdot 10^{-24}$
p	1.8
Offset	$5.0 \pm 0.5 \cdot 10^{-7} \text{cm}^{-2} \text{s}^{-1}$

Table 7.1: Parameters used for the model. See text for a description of the parameters. Error bars were determined by varying the parameters and still obtaining similar results. Parameters without error bars were kept fixed.

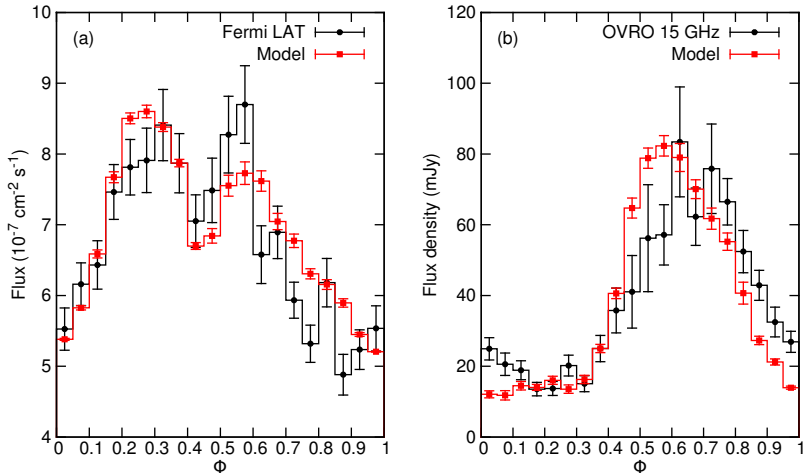


Figure 7.6: Results of the model in comparison with the observations. **(a)** Comparison of the model GeV output (red) with the observations by the *Fermi*-LAT (black), the energy range is 0.1–3.0 GeV in both cases and the time interval is MJD 54682–56450. The observed *Fermi*-LAT light curve, here folded on the orbital period $P_1 = 26.4960$ days, shows a periastron peak at $\Phi \approx 0.3$ and a second peak towards apastron at $\Phi \approx 0.55$. Assuming two electron injections along the orbit the shape of the orbital modulation of this observed GeV lightcurve is reproduced. **(b)** Comparison of the model radio output (red) with the observations by OVRO (black), both at 15 GHz spanning the time interval MJD 54909–56794. The observed light curve, folded on the orbital period P_1 , shows only one peak along the orbit, which is at apastron, peaking at $\Phi \approx 0.7$. The model reproduces this characteristic apastron peak even though two electron injections are taken into account. The reason for the absence of the periastron radio peak is the short length of the jet at periastron.

to apastron: $L \sim 1.2$ at periastron while it can be up to $L \sim 13$ for the apastron jet, $x_0 = 3.6 \cdot 10^{12}$ cm. The lengths are derived by the analysis of the energetic losses of the electrons following Section 7.2.5. Fig. 7.2 reports how the maximum $\gamma_M(l)$ value evolves along the jet axis (Eq. 7.23) at periastron (red line) and apastron (blue line). It is evident that electrons at periastron suffer stronger losses, essentially owing to IC losses. As explained in Sect. 7.2.5, there is a position along the jet axis where the electron Lorentz factor attains a too low value to be able to produce the observed radio emission at 15 GHz. This length is given by the intersection of $\gamma_M(l)$ curves with the black curve defined by Eq. (7.23).

7.5 Conclusions

We have modelled the synchrotron and inverse Compton emission of a precessing jet (with period P_2) periodically (with period P_1) refilled, twice along the orbit, with relativistic electrons. The model is able to reproduce both radio and gamma-ray (GeV) emission (see Figs 7.1 and 7.6).

Due to the strong IC losses at periastron the electrons lose their energy already at $L = 1.2$ becoming unable to produce radio emission after that length. For this reason we do not observe strong radio emission at periastron even if a large accelerated electron input is present. The length $L = 1.2$ corresponds to $x = Lx_0 = 9.6 \cdot 10^6 r_g$ (for $M_{\text{BH}} = 3M_{\odot}$), $L = 13$ corresponds to $Lx_0 = 1.04 \cdot 10^8 r_g$, and therefore one order of magnitude farther embedded in the acceleration zone (see, e.g., Piner et al. 2003).

The shorter periastron jet is also more massive (see Fig. 7.2) because of the higher accretion rate at periastron. The larger inertia because of the higher accretion rate and the fact that the jet is truncated while still embedded in the accelerating region are both consistent with the lower β that we find for the periastron jet: $\beta = 0.01$ at periastron and $\beta = 0.42$ at apastron.

The low velocity at periastron gives rise to a small Doppler boosting and consequently to a low dependency of the observed flux on P_2 .

As a result, the γ -ray flux at periastron is neither modulated by the long-term periodicity (Ackermann et al. 2013) due to the beating of P_1 and P_2 (Jaron & Massi 2014) nor does P_2 appear in the timing analysis. At apastron the larger velocity creates larger DB variations and both P_2 appears in the timing analysis and radio and gamma-ray emission show the long-term periodicity (Massi & Jaron 2013; Jaron & Massi 2014).

Acknowledgements

We thank Eduardo Ros and Karl Menten for reading the manuscript. We thank Bindu Rani and Robin Corbet for useful discussions about likelihood analysis of *Fermi*-LAT data. We thank Alan Marscher for useful discussions about jet acceleration. Helge Rottmann provided us with computing power. This work has made use of public *Fermi* data obtained from the High Energy Astrophysics Science Archive Research Center (HEASARC), provided by NASA Goddard Space Flight Center. The OVRO 40 m Telescope Monitoring Program is supported by NASA under awards NNX08AW31G and NNX11A043G, and by the NSF under awards AST-0808050 and AST-1109911.

Chapter 8

Observation of QPO from LS I +61°303 at radio wavelengths

This chapter will be the basis for a paper to be submitted to A&A.

8.1 Introduction

In the previous part of this thesis we have analyzed periodicities of LS I +61°303 that are in a range of one month (orbital period P_1 and precession period P_2) giving rise to a long-term modulation of years (P_{long} as result of the beating between P_1 and P_2). In addition to these periodicities, there is evidence that the source features also shorter variability on time scales of the order of a few days and shorter, down to hours.

Zimmermann et al. (2015) observed LS I +61°303 at seven radio frequencies between 2.6 GHz and 32 GHz with the 100-m telescope in Effelsberg. The light curves they obtained are sampled in a quasi-simultaneous way with a sampling rate of approximately every 12 hours over 14 consecutive days, covering the rise and the decline of one radio outburst. From their Fig. 1 (see here Fig. 8.1 top) it is well visible that the radio flux is significantly modulated on top of the actual radio

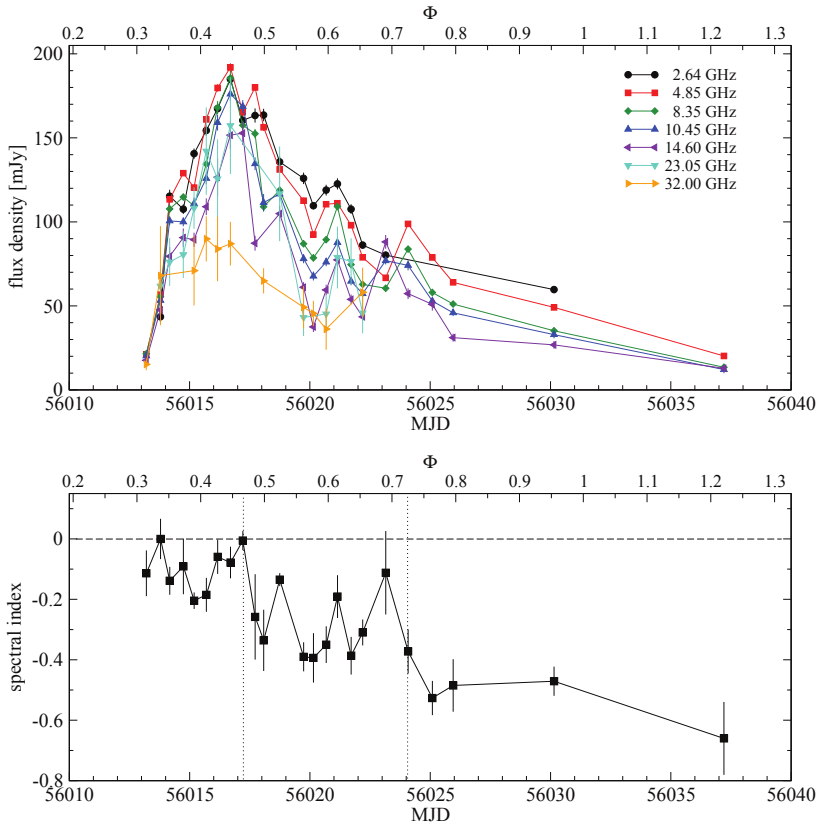


Figure 8.1: Radio light curves (top) and spectral index (bottom) at seven radio frequencies between 2.6 and 32 GHz, observed quasi-simultaneously with a sampling rate of about 12 hours with the 100-m telescope in Effelsberg, covering rise and decline of one radio outburst. Both fluxes and spectral index are significantly variable on top of the actual outburst. Fig. 1 in Zimmermann et al. (2015).

outburst, especially during the decline, i.e., after MJD 56017 for this one outburst. Also the spectral index shows significant variability on the same time scales (see here Fig. 8.1 bottom).

Peracaula et al. (1997) observed the source at radio wavelength 6 cm (i.e., 5 GHz) with the Very Large Array (VLA) and report on microflares with an amplitude of ~ 4 mJy (see their Fig. 2) and a possible periodicity of ~ 1.4 hours. In addition, they measure linear polarization of $\sim 2\%$ on all three non-consecutive observation days (see their Table 1).

Aiming at further investigation of these previously reported intraday variabilities and periodicities, we observed LS I +61°303 with the 100-m radio telescope in Effelsberg at three frequencies quasi-simultaneously and with unprecedented cadence. In this chapter we report on our results which will be the basis for a paper to be submitted (Jaron et al., in prep.).

8.2 Observation

8.2.1 Schedule

The periodicity of LS I +61°303 allows for precise scheduling of observations. We scheduled the observation at the Effelsberg 100-m telescope with the aim of observing the decay of a radio outburst, because there is evidence for short-term variability during these orbital phases (Zimmermann et al. 2015). Figure 8.2 shows the archived GBI 8 GHz data folded on $P_{\text{average}} = 26.714$ days, the period with which the radio outbursts actually occur (Ray et al. 1997; Massi & Jaron 2013; Jaron & Massi 2013; ?; Chapter 5 of this thesis), revealing that what we have observed is in fact the peak flux density.

8.2.2 Calibration

As primary flux calibrators we observed the quasars 3C 147, 3C 161, 3C 286, 3C48, and NGC 7027. Secondary calibrators were 0212+735 and 0835+580. The flux calibration was done as describes in Fuhrmann et al. (2014) and Angelakis et al. (2015).

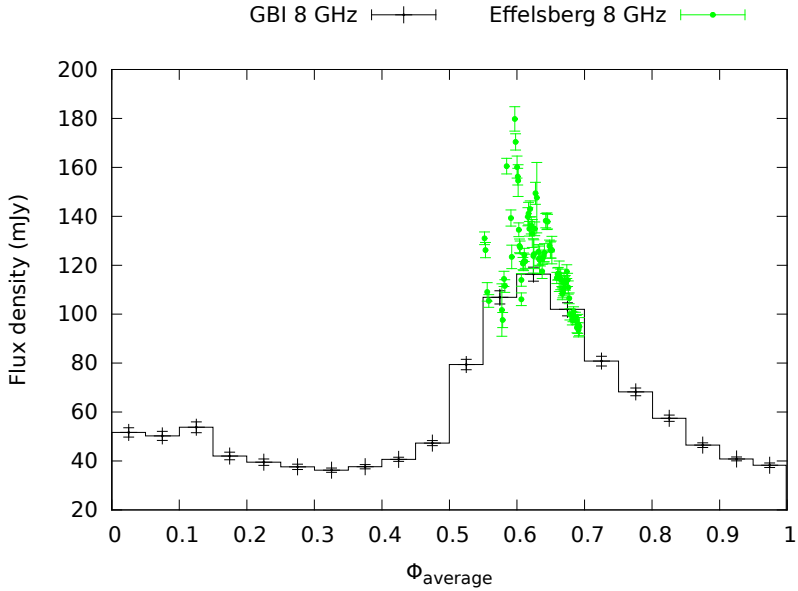


Figure 8.2: Comparison of archived GBI 8 GHz data and the 8 GHz data from this observation. The data have been folded on $P_{\text{average}} = 26.714$ days from the analysis of Massi & Torricelli-Ciamponi (2016). This figure shows that predicting the radio outbursts with the method by Jaron & Massi (2013) (Chapter 5 here) still works.

8.3 Results

8.3.1 Light curves

The calibrated light curves are shown in Fig. 8.3, where the 5 GHz data appear in red, 8 GHz in green, and 10 GHz in blue. In addition to the data from our observation, there is shown a data point from OVRO observation at 15 GHz in magenta. The observed radio fluxes are clearly variable with flux densities ranging from 60 – 180 mJy. There is a peak affecting all frequencies at MJD 56766.0 ($\Phi = 0.73$), featuring a flattening of the radio spectrum (explained in more detail below).

8.3.2 Evolution of the spectral index

In the bottom panel of Fig. 8.3 the spectral index is shown. The spectral index α was obtained by fitting a power law

$$S_\nu \propto \nu^\alpha \quad (8.1)$$

to all available data points within each time bin of 45 minutes, the horizontal error bars reflect these time bins. Concerning the long-term trend of the spectral index evolution we can distinguish two periods which are separated at MJD 56766.7 ($\Phi = 0.73$), indicated by the grey vertical line in Fig. 8.3 bottom. In the first period the spectral index oscillates and is reasonably well fitted by a sine wave of the form

$$f_1(t) = a_1 \sin\left(\frac{2\pi}{P}(t - t_0)\right) + b_1, \quad (8.2)$$

where the best fit parameters are $a_1 = 0.12 \pm 0.03$, $P = 1.77 \pm 0.20$ d, $t_0 = \text{MJD } 56765.5$ (fixed), and $b_1 = -0.27 \pm 0.02$. An oscillating evolution of the spectral index of LS I +61°303 during a certain interval was previously observed by Zimmermann et al. (2015), also with a period of about two days in the orbital phase interval $\Phi \approx 0.45 - 0.75$. While we cannot report on the beginning of this oscillating trend it also lasts until $\Phi \approx 0.75$ in our case, hinting at a periodic behavior of the source.

The second period, i.e., after MJD 56766.7, is characterized by a linear decline of the spectral index. We fitted a line

$$f_2(t) = \Delta\alpha \cdot t + b_2 \quad (8.3)$$

to the data and obtained $\Delta\alpha = -0.11 \pm 0.01 \text{ d}^{-1}$, and $b_2 = -0.32 \pm 0.02$.

8.3.3 Flattening of the radio spectrum

In the previous subsection it was shown that the spectral index of the observed light curves, being in the range $\alpha \approx -0.6 - 0$, is variable in a systematic way. In particular, during the oscillating part the spectral index reaches values around zero and above. In this paragraph we focus on these flat or even inverted parts of the light curves.

Figure 8.4 shows three plots, flux density vs. frequency, in double logarithmic scale, a and b containing only data from our observations, c in addition containing one data point from OVRO at 15 GHz. The data points are from a time interval of 45 minutes centered around the time indicated in the plots. The solid line is the result of fitting a power law to these data points.

8.3.4 Timing analysis

The long-term trend of the light curves at the three different frequencies is reasonably well fit by a parabola to first order. We fitted a quadratic function

$$f_3(t) = a_3t^2 + b_3t + c_3 \quad (8.4)$$

to each light curve. The best resulting fit parameters are listed in Table 8.1 and the result of the fit is shown in Fig. 8.5, where the fitted parabola is shown as a solid black line.

In order to further analyze the short-term variability we subtracted that parabola from each light curve, the result of which is shown in the second row of Fig. 8.5, where the time axis is now expressed in hours since MJD 56764.6. The Lomb-Scargle periodograms are shown in the third row of Fig. 8.5. The 5 GHz data show the most prominent peak

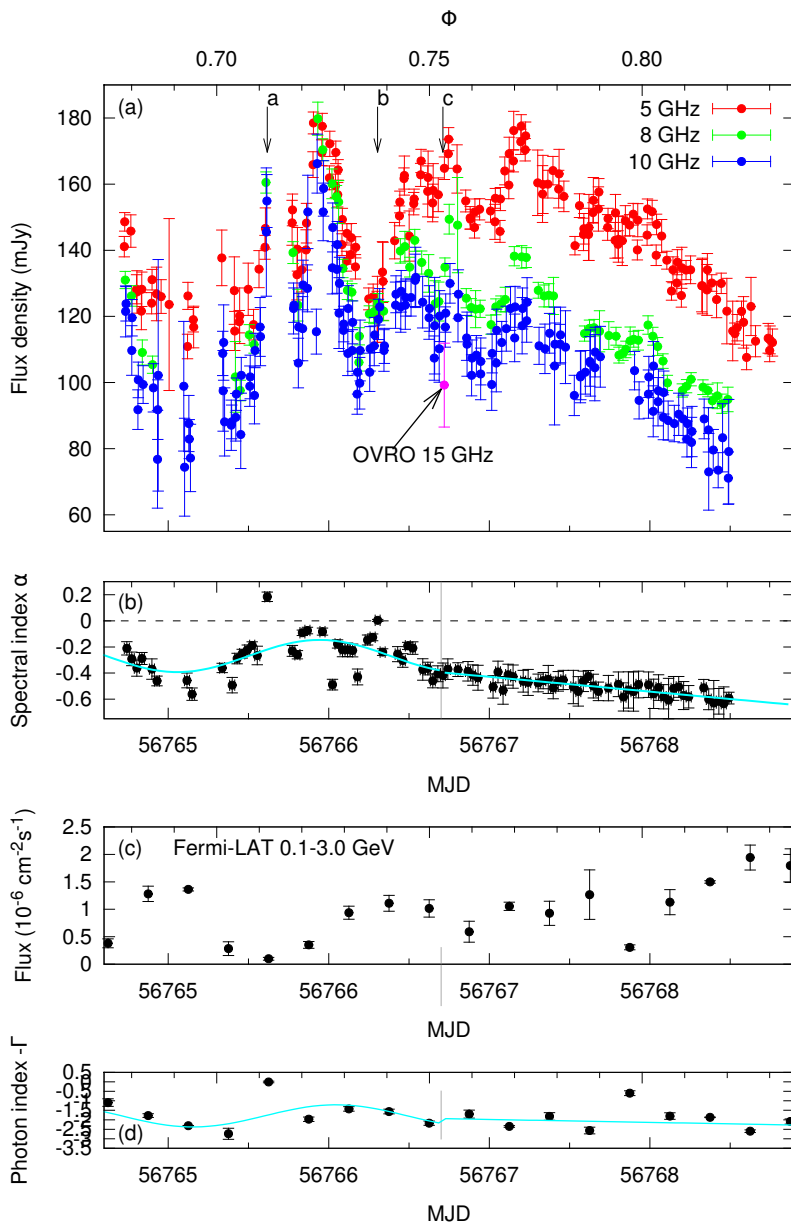


Figure 8.3: (a) Effelsberg light curves, the arrows mark the times of the spectral indices shown in Figs 8.4 a, b, and c, respectively, (b) Effelsberg spectral index. (c) *Fermi*-LAT light curve, (d) *Fermi*-LAT photon index.

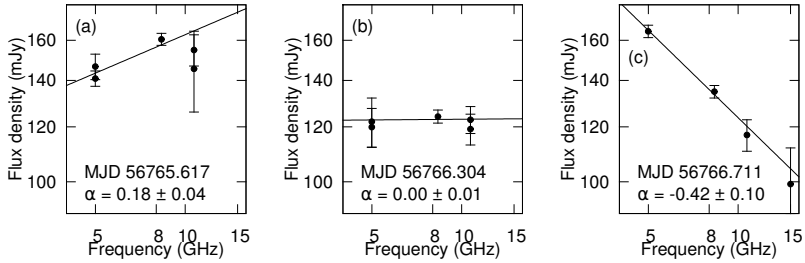


Figure 8.4: Flux density vs. frequency, both axes in logarithmic scale. Each figure contains all data within a bin of 45 minutes centered around the time written in the figure and also marked by the arrows in Fig. 8.3 a. The solid line is the result of fitting a power law to the data points. (a) Inverted spectrum (i.e., $\alpha > 0$, arrow “a” in Fig. 8.3). (b) Flat spectrum (i.e., $\alpha = 0$, arrow “b” in Fig. 8.3). (c) Optically thin spectrum (i.e., $\alpha < 0$, arrow “c” in Fig. 8.3), also including the data point observed by OVRO at 15 GHz, showing how well the spectral shape fits a pure power law from 5 to 15 GHz.

Frequency	a	b	c
5 GHz	$-9.4 \cdot 10^{-3}$	$-4.0 \cdot 10^{-3}$	0.16
8 GHz	$-7.6 \cdot 10^{-3}$	$-10.3 \cdot 10^{-3}$	0.13
10 GHz	$-8.7 \cdot 10^{-3}$	$-4.3 \cdot 10^{-3}$	0.12

Table 8.1: Best fit parameters used for subtraction the long-term trend of the light curves in form of a parabola.

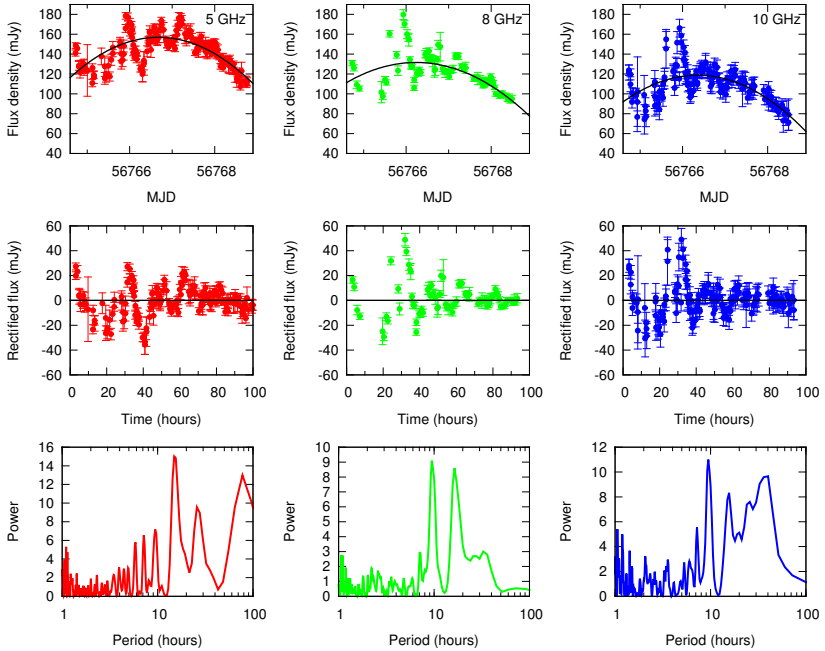


Figure 8.5: First row: Original lightcurves at indicated frequencies, same colors as in Figure 1. The long-term trend was fitted with a parabola, shown as the solid black line. Second row: The fitted parabola was subtracted from the original light curves in order to remove the long-term trend. The solid line shows a sine wave of the most powerful period from the Lomb-Scargle timing analysis. Third row: Lomb-Scargle periodograms of the parabola subtracted light curves. The 5 GHz data shows a highly significant peak at $P = 14.9 \pm 0.6$ h, while both 8 and 10 GHz show a significant peak at $P = 9.5 \pm 0.2$ h.

Frequency	A (mJy)	ϕ_0	B (mJy)
5 GHz	12.0 ± 1.2	-0.05 ± 0.01	-3.82 ± 0.74
10 GHz	7.28 ± 0.48	0.27 ± 0.01	0.00 ± 0.32

Table 8.2: Best fit parameters resulting from fitting a sine wave (Eq. 8.5) to the folded data (Fig. 8.6).

at a period of $P_{5\text{ GHz}} = 14.9 \pm 0.6$ h, while the 8 GHz and 10 GHz data both have $P_{8\text{ GHz}} = P_{10\text{ GHz}} = 9.5 \pm 0.2$ h. In all cases the peaks are highly significant, with a false alarm probability of the Fisher randomization test (Linnell Nemec & Nemec 1985) close to zero.

Figure 8.6 shows the result of folding the 5 and 10 GHz rectified light curves (i.e., the parabola-subtracted data shown in Fig. 8.5, second row) on the most significant periods from the timing analysis. These two frequencies were chosen, because the sinusoidal modulation is best visible. The solid line in each figure is the result of fitting a sine wave of the form

$$f_4(\phi) = A \sin 2\pi(\phi - \phi_0) + B \quad (8.5)$$

to the folded data, the resulting best fit parameters are shown in Table 8.2. The amplitude A differs from zero very significantly, i.e., 10σ for 5 GHz and 15σ for 10 GHz.

8.3.5 Polarization

With the data obtained in our observations we can put an upper limit to the linear polarization of 2%. This result is in agreement with the findings of Peracaula et al. (1997), who report on linear polarization of $\sim 2\%$.

8.3.6 Comparison to *Fermi*-LAT data

The first and second row of Fig. 8.3 show the γ -ray fluxes from LS I +61°303 and their photon index respectively. The data were obtained by fitting a power law to every time bin of half a day, restricting the

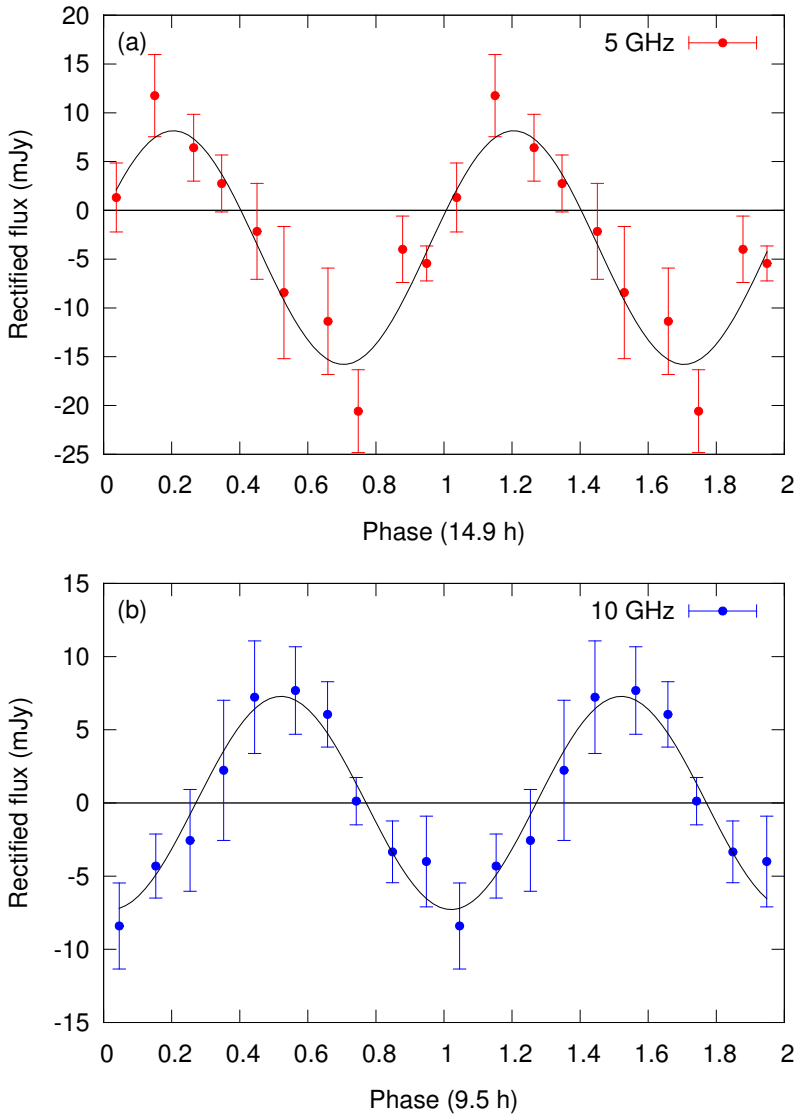


Figure 8.6: Rectified fluxes folded on the most significant periods from the timing analysis. The solid line is the result of fitting a sine wave to the folded data. (a) $\nu = 5$ GHz, $P = 14.9 \pm 0.6$ h, (b) $\nu = 10$ GHz, $P = 9.5 \pm 0.2$ h.

analysis to the energy range $E = 0.1 - 3$ GeV (i.e., same energy range as in Chapter 7). A fit of a sine wave to the photon index data results in a period of $P = 1.78 \pm 0.09$ d, a value well compatible with the period ($P = 1.77 \pm 0.2$ d) of the sine wave fitted to the radio spectral index reported above. The phases of the two sine waves match exactly, but they have not been varied in the fit either. However, we note that the small number of data points and the signal to noise ratio does not allow for a very strong statement here.

8.4 Conclusion

The here presented light curves at 5, 8, and 10 GHz reveal that the radio flux of LS I +61°303 at these frequencies is significantly variable on time scales less than one day (see Fig. 8.3). We find hints for a periodic modulation in the order of 10–15 hours (see Fig. 8.5). The fact that the period, $P = 14.9 \pm 0.6$ h, which we find in the 5 GHz data, is significantly longer than the period, $P = 9.5 \pm 0.2$, in the 10 GHz data is consistent with the picture that the 10 GHz data come from a region in the jet closer to the engine than the 5 GHz data.

Quasi periodic microflares in the radio flux from LS I +61°303 have been reported before. Taylor et al. (1992) carried out two sessions of VLBI observations of the source at 5 GHz. During session 1 the flux was rising, and during session 2, five days later, the flux was decreasing. They report on a “steplike pattern with a characteristic time scale of $\sim 10^3$ s” (i.e., ~ 17 minutes) in a radio light curve observed during session 2 (see their Fig. 2 b). When removing the long-term trend in this lightcurve, the steplike pattern would have a sinusoidal shape with an amplitude in the order of 10 mJy, similar to the oscillations that we report here.

Another report on micro-flares comes from Peracaula et al. (1997), who observed oscillations on a time scale of ~ 1.4 h in a radio lightcurve obtained by VLA observations at 5 GHz, the amplitude being ~ 1 mJy (see their Fig. 4). Also in this case the lightcurve covered an epoch of decreasing flux (see their Fig. 1 middle panel). They further report on linear polarization of $\sim 2\%$. Both the microflares and

the polarization results cannot be confirmed or denied by our observations, because our observations have a lower SNR than the observations by the VLA.

It is worth of note that all three cases of quasi periodic microflaring activity (i.e., Taylor et al. 1992, Peracaula et al. 1997, and our results presented here) were observed during decreasing radio fluxes of LS I +61°303. In the microquasar scenario, optically thin injections of relativistic particles are expected during the optically thin transient jet occurring after the optically thick main flare. Further observations of the optically thin declining phase of the periodic radio outbursts are necessary to further investigate on the physical processes behind these quasi periodic oscillations.

Chapter 9

Radio emission from the Be/black hole binary MWC 656

Credit: Dzib, S., Massi, M., & Jaron, F., A&A, 580, L6, 2015, reproduced with permission © ESO.

Abstract

MWC 656 is the recently discovered first binary system case composed of a Be-type star and an accreting black hole. Its low X-ray luminosity indicates that the system is in a quiescent X-ray state. The aim of our investigation is to establish if the MWC 656 system has detectable radio emission and if the radio characteristics are consistent with those of quiescent black hole systems. We used three archived VLA data sets, one hour each at 3 GHz, and seven new VLA observations, two hours each at 10 GHz, to produce very high sensitivity images down to $\sim 1 \mu\text{Jy}$. We detected the source twice in the new observations: in the first VLA run, at apastron passage, with a flux density of $14.2 \pm 2.9 \mu\text{Jy}$ and by combining all together the other six VLA runs, with a flux density of $3.7 \pm 1.4 \mu\text{Jy}$. The resulting combined map of the archived

observations has the sensitivity of $1\sigma = 6.6 \mu\text{Jy}$, but no radio emission is detected there. The radio and X-ray luminosities agree with the behaviour of accreting binary black holes in the hard and quiescent state. In particular, MWC 656 in the L_X, L_R plane occupies the same region as A0620–00 and XTE J1118+480, the faintest known black holes up to now.

9.1 Introduction

In 2010 the gamma-ray source AGL J2241+4454 was detected by the AGILE satellite (Lucarelli et al. 2010). Within the positional error circle of the satellite Williams et al. (2010) found the emission-line Be star MWC 656 (also known as HD 215227). The first suggested classification for MWC 656 was B3 IVne+sh, where n and e indicate broad lines and Balmer emission, and sh denotes the presence of shell lines, indicated by a sharp central absorption in the line. The V/R ratio of the $H\gamma$ emission changed significantly in one day, which is unusually fast for most Be stars and Williams et al. (2010) pointed out some resemblance of the spectral properties of this newly identified gamma-ray source to the gamma-ray binary LS I +61°303 and its $H\alpha$ variations. The star MWC 656 is at a Galactic latitude of $b = -12^\circ$; at a distance of $d = 2.6 \pm 0.6$ kpc the star results well below the Galactic plane at $z = -560 \pm 200$ pc. This is an extreme distance for a normal OB star and Williams et al. (2010) suggested a runaway star, which reached the current position by a supernova explosion of the companion star. Timing analysis of variations in the optical photometry, interpreted as orbital modulation, resulted in a period of 60.37 ± 0.04 days with the epoch of maximum brightness at HJD 2453243.3 ± 1.8 .

The binary hypothesis was tested with a radial velocity study by Casares et al. (2012). Radial velocities folded with the 60.37 d of Williams et al. (2010) revealed a sine-like modulation. Casares et al. (2012) by the rotational broadening $v \sin i \sim 346 \text{ km s}^{-1}$ estimated the inclination of the orbit $i > 66^\circ$ and a mass of the compact object in the range $M_c \sim 2.7 - 5.5 M_\odot$. Moreover, Casares et al. (2012) found that the main parameters of the $H\alpha$ emission line (equivalent

Table 9.1: MWC 656 observations and final parameters of maps.

Epoch	Date (day.month hh:mm)	Julian Date	Φ	Synthesized beam ($\theta_{\text{maj}}['']$ \times $\theta_{\text{min}}['']$; P.A.[$^{\circ}$])	rms noise ($\mu\text{Jy beam}^{-1}$)	Peak ($\mu\text{Jy bm}^{-1}$)	Flux $\pm \sigma^a$ (μJy)
X-band observations in 2015							
1	22.02 19:15	2457076.302	0.49	1.17×1.09 ; 101.7	2.9	9.9	14.2 ± 2.9
2	28.02 19:30	2457082.313	0.58	1.15×1.08 ; 104.3	3.8	...	<11.4
3	07.03 22:10	2457089.424	0.70	2.69×0.36 ; 58.8	2.3	...	<6.9
4	08.03 23:04	2457090.461	0.72	1.62×1.06 ; 84.6	2.4	...	<7.2
5	03.04 19:36	2457116.317	0.15	1.89×1.09 ; 89.3	2.2	...	<6.6
6	10.04 17:01	2457123.209	0.26	1.30×0.97 ; -20.6	2.7	...	<8.1
7	12.04 20:25	2457125.351	0.30	1.10×1.02 ; -21.9	2.3	...	<6.9
2 - 7				0.84×0.70 ; -75.1	1.02	3.47	3.7 ± 1.4
1 - 7				0.82×0.70 ; -75.1	0.95	4.15	4.5 ± 1.2
S-band observations in 2012							
1	05.10 04:38	2456205.693	0.06	0.48×0.41 ; 12.3	12.6	...	<37.8
2	15.10 08:03	2456215.835	0.23	0.66×0.44 ; 89.6	10.1	...	<30.3
3	06.12 04:54	2456267.704	0.09	0.61×0.50 ; 83.0	11.1	...	<33.3
1 - 3				0.51×0.45 ; 80.5	6.6	...	<19.8

^aUpper limits at three times the noise level.

width, full width at half maximum, and centroid velocity) result to be modulated by the proposed orbital period.

The turning point in this research came with the new optical observations by Casares et al. (2014). To improve the radial velocity curve of the Be star, FeII emission lines from the innermost region of the Be disk were used instead of stellar broad absorption lines contaminated by the circumstellar wind emission lines. On the other hand, the spectra show an HeII 4686 Å double-peaked emission line, indicating a disk, whose centroid is modulated with the same 60.37 day period, but in antiphase with respect to the radial velocity of the Be star, as obtained from the FeII line (their Fig. 3). This important observation therefore hints at an accretion disk around an invisible companion. The orbital solution resulted in $\Phi_{\text{periastron}} = 0.01 \pm 0.10$ (phase zero set to HJD 2453243.7). With new observations, the authors were also able to obtain a better spectral classification for the Be star, and determined a B1.5-B2 III classification. Given the mass of this star, 10-16 M_{\odot} , the implied companion mass is 3.8-6.9 M_{\odot} . This makes MWC 656 the first clear case of a Be-type star with a black hole companion. The case of LS I +61°303 is, in fact, still unclear because of the uncertainties in the values of mass function and inclination of the orbit (Massi 2004; Casares et al. 2005).

Observations with XMM-Newton at $\Phi = 0.08$ by Munar-Adrover et al. (2014) proved that MWC 656 is indeed an X-ray binary system. The X-ray luminosity of $\sim 10^{31} \text{erg s}^{-1}$ points to a stellar mass black hole in quiescence. The quiescent X-ray state is one of the X-ray states of an accreting black hole similar to the low-hard X-ray state. For a compact object of a few solar masses, the low/hard state corresponds to $L_X \sim 10^{36} \text{erg s}^{-1}$ but may drop to $L_X = 10^{30.5} - 10^{33.5} \text{erg s}^{-1}$ (McClintock & Remillard 2006) at its lowest phase, called the quiescent state. The X-ray luminosity in the quiescent and low/hard X-ray states correspond to a radiatively inefficient, “jet-dominated” accretion mode (Fender et al. 2003). In this mode, only a negligible fraction of the binding energy of the accreting gas is directly converted into radiation. Most of the accretion power emerges in kinetic form, as shown for Cygnus X-1 by Gallo et al. (2005), and for AGNs through the rela-

tionship between the Bondi power and the kinetic luminosity (Merloni & Heinz 2007, and references therein). That is, during the low-hard and quiescent states the liberated energy of the accretion is thought to be converted into magnetic energy, which powers the relativistic jet observed in these states (Gallo et al. 2003; Fender & Belloni 2004; Gallo et al. 2006; Smith 2012).

The origin of the X-ray emission during the low-hard and quiescent states is still controversial. The emission may be due to a Comptonizing corona and/or to the jet (see Gallo et al. 2006). Nevertheless, it is well established that the X-ray emission is related to the radio emission from the jet (Gallo et al. 2003, 2006; Merloni et al. 2003). This important nonlinear scaling between X-ray and radio luminosities, L_X , L_R , has been demonstrated to hold, with the addition of a mass term, across the entire black hole mass spectrum, from microquasars to AGN (Merloni et al. 2003).

Therefore, if a jet is associated with MWC 656, its radio emission should be consistent with the L_X , L_R relationship. The aim of our investigation is to establish if the system MWC 656 has an associated radio emission and if the radio emission fulfills the L_X , L_R relationship. In this letter, we present new radio observations in the direction of this system. Section 9.2 describes the observations and the data reduction. In Sect. 9.3 we report on our results. Section 9.4 describes MWC 656 in the context of the L_X , L_R relationship, and finally, Sect. 9.6 gives our conclusions.

9.2 Observations

We obtained seven new X-band (8 to 12 GHz) observations with the Karl G. Jansky Very Large Array (VLA) of the National Radio Astronomy Observatory (NRAO) in its B configuration. These observations were made under project 15A-013. The receiver was used in semicontinuum mode with the 3 bit sampler and 32 different spectral windows (with bandwidths of 125 MHz) were recorded simultaneously to cover the full band.

Each observing session ran for two hours and was organized as

follows. First, we spent 4.5 minutes on scans for instrument setups as recommended by NRAO¹. Then, we observed a 5.5 minute scan on the phase calibrator J2255+4202, and the large scan was performed to take the slewing time into account. Then we observed nine cycles of 10.6 minutes on the target followed by 1.0 minutes on the phase calibrator. We finished the observation with a 5.5 minutes scan in the flux calibrator 3C147, which was also used as the bandpass calibrator. We spent ~ 95 minutes on target per epoch, or a total of ~ 668 minutes.

The data were edited and calibrated using the Common Astronomy Software Applications (CASA 4.2.2) package, and the VLA calibration pipeline in its 1.3.1 version. After calibration, images were produced with pixel sizes of 0.2 arcseconds, a natural weighting, and a multifrequency synthesis scheme (e.g., Rau & Cornwell 2011). The noise levels reached for each individual observation was about $\sim 3 \mu\text{Jy}$ (see Table 9.1). Additionally, we produced images from the concatenated UV data from the epoch 2 to 7 and of the seven observations to reach lower noise levels of $1.02 \mu\text{Jy}$ and $0.95 \mu\text{Jy}$, respectively. These noise levels are in agreement with the theoretically expected values.

Finally, we also performed the data reduction of three archived S-band (2-4 GHz) data sets taken with the VLA in its A configuration; these are part of the project 12B-061. Each individual epoch runs for 1.0 hours. The receiver was also used in semicontinuum mode with the 8 bit sampler and 16 different spectral windows (with bandwidths of 125 MHz each) were recorded simultaneously to cover the full band. These observations used the quasar 3C48 as the flux and bandpass calibrator, and quasar J2202+4216 as the phase calibrator.

The data were edited, calibrated, and imaged following the same scheme as the new observations. The resulting sensitivity limits are $\sim 11 \mu\text{Jy}$ and $6.6 \mu\text{Jy}$, for the maps of individual epochs and for the map of the concatenated epochs (see also Table 9.1), respectively. These values are also in agreement with those theoretically expected.

¹<https://science.nrao.edu/facilities/vla/docs/manuals/obsguide>

9.3 Results

A source with a peak 3.4 times the noise level was detected in the first observation at orbital phase $\Phi = 0.49$, i.e., at apastron passage. The source is coincident with the position of MWC 656 (see Fig. 9.1, center). A Gaussian fit to the source (using *imfit* in CASA) yields the flux density of the source to be $14.2 \pm 2.9 \mu\text{Jy}$. In the remaining observations, however, we do not detect any peak above 2.6 times the noise level of the images (see Fig. 9.2). By adding these six remaining observations, we detected a source with a peak 3.4 times the noise level, which is coincident in position with MWC 656 and with the source detected in the first epoch (see Fig. 9.1, right). The flux density in this case was $3.7 \pm 1.4 \mu\text{Jy}$. The two images of Fig. 9.1 (center, right) were produced with independent data sets, and support our detection of the radio counterpart of MWC 656. Interestingly, the flux in the first image (Fig. 9.1, center) has a flux density almost three times higher than that in Fig. 9.1, right, and this increased flux is occurring at apastron. We produce a final map by concatenating the data of the seven observed epochs. The source is now detected at levels of 4.4 times the noise in the image (Fig. 9.1, left). The Gaussian fit to the source yields the flux density of the source to be $4.5 \pm 1.2 \mu\text{Jy}$, at the position $\text{RA}=22^{\text{h}}42^{\text{m}}57^{\text{s}}305 \pm 0^{\text{s}}005$, $\text{DEC}=+44^{\circ}43'18''.23 \pm 0''.08$, and is consistent with a point like structure and parameters of Table 9.1. The source position is in good agreement with the optical position of MWC 656, $\text{RA}=22^{\text{h}}42^{\text{m}}57^{\text{s}}30295$, $\text{DEC}=+44^{\circ}43'18''.2525$ (van Leeuwen 2007).

Finally, concerning the archived data (Table 9.1), we did not detect the source in any single S-band epoch, nor in the final image of concatenated observations at levels above $20 \mu\text{Jy}$.

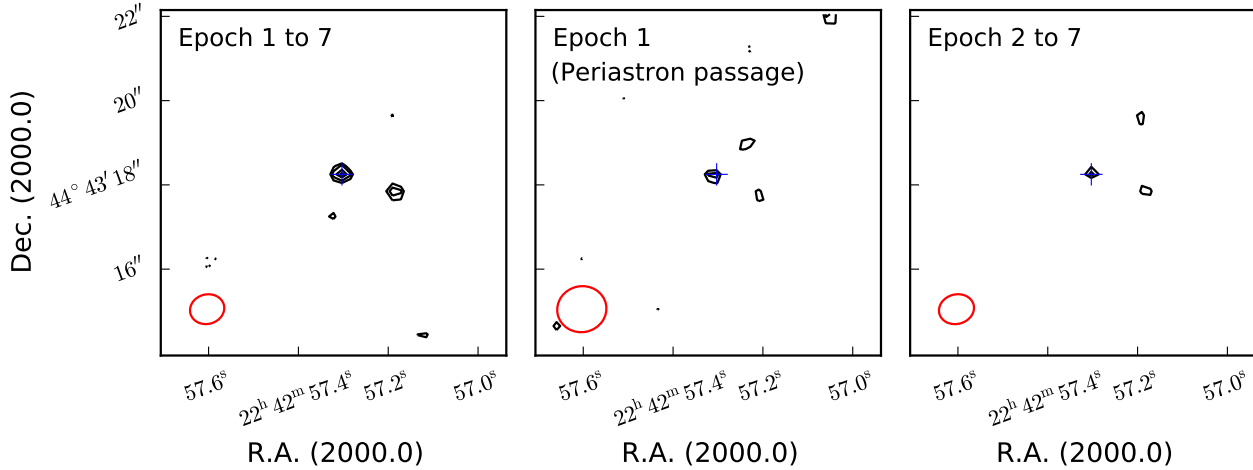


Figure 9.1: VLA images with radio emission at the MWC 656 position. **Left:** image of the concatenated X-band data from Epoch 1 to 7. **Center:** Epoch 1. **Right:** Image of the concatenated X-band data from Epoch 2 to 6. Contour levels are -3, 2.8, 3.2, 3.8, and 4.2 times the noise levels of the image (see Table 9.1). The red ellipse at the bottom left is the corresponding synthesized beam. The blue cross indicates the optical position of MWC 656.

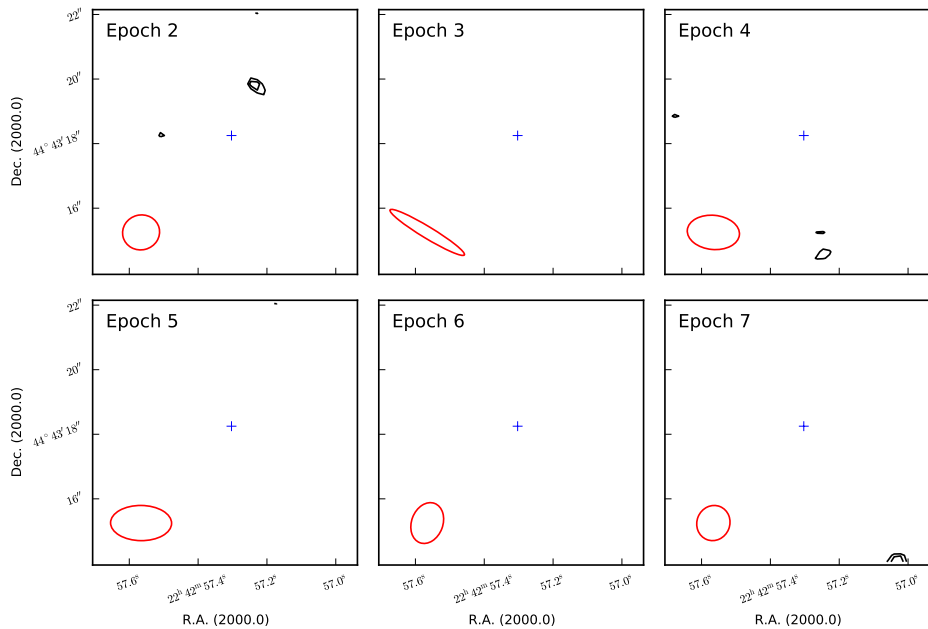


Figure 9.2: VLA images from epoch 2 to 7. The red circle at bottom-left is the synthesized primary beam. Contours are at -3, 2.6, and 3 times the noise level. The blue cross at the center represents the position of MWC 656. The source remains undetected in each single image. The rms of the images and upper limits for the flux density of MWC 656 are given in Table 9.1.

9.4 MWC 656 in the context of the L_X , L_R relationship

The radio flux values of $3.7 \pm 1.4 \mu\text{Jy}$ and $14.2 \pm 2.9 \mu\text{Jy}$ at 10 GHz, for a distance of 2.6 kpc, and assuming a nearly flat spectrum, corresponds to a L_R at 8.6 GHz of $2.6 \times 10^{26} \text{ erg s}^{-1}$ and $9.9 \times 10^{26} \text{ erg s}^{-1}$, respectively. Munar-Adrover et al. (2014) determined an X-ray luminosity of $L_X = 1.2 \times 10^{31} \text{ erg s}^{-1}$ from an observation at $\Phi = 0.08$. We report our new data of MWC 656 along with the measurements from Corbel et al. (2013). Figure 9.3 shows (square/black) the radio and X-ray luminosities for the 24 Galactic accreting binary BHs in the hard and quiescence states reported in Fig. 9 of Corbel et al. (2013). The position of MWC 656, given in red color, is rather close to the position of A0620+00 and XTE J1118+480, which are the weakest quiescent black holes known so far (Gallo et al. 2006, 2014).

9.5 Updated SED

The SED obtained by observations of MWC 656 at different wavelengths as presented in Fig. 2 in Aleksić et al. (2015) contained only upper limits in the radio and GeV γ -ray regimes. Now, after the radio detection presented in this chapter, and after the confirmation of the Lucarelli et al. (2010) observations of GeV γ -ray emission from MWC 656 by Alexander & McSwain (2015), we can put these two observational results on the SED. In Fig. 9.4 the updated SED for MWC 656 is shown. The peak in the GeV regime justifies a classification as γ -ray binary.

9.6 Conclusions

Deep VLA observations of the BH-Be system MWC 656 have provided us with the first radio detection of an accreting stellar mass black hole with a Be star as companion. Along with a level of emission of $3.7 \pm 1.4 \mu\text{Jy}$, determined combining six observations at the different

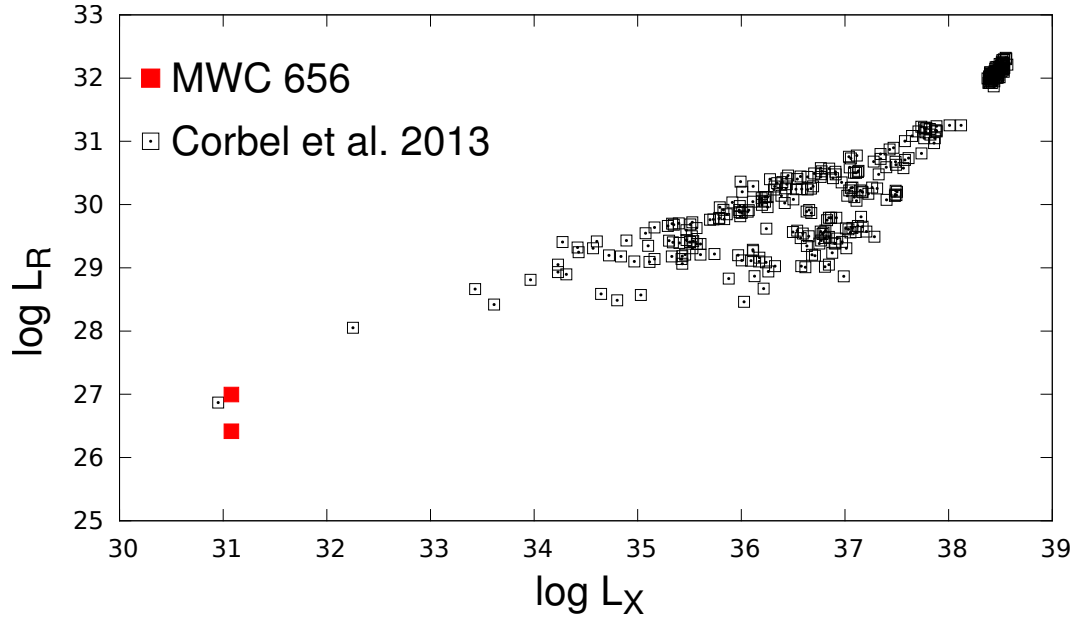


Figure 9.3: Radio (8.6 GHz) vs X-ray luminosity (1–10 keV) diagram. Black squares indicate the positions of the 24 Galactic accreting binary black holes in the hard and quiescence states, as in Fig. 9 of Corbel et al. (2013, ; i.e., without the upper limits and neutron stars there present). The position of MWC 656 is indicated by two red squares for the two fluxes of $3.7 \mu\text{Jy}$ and $14.2 \mu\text{Jy}$. The position of MWC 656 is rather close to the faintest accreting black hole systems known so far, A0620-00 (triangle, Gallo et al. 2006) and XTE J1118+480 (asterisk, Gallo et al. 2014).

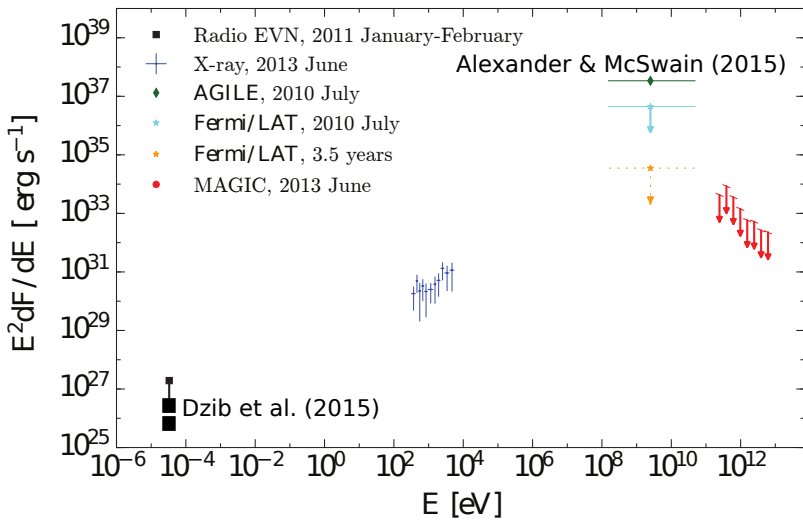


Figure 9.4: Updated SED for MWC 656. The original figure by Aleksić et al. (2015) (Fig. 2 in their paper) is modified by adding the radio detection reported in this chapter (Dzub et al. 2015) and the confirmation of the GeV detection of Lucarelli et al. (2010) by Alexander & McSwain (2015).

orbital phases $\Phi = 0.58 - 0.72$ and $\Phi = 0.15 - 0.30$, we detected in a single observation around apastron ($\Phi = 0.49$) the flux density of $14.2 \pm 2.9 \mu\text{Jy}$.

Several works have placed significant constraints on the L_X - L_R luminosities of quiescent systems (e.g., Gallo et al. 2006, 2014; Calvelo et al. 2010; Miller-Jones et al. 2011). The nonsimultaneous XMM-Newton X-ray observation by Munar-Adrover et al. (2014) at orbital phase $\Phi = 0.08$ also allowed us to test for MWC 656 the X-ray/radio correlation for black holes. The position of MWC 656 is close to the faintest black holes known so far, which are A0620-00 and XTE J1118+480. The secondary star in A0620-00 is a $0.7 M_\odot$ K3-K4V star in a 7.75 h orbit around the black hole (Gallo et al. 2006). The companion star in XTE J1118+480 is a K5-K8V star with an orbital period of 4.08 h (Gallo et al. 2014, and references therein). MWC 656 has an orbit of ~ 60 days and the companion star is a $10\text{-}16 M_\odot$ Be star. Our observations support, therefore, the universality of the L_X , L_R relationship, which is intimately related to the accretion-ejection coupling process, which seems to be invariant to different forms of accretion.

Acknowledgements

We acknowledge Pere Munar-Adrover, Luis F. Rodríguez and Alberto Sanna for comments and suggestions in the manuscript. The data set of Fig. 9.3 is provided by S. Corbel with support from the Agence Nationale de la Recherche for the CHAOS project. The National Radio Astronomy Observatory is operated by Associated Universities Inc. under cooperative agreement with the National Science Foundation.

Chapter 10

Conclusion and outlook

10.1 Conclusions

The conclusions of this thesis are:

1. The radio outbursts occur with a period of $P_{\text{average}} = 26.704 \pm 0.004$ days (Jaron & Massi 2013; Massi & Torricelli-Ciamponi 2016), in agreement with the previous result by Ray et al. (1997). This period, when taking into account the phase jump during the minimum of the long-term modulation, is a very stable feature of the source and is well explained as the result from the beating between the orbital period and the precession period of a relativistic jet.
2. The apparent disappearance of the orbital period during certain epochs of the *Fermi*-LAT GeV lightcurve (Hadasch et al. 2012) is the result of a previously undetected periodic apastron GeV peak, which is correlated to the radio emission, i.e., subject to the same orbital drift (Gregory et al. 1999; Jaron & Massi 2013; Massi & Torricelli-Ciamponi 2014), disturbing the timing analysis in such a way that the orbital period cannot be detected when the apastron GeV peak is too much detached from the periastron GeV, which remains stable in orbital phase (Jaron & Massi 2014). In addition, timing analysis reveals that the apastron GeV

peak is modulated by the orbital period P_1 and the precession period P_2 , while the periastron GeV peak is only modulated by P_1 (Jaron & Massi 2014), a result which is in agreement with the findings of Ackermann et al. (2013), who report that only the apastron GeV emission ($\Phi = 0.5 - 1.0$) is subject to the long-term modulation, while the periastron GeV emission ($\Phi = 0.0 - 0.5$) is not.

3. The physical model of a self-absorbed, adiabatically expanding relativistic jet (Kaiser 2006) precessing with P_2 (Massi & Torricelli-Ciamponi 2014), which reproduces the observed radio light curves by the GBI and also fits the entire radio observations since 1977 until 2014 (Massi & Torricelli-Ciamponi 2016), has been extended to include two injections along the orbit, taking into account inverse Compton (IC) scattering of stellar seed photons (external inverse Compton, i.e., EIC) and of jet seed photons (synchrotron self-Compton, SSC), reproduces the observed timing characteristics of having P_1 and P_2 at apastron, and only P_1 at periastron. In addition, it reproduces the average orbital modulation of the GeV and the radio emission, here in particular the absence of a periastron radio peak due to catastrophic IC losses leading to a jet too short for radio emission (Jaron et al. submitted).
4. The binary star MWC 656, being the first case of a Be type star and a proven black hole (Casares et al. 2014), has now been detected in radio by Dzib et al. (2015). This observation, together with the detection in the GeV regime by the AGILE satellite (Lucarelli et al. 2010; Alexander & McSwain 2015) puts this object in strong relationship to LS I +61°303. We conclude that, Be-BH systems can be emitters of radiation up to the GeV regime, and consequently an accreting BH scenario could apply for LS I +61°303 as well.

We conclude that the observations, at radio and γ -ray wavelengths, corroborate the scenario of a conical jet, precessing with period $P_2 \approx 26.9$ days, periodically (with period $P_1 \approx 26.5$ days) refilled with electrons twice along the orbit, once at periastron and a second time towards apastron. The electrons at periastron lose their energy by up-scattering stellar photons to γ -ray (EIC), explaining the absence of a periastron radio peak and the absence of the precession period P_2 from the power spectrum. At apastron, however, lower energetic losses allow electrons to produce synchrotron emission in the radio band, and the jet can accelerate to relativistic velocities giving rise to strong variable Doppler boosting and the presence of P_2 in the power spectrum. The long-term modulation of the radio and γ -ray emission at apastron is the result of the beating between the two close periods P_1 and P_2 .

10.2 Outlook

Future investigations concerning LS I +61°303 could include the following topics.

1. We observed LS I +61°303 at three different radio wavelengths with the 100-m telescope in Effelsberg with unprecedented sampling rate for a multiwavelengths observation. Our preliminary results show evidence for significant variability in the order of ~ 10 hours, also hinting at possible periodicity and correlation between the observed radio frequencies. These results could contribute to future investigations on transient phenomena associated with a jet in LS I +61°303.
2. mm-VLBI observations of LS I +61°303 could produce images with a higher resolution than the VLBI images obtained so far, and consequently could help the better understand the nature of the precessing elongated structures observed in these images.

3. The physical model presented in Chapter 7 reproduces the timing characteristics and the orbital flux modulation at radio and GeV wavelengths. However, there is still the possibility of improving the model by including, e.g., the equatorial disk of the Be star as a possibility to better fit the model during phases around periastron.
4. The same physical model of Chapter 7 can serve as a basis for hydrodynamical simulations of an accretion scenario for LS I +61°303 in order to probably better understand the acceleration mechanism of a jet and to model the shape and the evolution of VLBI images of the source.

Appendix A

Methods

A.1 Programs and scripts

For the analysis of the data a number of programs and scripts were written by the author of this thesis. In this chapter a short description of each of these programs is given. The program “binfold” to perform a binned folding deserved a more detailed discussion. Most of the programs were written in C (Kernighan & Ritchie 1988) and most of the script were written in AWK. The programs in C were compiled with the GNU Compiler Collection (gcc) version 4.6.3 installed under the GNU/Linux distribution Ubuntu 12.04.1 LTS (Ubuntu 2013).

A.1.1 Starlink

Here I describe how to install the UK Starlink software on your personal computer. First, download the archive appropriate for your system at <http://starlink.jach.hawaii.edu/starlink>. Then unpack it into a directory of your choice. Before you can run a program like PERIOD you have to set the environment variable “STARLINK_DIR” to Starlink’s directory and then source the file `.../etc/profile`, where “...” has to be replaced by the name of Starlink’s directory. PERIOD is then run by simply typing the command in a shell. It will run in the text mode.

Note: The version used for the timing analysis in this thesis is “Kapuahi”.

A.2 Bifold

A.2.1 Introduction

The light curves of astronomical objects often contain periodicities. They are the result of periodic behaviour of the system itself like, e.g., the orbital periodicity. In the case of LS I +61°303 the light curves are modulated by the orbital period and the precessional period of the relativistic jet. Folding is a technique to explore the ideal shape of the light curve which may be covered by random fluctuations.

A.2.2 Simple Folding

A light curve is a time series taken from an astronomical object over a certain time interval. Let us denote the times of the observations by t_i and the corresponding fluxes by f_i , with $i = 1, 2, \dots, N$. The observation times t_i do not necessarily have to be equally spaced.

The simplest way to produce a folded light curve is to convert the observation times t_i to phases ϕ_i with respect to a periodicity P :

$$\phi_i = \frac{t_i - t_0}{P} - \text{int} \left(\frac{t_i - t_0}{P} \right), \quad (\text{A.1})$$

where $\text{int}(x)$ returns the integer part of x and t_0 is the time of zero phase.

The graph of the pairs (ϕ_i, f_i) is the simple folded light curve. If the period P is well chosen, then the graph should show a distinct pattern.

A.2.3 Binned Folding

The simple folding has certain disadvantages. First, there is the problem what to do if two phases ϕ_i and ϕ_j happen to be equal. If the values are listed in a text file, then a program like gnuplot simply overwrites

the first appearance of ϕ_i , so in the end only (ϕ_j, f_j) is plotted. Second, the fluxes f_i are stored together with individual errors Δf_i . The simple folded light curve shows no improvement in terms of error bars compared to the original one.

One solution for the above mentioned problems is to perform a binned folding instead. For this purpose the phase interval is divided into n bins. The l^{th} bin is the interval

$$\Phi_l = \left[\frac{l-1}{n}, \frac{l}{n} \right). \quad (\text{A.2})$$

Each phase ϕ_i falls into exactly one of these bins. The bin number b_i is

$$b_i = \text{int}(n \cdot \phi_i). \quad (\text{A.3})$$

Let us define the set B_l as the set of indices i which fall into the l^{th} phase bin:

$$B_l = \{i \in \mathbb{N} \mid \phi_i \in \Phi_l\}. \quad (\text{A.4})$$

For each bin the average flux is calculated:

$$\bar{f}_l = \frac{1}{m_l} \sum_{k \in B_l} f_k, \quad (\text{A.5})$$

where m_l is the number of elements in B_l . Alternatively, one can perform the weighted averaging:

$$\bar{f}_l = \frac{1}{\sum_{k \in B_l} \Delta f_k^{-2}} \sum_{k \in B_l} \frac{f_k}{\Delta f_k^2} \quad (\text{A.6})$$

The fluxes f_i are recorded with individual errors Δf_i . Error propagation yields

$$\Delta \bar{f}_l = \sqrt{\sum_{k \in B_l} \left(\frac{\partial \bar{f}_l}{\partial f_k} \Delta f_k \right)^2} \quad (\text{A.7})$$

$$= \left(\sum_{k \in B_l} \Delta f_k^{-2} \right)^{-\frac{1}{2}}. \quad (\text{A.8})$$

The error $\Delta\bar{f}_l$ becomes smaller as the number of observations which fall into the bin increases.

One more note on the error: There is another information about the fluxes in each bin which I find rather useful. It is the variance of the fluxes:

$$\text{Var}(B_l) = \frac{1}{m_l - 1} \sum_{k \in B_l} (f_k - \bar{f}_l)^2. \quad (\text{A.9})$$

It is a measure for the scatter of the fluxes around the mean value. For a good clustering the sum of these variances should become small.¹ I would somehow like to include this information in the plot of the folded light curve. It is now the question if this is to be included in the above mentioned error, so that

$$(\Delta\bar{f}_l)_{\text{total}}^2 = \Delta\bar{f}_l^2 + \text{Var}(B_l), \quad (\text{A.10})$$

or if the variances are plotted, e.g., as additional errorbars.

The next question is: Where to put the flux \bar{f}_l in the phase bin Φ_l . The simplest approach might be to put it at

$$\frac{1}{2} \left(\frac{l}{n} + \frac{l-1}{n} \right) = \frac{2l-1}{2n}, \quad (\text{A.11})$$

i.e., in the middle of each bin. Another choice could be the mean value of the phases:

$$\bar{\phi}_l = \frac{1}{m_l} \sum_{k \in B_l} \phi_k. \quad (\text{A.12})$$

There is also the possibility to include an error bar in the “x”-direction. Two choices come to my mind. The simplest could be just half the width of a bin:

$$\Delta\phi_l = \frac{1}{2n}. \quad (\text{A.13})$$

The other choice could be the standard deviation of the phases in each bin:

$$\sigma^2(\phi_l) = \frac{1}{m_l - 1} \sum_{k \in B_l} (\phi_k - \bar{\phi}_l)^2. \quad (\text{A.14})$$

¹ Indeed, this is the quantity given as power in Stellingwerf’s Phase Dispersion Minimization (PDM) algorithm, divided by the overall variance. That is why low values correspond to greater significance in PDM.

INPUTFILE	File name of the input file
OUTPUTFILE	File name of the output file
P	Periodicity used for the folding
T0	Time of zero phase
BINS	Number of bins
A	Coefficient for the propagated error
B	Coefficient for the variance
WEIGHTED	Perform weighted averaging if not set to zero.
PLACEPHI	0 for middle of bin, 1 for average phase of bin
ERRORPHI	0 for half width of bin, 1 for standard deviation

Table A.1: List of the keywords known to binfold.

A.2.4 Binfold

Binfold is a computer program I have written in C which performs a binned folding as described in the section above. The user interface is a configuration file. This is just a text file which contains rows of keyword-value-pairs. Table A.1 gives a list of keywords known to the program. In the following the keywords are explained in more detail.

The *inputfile* has to contain rows of time, flux and error, separated by white space. The *outputfile* will be in the format: phase, delta phase, flux, delta flux.

The periodicity P has to be in the same units as the timing information in the input file. The same holds true for $T0$.

$BINS$ has to be an integer number greater than zero.

The coefficients A and B are to be understood as follows. In equation (A.10) I propose to sum the square of the propagated error and the intrinsic variance of the bin. In the software this formula is altered in this way:

$$(\Delta \bar{f}_i)_{\text{total}}^2 = A \cdot \Delta \bar{f}_i^2 + B \cdot \text{Var}(f_i). \quad (\text{A.15})$$

So, this is what the coefficients A and B mean.²

With the keyword *WEIGHTED* you can chose whether equation (A.5) or (A.6) is used for the averaging. When set to a value different

²In this work I set $A = 1$ and $B = 0$ all the time.

from zero, weighted averaging will be performed.

Set *PLACEPHI* to 0 in order to place the folded fluxes in the middle of each phase bin and to 1 if you would like it in the average phase position.

When *ERRORPHI* is set to 0 the error bar in *x*-direction is always half the width of the phase bin. Setting this to 1 means to take the standard deviation of the phases in each bin.

Final note: For the error propagation the formula for the weighted average is used. This is why in my opinion only for the weighted average it is appropriate to set *A* to one.

The program is run in the shell by

```
$ binfold -c <config file>
```

A.3 Analysis of *Fermi*-LAT data

The data obtained by the Large Area Telescope (LAT) on-board the *Fermi* satellite are available to the public and can be downloaded from the *Fermi* Science Support Center³. The raw data files are provided in the FITS format (Flexible Image Transport System, and the standard is defined in Wells et al. 1981). The software necessary for the analysis of the raw data is also available for free download⁴ and is called *Fermi* ScienceTools.

A.3.1 Generating *Fermi*-LAT light curves

In order to generate light curves from the raw data FITS files downloaded from the *Fermi* Science Support Center, one has to divide the data into time bins of a certain size (e.g., 1 day) and perform likelihood analysis on each of these time bins. The procedure of likelihood analysis is explained step by step at http://fermi.gsfc.nasa.gov/ssc/data/analysis/scitools/likelihood_tutorial.html.

Before the release of Pass 8 (on June 24, 2015) I used the script `like_lc.pl` written by Robin Corbet and which was available from the

³<http://fermi.gsfc.nasa.gov/ssc/data/>

⁴<http://fermi.gsfc.nasa.gov/ssc/data/analysis/software/>

user's contribution section of the *Fermi* Science Support Center. The light curves for Jaron & Massi (2014) were produced in this way.

After the release of Pass 8, the above mentioned script did not work straight away, which is why I wrote a new PERL script which worked with Pass 8, and which in addition used configuration files and distributed the computations of each time bin onto different cores of a computer to speed up the calculations. This script is printed here in Listing A.1.

```

1  #!/usr/bin/perl -w
2
3  use Getopt::Long;
4  use Parallel::ForkManager;
5
6  my $configfile;
7  my $handle;
8  my $keyword;
9  my $value;
10 my $verbosity = 1;
11 my $plist = 'plist.dat';
12 my $slist = 'slist.dat';
13 my $semin = '100';
14 my $semax = '300000';
15 my $svarmin = '41.6';
16 my $svarfile = 'var.csv';
17 my $srad = '10.0';
18 my $ststep = '5.0';
19 my $sncores = 8;
20 my $scatfile = 'gll_psc_v16.fit';
21 my $modelfile = 'mymodel.xml';
22 my $automodel = '0';
23 my $zmax = 90;
24 my $schat = 1;
25 my $scfile;
26 my $lcfile;
27 my $srcfound = 0;
28 my $flux;
29 my $dflux;
30 my $alpha;
31 my $dalpha;
32 my $stsvalue;
33 my $delold = 0;
34 my $spm;
35 my $loglike;
36
37 # Parameters for gtmktime
38 my $sirfs = "CALDB";
39

```

```

40 GetOptions(
41     'c|config=s' => \$configfile ,
42     'verbosity=i' => \$verbosity
43 );
44
45 if ($verbosity >= 1) {
46     print "This_is_like_lc_fj.pl\n";
47 }
48
49 if ($verbosity >= 2) {
50     print "Going_to_read_configuration_file_\$configfile\.\n";
51 }
52
53 open($handle, '<', $configfile);
54
55 while (<$handle>) {
56     (keyword, $value) = split /\s+/;
57     if ($verbosity > 1) {
58         print "keyword=.$keyword\n";
59         print "value=.$value\n";
60     }
61     if (uc($keyword) =~ /^PLIST$/) {
62         $plist = $value;
63     } elsif (uc($keyword) =~ /^SLIST$/) {
64         $slist = $value;
65     } elsif (uc($keyword) =~ /^EMINS/) {
66         $emin = $value;
67     } elsif (uc($keyword) =~ /^EMAX$/) {
68         $emax = $value;
69     } elsif (uc($keyword) =~ /^VARMIN$/) {
70         $varmin = $value;
71     } elsif (uc($keyword) =~ /^VARFILES/) {
72         $varfile = $value;
73     } elsif (uc($keyword) =~ /^RAD$/) {
74         $rad = $value;
75     } elsif (uc($keyword) =~ /^TSTEP$/) {
76         $step = $value;
77     } elsif (uc($keyword) =~ /^NCORE$/) {
78         $cores = $value;
79     } elsif (uc($keyword) =~ /^CATFILES/) {
80         $catfile = $value;
81     } elsif (uc($keyword) =~ /^MODELFILES/) {
82         $modelfile = $value;
83     } elsif (uc($keyword) =~ /^AUTOMODELS/) {
84         $automodel = $value;
85     } elsif (uc($keyword) =~ /^ZMAX$/) {
86         $zmax = $value;
87     } elsif (uc($keyword) =~ /^CHATTER$/) {
88         $chatter = $value;
89     } elsif (uc($keyword) =~ /^TSTART$/) {

```

```

90     $tstart = $value;
91 } elseif (uc($keyword) =~ /^TSTOPS/) {
92     $tstop = $value;
93 } elseif (uc($keyword) =~ /^SCFILE$/ ) {
94     $scfile = $value;
95 } elseif (uc($keyword) =~ /^IRFS$/ ) {
96     $irfs = $value;
97 } elseif (uc($keyword) =~ /^LCFILE$/ ) {
98     $lcfile = $value;
99 } elseif (uc($keyword) =~ /^DELOLD$/ ) {
100    $delold = $value;
101 } else {
102     print "Warning: Unknown keyword \"$keyword\" in
        configuration file \"$configfile\"!\n";
103 }
104 }
105 close($handle);
106
107 if ($automodel != 0) {
108     die "Automatic generation of model file not implemented yet
        .\n";
109 }
110
111 # Read source list
112
113 if ($slist) {
114     open($handle, '<', $slist) || die "Error opening source list
        file \"$slist\" for reading.\n";
115 } else {
116     die "Error: No source list file given!\n";
117 }
118
119 if ($verbosity >= 2) {
120     print "Reading source list file \"$slist\"...\n";
121 }
122
123 if ($delold) {
124     $cmd = "rm $lcfile";
125     system($cmd);
126 }
127
128 my $nsrc = 0;
129 while (<$handle>) {
130     ($source[$nsrc], $ra[$nsrc], $dec[$nsrc]) = split /\s+/;
131     $nsrc++;
132     if ($verbosity >= 2) {
133         print "Source $nsrc: \"$source[$nsrc - 1]\", ra=$ra[$nsrc
            - 1], dec=$dec[$nsrc - 1]\n";
134     }
135 }

```

```

136
137 if ($verbosity >= 2) {
138   print "Done_reading_source_list_file.\n";
139 }
140
141 # Source loop
142 for (my $i = 0; $i < $nsrc; $i++) {
143   # Likelihood analysis
144
145   # Get start and stop time
146
147   my $eventfile0 = make_temp("eventfile0.fits");
148
149   # Time loop
150
151   my $tmin;
152   my $tmax;
153   my $t;
154
155   $spm = new Parallel::ForkManager($ncores);
156
157   for ($t = $tstart; $t < $tstop; $t += $tstep) {
158     my $pid = $spm->start and next;
159
160     # gtselect
161     my $eventfile1 = make_temp("eventfile1.fits");
162     $tmin = mjd2met($t);
163     $tmax = mjd2met($t + $tstep);
164     $cmd = "gtselect_chatter=$chatter_zmax=$zmax_emin=$emin_
           emax=$emax_infile=@$plist_outfile=$eventfile1_ra=
           $ra[$i]_dec=$dec[$i]_rad=$rad_tmin=$tmin_tmax=$tmax
           _evclass=128_evtype=3";
165
166     if ($verbosity >= 2) {
167       print "\n".$cmd."\n";
168     }
169     system($cmd);
170
171     # gtmktime
172     my $eventfile2 = make_temp("eventfile2.fits");
173     my $bore_limit = 180;
174     my $filter = "(DATA_QUAL==1)&&(LAT_CONFIG==1)&&(
           angsep(RA_ZENITH,DEC_ZENITH,$ra[$i],$dec[$i])\|_rad
           <$zmax)&&(angsep($ra[$i],$dec[$i],RA_SCZ,DEC_SCZ)
           <$bore_limit)";
175
176     my $roicut = "n";
177     $cmd = "gtmktime_scfile=$scfile_filter=\"$filter\"_
           roicut=$roicut_evfile=$eventfile1_outfile=
           $eventfile2_chatter=$chatter";
178
179     if ($verbosity >= 2) {
180       print "\n".$cmd."\n";
181     }
182   }
183 }

```

```

178     }
179     system ($cmd);
180
181     # gltcube
182     my $expcube = make_temp("expcube.fits");
183     $cmd = "gltcube┬ chatter=$chatter┬ evfile=$eventfile2┬
        scfile=$scfile┬ outfile=$expcube┬ dcostheta=0.025┬
        binsz=1";
184     if ($verbosity >= 2) {
185         print "\n".$cmd."\n";
186     }
187     system ($cmd);
188
189     # gtexpmap
190     my $expmap = make_temp("expmap.fits");
191     my $srcrad = $rad + 10.0;
192     $cmd = "gtexpmap┬ chatter=$chatter┬ evfile=$eventfile2┬
        scfile=$scfile┬ expcube=$expcube┬ outfile=$expmap┬
        irfs=$irfs┬ srcrad=$srcrad┬ nlong=120┬ nlat=120┬
        nenergies=20";
193     if ($verbosity >= 2) {
194         print "\n".$cmd."\n";
195     }
196     system ($cmd);
197
198     # gtdiffrsp
199     $cmd = "gtdiffrsp┬ chatter=$chatter┬ evfile=$eventfile2┬
        scfile=$scfile┬ srcmdl=$modelfile┬ irfs=$irfs";
200     if ($verbosity >= 2) {
201         print "\n".$cmd."\n";
202     }
203     system ($cmd);
204
205     # gtlike
206     my $resultfile = make_temp("results.dat");
207     my $specfile = make_temp("counts_spectra.fits");
208     $cmd = "gtlike┬ results=$resultfile┬ specfile=$specfile┬
        chatter=$chatter┬ irfs=$irfs┬ expcube=$expcube┬ srcmdl
        =$modelfile┬ statistic=UNBINNED┬ optimizer=MINUIT┬
        evfile=$eventfile2┬ scfile=$scfile┬ expmap=$expmap┬
        cmap=none┬ bexpmap=none";
209     if ($verbosity >= 2) {
210         print "\n".$cmd."\n";
211     }
212     system ($cmd);
213
214     # Extract values from results.dat
215
216     my $resultshandle;
217     my $insrc = 0;

```

```

218 $srcfound = 0;
219 open($resultshandle , "<", $resultsfile);
220 while (<$resultshandle >) {
221     my @line = split /\s+;/;
222
223     my $src = $source[$i];
224     if ($line[0] =~ /${src}/) {
225         if ($verbosity >= 1) {
226             print "Found the source of \"$source[$i]\".\n";
227         }
228         $insrc = 1;
229         $srcfound = 1;
230     }
231
232     if ($insrc == 1) {
233         if ($line[0] =~ /Index/) {
234             $alpha = substr($line[1], 1);
235             $dalpha = substr($line[3], 0, -2);
236         } elsif ($line[0] =~ /TS/) {
237             $tsvalue = substr(substr($line[2], 1), 0,
238                             -2);
239         } elsif ($line[0] =~ /Flux/) {
240             $flux = substr($line[1], 1);
241             $dflux = substr($line[3], 0, -2);
242         } elsif ($line[0] =~ /\^\/,$/) {
243             $insrc = 0;
244         }
245     }
246     close($resultshandle);
247
248     if ($verbosity >= 2) {
249         print "Results for current time bin of \"($t + $step
250             /2.0).\" LMD)\n";
251         print "Source: \"$source[$i]\".\n";
252         if ($srcfound == 1) {
253             print "Flux: \"$flux+/- $dflux\".\n";
254             print "Index: \"$alpha+/- $dalpha\".\n";
255             print "TS value: \"$tsvalue\". sqrt($tsvalue).\"
256                 sigma)\n";
257         } else {
258             print "Did not find the source!\n";
259         }
260     }
261
262     my $lchandle;
263     if ($srcfound == 1) {
264         open ($lchandle, ">>", $lcf);
265         print $lchandle ($t + $step/2.0)."\t". $flux. "\t".

```



```

                $dflux."\t".$alpha."\t".$dalpha."\t".$stvalue."
                \n";
265         close ($lhandle);
266     }
267
268     # Clean up
269     $cmd = "rm$_eventfile1$_eventfile2$_expmmap$_expcube_
            $resultsfile$_specfile";
270     system($cmd);
271
272     if ($verbosity >= 1) {
273         print "Finished$_time$_bin_".($t + $tstep/2.0)."$_MJD\n
            ";
274     }
275
276     $pm->finish; # Terminates the child process
277 } # End of time loop.
278 $pm->wait_all_children;
279 }
280
281
282 exit;
283
284 #####
285 # convert MJD to MET
286 # start and stop times are specified on command line in MJD
    units
287 # but science tools use MET
288
289 sub mjd2met{
290 my $value = shift;
291
292 # This makes an assumption about UT vs. TT...
293 $result = ($value - (51910.0 + 7.428703703703703E-4)) * 86400.0;
294
295 return($result)
296 }
297
298 sub make_temp{
299     return "tmp_".$$.$_[0];
300 }

```

Listing A.1: PERL script to produce a light curve from raw Fermi-LAT data

Acknowledgements

The work on this thesis over the past three years has been a great experience. But it would not have been possible without the contribution of many people whom I would like to thank here.

This PhD thesis was supervised by Dr. Maria Massi in the best possible way. She was always available when I needed advice and we had a lot of very fruitful discussions.

My second advisor Prof. Norbert Langer gave very good comments and advice during regular meetings.

I thank Prof. Karl Menten for giving me the opportunity to be a member of his working group and for allowing me to travel to conferences to present and discuss my results.

I thank Prof. Ian Brock and Prof. Hubert Schorle for joining the thesis examination committee.

Dr. Lisa Zimmermann helped me a lot to get started with the topic of X-ray binaries and LS I +61°303.

Prof. Eduardo Ros was a regular member of meetings and contributed very useful comments.

The observations at the 100-m telescope in Effelsberg during Easter 2014 would not have been possible without the participation of Dr. Lars Fuhrmann, Dr. Guang-Xing Li, and Dr. Xun Shi, who contributed invaluable work observing at the telescope. Dr. Emmanouil Angelakis and Dr. Ioannis Myserlis helped a lot with the calibration of the data.

I thank Dr. Sergio Dzib for the fruitful collaboration about MWC 656.

Whenever I had question concerning the analysis of *Fermi*-LAT data, Dr. Bindu Rani was there to share her knowledge with me.

The computationally expensive analysis of *Fermi*-LAT data would not have been feasible in a reasonable time without the kind permission to use nodes from the VLBI correlator cluster given by Dr. Walter Alef, Dr. Helge Rottmann, and Dr. Alessandra Bertarini.

Dr. Robin Corbet often answered my questions concerning the analysis of *Fermi*-LAT data. He kindly organized and hosted my visit to the Goddard Space Flight Center in November 2015. It has been a unique opportunity to share and discuss my results in addition to learning about some aspects of the research carried out at that institute.

I owe my deepest gratitude to Dr. Guidetta Torricelli-Ciamponi for the collaboration on the physical model and for answering a lot of questions about it.

I thank all of the people with whom I shared the office during this project for creating a pleasant working environment.

This project would not have been possible without the support by my family, in particular my mother Alice Jaron, and my father Dr. Michael Jaron, and my grandmother Marie-Louise Kremer. I would like to emphasize the contribution by my grandfather Dipl.-Ing. Franz Kremer, who interested me in the exciting field of astronomy when I was still a child, and who taught me computer programming at the age of nine. May he rest in peace. My brother René Jaron lent me a helping hand frequently, and his wife Luisa Jaron kindly provided me with equipment. Thanks to Elisa Volmering for being there.

This PhD project was supported by a stipend from the Max Planck Society. It was an honour to be a member of the International Max Planck Research School (IMPRS), who also provided additional financial support for travelling.

Bibliography

Abbasi, R. et al. 2012, *ApJ*, 748, 118, 1108.3023

Abbott, B. P. et al. 2016, *Physical Review Letters*, 116, 061102, 1602.03837

Abdo, A. A. et al. 2011, *ApJ*, 736, L11, 1103.4108

———. 2009a, *ApJS*, 183, 46, 0902.1340

———. 2009b, *ApJ*, 701, L123, 0907.4307

———. 2009c, *ApJ*, 706, L56, 0910.5520

Acero, F. et al. 2015, *ApJS*, 218, 23, 1501.02003

Ackermann, M. et al. 2013, *ApJ*, 773, L35

Aharonian, F. et al. 2005, *A&A*, 442, 1, astro-ph/0506280

Aharonian, F. A. et al. 2007, *A&A*, 469, L1, 0704.0171

Albert, J. et al. 2009, *ApJ*, 693, 303, 0806.1865

———. 2006, *Science*, 312, 1771, arXiv:astro-ph/0605549

———. 2007, *ApJ*, 665, L51, 0706.1505

Aleksić, J. et al. 2015, *ArXiv e-prints*, 1502.01529

Alexander, M. J., & McSwain, M. V. 2015, *MNRAS*, 449, 1686, 1502.07385

- Anderhub, H. et al. 2009, *ApJ*, 706, L27, 0910.4381
- Angelakis, E. et al. 2015, *A&A*, 575, A55, 1501.02158
- Atwood, W. B. et al. 2009, *ApJ*, 697, 1071, 0902.1089
- Bailyn, C. D., Orosz, J. A., McClintock, J. E., & Remillard, R. A. 1995, *Nature*, 378, 157
- Belczynski, K., & Ziolkowski, J. 2009, *ApJ*, 707, 870, 0907.4990
- Blandford, R. D., & Königl, A. 1979, *ApJ*, 232, 34
- Bodaghee, A., Tomsick, J. A., Pottschmidt, K., Rodriguez, J., Wilms, J., & Pooley, G. G. 2013, *ApJ*, 775, 98, 1307.3264
- Bondi, H., & Hoyle, F. 1944, *MNRAS*, 104, 273
- Bordas, P., Yang, R., Kafexhiu, E., & Aharonian, F. 2015, *ApJ*, 807, L8, 1411.7413
- Bosch-Ramon, V., Paredes, J. M., Romero, G. E., & Ribó, M. 2006, *A&A*, 459, L25
- Calvelo, D. E. et al. 2010, *MNRAS*, 409, 839, 1007.2313
- Casares, J., Negueruela, I., Ribo, M., Ribas, I., Paredes, J. M., Herrero, A., & Simon-Diaz, S. 2014, *ArXiv e-prints*, 1401.3711
- Casares, J., Ribas, I., Paredes, J. M., Martí, J., & Allende Prieto, C. 2005, *MNRAS*, 360, 1105, arXiv:astro-ph/0504332
- Casares, J., Ribó, M., Ribas, I., Paredes, J. M., Vilardell, F., & Negueruela, I. 2012, *MNRAS*, 421, 1103, 1201.1726
- Chernyakova, M. et al. 2014, *MNRAS*, 439, 432, 1401.1386
- . 2015, *ArXiv e-prints*, 1508.01339
- Connors, T. W., Johnston, S., Manchester, R. N., & McConnell, D. 2002, *MNRAS*, 336, 1201, arXiv:astro-ph/0207302

-
- Corbel, S., Coriat, M., Brocksopp, C., Tzioumis, A. K., Fender, R. P., Tomsick, J. A., Buxton, M. M., & Bailyn, C. D. 2013, *MNRAS*, 428, 2500, 1211.1600
- D’Ai, A., Cusumano, G., La Parola, V., Segreto, A., & Mineo, T. 2016, *ArXiv e-prints*, 1601.03260
- Dhawan, V., Mioduszewski, A., & Rupen, M. 2006, in *VI Microquasar Workshop: Microquasars and Beyond*
- Dubus, G. 2006, *A&A*, 456, 801, *arXiv:astro-ph/0605287*
- . 2013, *A&A Rev.*, 21, 64, 1307.7083
- Dulk, G. A. 1985, *ARA&A*, 23, 169
- Dzib, S. A., Massi, M., & Jaron, F. 2015, *ArXiv e-prints*, 1507.04488
- Esposito, P., Caraveo, P. A., Pellizzoni, A., de Luca, A., Gehrels, N., & Marelli, M. A. 2007, *A&A*, 474, 575, 0708.3330
- Falcke, H., Patnaik, A. R., & Sherwood, W. 1996, *ApJ*, 473, L13, *astro-ph/9610049*
- Fender, R., & Belloni, T. 2004, *ARA&A*, 42, 317, *astro-ph/0406483*
- Fender, R. P., Gallo, E., & Jonker, P. G. 2003, *MNRAS*, 343, L99, *astro-ph/0306614*
- Fuhrmann, L. et al. 2014, *MNRAS*, 441, 1899, 1403.4170
- Gallo, E., Fender, R., Kaiser, C., Russell, D., Morganti, R., Oosterloo, T., & Heinz, S. 2005, *Nature*, 436, 819, *astro-ph/0508228*
- Gallo, E., Fender, R. P., Miller-Jones, J. C. A., Merloni, A., Jonker, P. G., Heinz, S., Maccarone, T. J., & van der Klis, M. 2006, *MNRAS*, 370, 1351, *astro-ph/0605376*
- Gallo, E., Fender, R. P., & Pooley, G. G. 2003, *MNRAS*, 344, 60, *astro-ph/0305231*

- Gallo, E. et al. 2014, ArXiv e-prints, 1408.3130
- Ginzburg, V. L., & Syrovatskii, S. I. 1965, ARA&A, 3, 297
- Gregory, P. C. 2002, ApJ, 575, 427
- Gregory, P. C., Peracaula, M., & Taylor, A. R. 1999, ApJ, 520, 376
- Gregory, P. C., & Taylor, A. R. 1978, Nature, 272, 704
- Grudzinska, M. et al. 2015, ArXiv e-prints, 1504.03146
- Grundstrom, E. D. et al. 2007, ApJ, 656, 437, arXiv:astro-ph/0610608
- H. E. S. S. Collaboration et al. 2015, ArXiv e-prints, 1503.02711
- Hadasch, D. et al. 2012, ApJ, 749, 54, 1202.1866
- Harding, A. K. 2013, Frontiers of Physics, 8, 679, 1302.0869
- Heald, G. et al. 2011, Journal of Astrophysics and Astronomy, 32, 589, 1106.3195
- Hjellming, R. M., & Johnston, K. J. 1988, ApJ, 328, 600
- Hjellming, R. M., & Rupen, M. P. 1995, Nature, 375, 464
- Hutchings, J. B., & Crampton, D. 1981, PASP, 93, 486
- Illarionov, A. F., & Sunyaev, R. A. 1975, A&A, 39, 185
- Jansky, K. G. 1933, Nature, 132, 66
- Jaron, F., & Massi, M. 2013, A&A, 559, A129
- . 2014, A&A, 572, A105, 1412.2028
- Jaron, F., Torricelli-Ciamponi, G., & Massi, M. submitted, to A&A
- Johnston, S., Manchester, R. N., Lyne, A. G., Bailes, M., Kaspi, V. M., Qiao, G., & D'Amico, N. 1992, ApJ, 387, L37
- Kaiser, C. R. 2006, MNRAS, 367, 1083, astro-ph/0601103

-
- Kaufman Bernadó, M. M., Romero, G. E., & Mirabel, I. F. 2002, *A&A*, 385, L10, astro-ph/0202316
- Kernighan, B. W., & Ritchie, D. M. 1988, *The C Programming Language* (Prentice Hall)
- Kniffen, D. A. et al. 1997, *ApJ*, 486, 126
- Kurahashi, N., & for the IceCube Collaboration. 2014, *ArXiv e-prints*, 1402.3627
- Linnell Nemeč, A. F., & Nemeč, J. M. 1985, *AJ*, 90, 2317
- Lomb, N. R. 1976, *Ap&SS*, 39, 447
- Lucarelli, F. et al. 2010, *The Astronomer's Telegram*, 2761, 1
- Maraschi, L., & Treves, A. 1981, *MNRAS*, 194, 1P
- Mariaud, C., Bordas, P., Aharonian, F., Boettcher, M., Dubus, G., de Naurois, M., Romoli, C., & V. Zabalza for the H. E. S. S. Collaboration. 2015, *ArXiv e-prints*, 1509.05791
- Marti, J., & Paredes, J. M. 1995, *A&A*, 298, 151
- Martin, R. G., Tout, C. A., & Pringle, J. E. 2008, *MNRAS*, 387, 188, 0802.3912
- Massi, M. 2004, *A&A*, 422, 267, arXiv:astro-ph/0404605
- Massi, M., & Jaron, F. 2013, *A&A*, 554, A105, 1303.2007
- Massi, M., Jaron, F., & Hovatta, T. 2015, *ArXiv e-prints*, 1502.00934
- Massi, M., & Kaufman Bernadó, M. 2009, *ApJ*, 702, 1179, 0908.2600
- Massi, M., Ribó, M., Paredes, J. M., Garrington, S. T., Peracaula, M., & Martí, J. 2004, *A&A*, 414, L1, arXiv:astro-ph/0312091
- Massi, M., Ros, E., & Zimmermann, L. 2012, *A&A*, 540, A142, 1203.4621

- Massi, M., & Torricelli-Ciamponi, G. 2014, *A&A*, 564, A23, 1402.3983
- . 2016, *A&A*, 585, A123, 1511.05621
- Massi, M., & Zimmermann, L. 2010, *A&A*, 515, A82, 1003.3693
- McClintock, J. E., & Remillard, R. A. 2006, *Black hole binaries*, ed. W. H. G. Lewin & M. van der Klis, 157–213
- McSwain, M. V., Ray, P. S., Ransom, S. M., Roberts, M. S. E., Dougherty, S. M., & Pooley, G. G. 2011, *ApJ*, 738, 105, 1106.5550
- Merloni, A., & Heinz, S. 2007, *MNRAS*, 381, 589, 0707.3356
- Merloni, A., Heinz, S., & di Matteo, T. 2003, *MNRAS*, 345, 1057, astro-ph/0305261
- Miller-Jones, J. C. A., Jonker, P. G., Maccarone, T. J., Nelemans, G., & Calvelo, D. E. 2011, *ApJ*, 739, L18, 1106.0097
- Mirabel, I. F. 2006, *Science*, 312, 1759, arXiv:astro-ph/0606393
- Mirabel, I. F., & Rodríguez, L. F. 1999, *ARA&A*, 37, 409, arXiv:astro-ph/9902062
- Mirabel, I. F., Rodríguez, L. F., Cordier, B., Paul, J., & Lebrun, F. 1992, *Nature*, 358, 215
- Moldón, J., Ribó, M., & Paredes, J. M. 2012, *A&A*, 548, A103, 1209.6073
- Munar-Adrover, P., Paredes, J. M., Ribó, M., Iwasawa, K., Zabalza, V., & Casares, J. 2014, *ApJ*, 786, L11, 1404.0901
- Nolan, P. L. et al. 2012, *ApJS*, 199, 31, 1108.1435
- Okazaki, A. T. 1997, *A&A*, 318, 548
- Paredes, J. M., Estalella, R., & Rius, A. 1990, *A&A*, 232, 377

-
- Paredes-Fortuny, X., Ribó, M., Bosch-Ramon, V., Casares, J., Fors, O., & Núñez, J. 2015, ArXiv e-prints, 1501.02208
- Pe'er, A., & Casella, P. 2009, ApJ, 699, 1919, 0902.2892
- Peracaula, M., Marti, J., & Paredes, J. M. 1997, A&A, 328, 283
- Piner, B. G., Unwin, S. C., Wehrle, A. E., Zook, A. C., Urry, C. M., & Gilmore, D. M. 2003, ApJ, 588, 716, astro-ph/0301333
- Potter, W. J., & Cotter, G. 2012, MNRAS, 423, 756, 1203.3881
- Poutanen, J., & Veledina, A. 2014, Space Sci. Rev., 183, 61, 1312.2761
- Psaltis, D. 2004, ArXiv Astrophysics e-prints, arXiv:astro-ph/0410536
- Rau, U., & Cornwell, T. J. 2011, A&A, 532, A71, 1106.2745
- Ray, P. S., Foster, R. S., Waltman, E. B., Tavani, M., & Ghigo, F. D. 1997, ApJ, 491, 381, arXiv:astro-ph/9710033
- Rivinius, T., Carciofi, A. C., & Martayan, C. 2013, A&A Rev., 21, 69, 1310.3962
- Rodriguez, L. F., & Mirabel, I. F. 1995, Proceedings of the National Academy of Science, 92, 11390
- Romero, G. E., Christiansen, H. R., & Orellana, M. 2005, ApJ, 632, 1093, arXiv:astro-ph/0506735
- Romero, G. E., Okazaki, A. T., Orellana, M., & Owocki, S. P. 2007, A&A, 474, 15, 0706.1320
- Rybicki, G. B., & Lightman, A. P. 1986, Radiative Processes in Astrophysics
- Scargle, J. D. 1982, ApJ, 263, 835
- Sidoli, L., Pellizzoni, A., Vercellone, S., Moroni, M., Mereghetti, S., & Tavani, M. 2006, A&A, 459, 901, arXiv:astro-ph/0606722

- Siegert, T. et al. 2016, ArXiv e-prints, 1603.01169
- Smith, M. D. 2012, *Astrophysical Jets and Beams*
- Strickman, M. S., Tavani, M., Coe, M. J., Steele, I. A., Fabregat, J., Martí, J., Paredes, J. M., & Ray, P. S. 1998, *ApJ*, 497, 419, astro-ph/9711286
- Tavani, M. et al. 1996, *A&AS*, 120, 243, astro-ph/9611200
- Taylor, A. R., Kenny, H. T., Spencer, R. E., & Tzioumis, A. 1992, *ApJ*, 395, 268
- The Fermi LAT Collaboration, Coe, M. J., Di Mille, F., Edwards, P. G., Filipović, M. D., Payne, J. L., Stevens, J., & Torres, M. A. P. 2012, ArXiv e-prints, 1202.3164
- Torrence, C., & Compo, G. P. 1998, *Bulletin of the American Meteorological Society*, 61
- Ubuntu. 2013, Ubuntu, <http://www.ubuntu.com>
- Štefl, S. et al. 2009, *A&A*, 504, 929, 0907.2250
- van Dijk, R. et al. 1996, *A&A*, 315, 485, astro-ph/9604136
- van Leeuwen, F. 2007, *A&A*, 474, 653, 0708.1752
- Wells, D. C., Greisen, E. W., & Harten, R. H. 1981, *A&AS*, 44, 363
- Williams, S. J., Gies, D. R., Matson, R. A., Touhami, Y., Grundstrom, E. D., Huang, W., & McSwain, M. V. 2010, *ApJ*, 723, L93, 1009.4947
- Zamanov, R., Stoyanov, K., Marti, J., Tomov, N. A., Belcheva, G., Luque-Escamilla, P. L., & Latev, G. 2013, ArXiv e-prints, 1309.3947
- Zamanov, R. K., Martí, J., Paredes, J. M., Fabregat, J., Ribó, M., & Tarasov, A. E. 1999, *A&A*, 351, 543, arXiv:astro-ph/9909233
- Zimmermann, L., Fuhrmann, L., & Massi, M. 2015, *A&A*, 580, L2, 1507.00859

Curriculum Vitae

Name: Frédéric Felix Daniel Jaron
Place of birth: Siegburg, Germany
Date of birth: ■■■■■

Education

Master of Science in Physics (2013)

Master thesis: “Properties of the Radio Emission from the
Gamma-ray Binary LS I +61°303”
Supervisor: Priv.-Doz. Dr. Maria Massi

Bachelor of Science in Physics (2010)

Bachelor thesis: “Phase-Calibration Signal Extraction from VLBI
Radio Data within the DiFX Software Correlator”
Supervisor: Priv.-Doz. Dr. Maria Massi

Publications

Refereed

Dzib, S., Massi, M., Jaron, F., “Radio emission from the Be/black hole binary MWC 656”, 2015, A&A, 580, L6

Massi, M., Jaron, F., Hovatta, T., “Long-term OVRO monitoring of LS I +61°303: confirmation of the two close periodicities”, 2015, *A&A*, 575, L9

Jaron, F., Massi, M., “Discovery of a periodical apoastron GeV peak in LS I +61°303”, 2014, *A&A*, 572, A105

Jaron, F., Massi, M., “Prediction of the radio outbursts of LS I +61°303”, 2013, *A&A*, 559, A129

Massi, M., Jaron, F., “Long-term periodicity in LS I +61°303 as beat-frequency between the orbital and precessional rate”, 2012, *A&A*, 554, A105

Submitted

Jaron, F., Torricelli-Ciamponi, G., Massi, M., “Understanding the periodicities in the radio and GeV emission from LS I +61°303”, submitted to *A&A*

Conference Proceedings

Jaron, F., Massi, M., “The apparent discontinuity in the periodicity of the GeV emission from LS I +61°303”, 2015, arXiv:1502.03039

Massi, M., Jaron, F., “A new radio feature in the gamma ray binary LS I +61°303”, 2012, American Institute of Physics Conference Series, 1505, 378